Microscopic modeling of high-field charge transport in amorphous Selenium

by

Ali Darbandi

A thesis

submitted in conformity with the requirements for the degree of

Master of Science

in

Department of Physics

Lakehead University

© Ali Darbandi, 2012

October 26, 2012

ABSTRACT

Avalanche multiplication of charge carriers as a result of successive impact ionization has led to the development of solid state avalanche photo-detectors. Crystalline based avalanche photodiodes have found a variety of applications including laser range finders and fiber optic telecommunications. Recently, there is a growing interest to employ *amorphous* semiconductors due to their economically favourbale costs and capability to be readily prepared in the desired size and structure with high efficiency. Selenium is the only material that has been reported to clearly feature the avalanche phenomenon in the amorphous phase in a practical electric field. Selenium based avalanche photo-diodes motivated commercialization of TV camera tubes which are capable of capturing images at extremely low light intensities. In addition, amorphous Selenium exhibits a high potential for development of x ray and γ ray detectors for medical imaging devices. Hence, studying the electronic properties of Selenium is worthwhile for advancement of functional amorphous materials that feature impact ionization.

The energy loss mechanism that prevents the carriers from gaining sufficient kinetic energy to initiate impact ionization is inelastic scattering of electrons and holes with optical phonons. The latter interaction in Selenium is analyzed in this work. To overcome the computational difficulties, a crystalline structure of Selenium was studied, however it is of interest to extend the outcomes to amorphous phase. Here, we assume that the calculated results based on trigonal Selenium structure can be also translated into the amorphous structure.

This assumption is supported by further studies of density of states and phonon density of states in both amorphous and crystalline phases of Selenium. In addition, validity of our assumption is further confirmed by simulating an amorphous Selenium structure. Volume deformation potential was studied for both trigonal and the simulated amorphous selenium.

Electronic structure of trigonal Selenium was studied and calculations of electron-phonon matrix elements were performed in order to analyze the inelastic scattering processes. Computations were done in the framework of density functional theory. Results represent a more intense scattering rate for electrons than for holes. This resolves the long standing question that why holes undergo avalanche multiplication at lower electric fields than electrons in amorphous Selenium.

A closer study of the electronic structure prepared in latter analysis suggest that a domination of holes avalanche multiplication can be observed in Selenium. This is because the excess energy of electrons is confined by a peculiar dispersion of the conduction band. The latter provided a basis to propose the single carrier multiplication due to a limited band dispersion for development of novel functional semiconductors. Single carrier avalanche is a performance requirement of APDs with low excess noise. Further investigation involved calculations of ionization threshold energies and analysis of all possible inverse Auger transitions for both electrons and holes in the Selenium Brillouin zone.

In addition, though the low excess noise is a requirement for development of Selenium-based *avalanche detectors*, at the same time the energy resolution is another important factor for Selenium-based *direct conversion detectors*. Energy resolution can be determined by Fano factor. Therefore, the Fano factor and pair creation energy were also studied through numerical analysis of density of states for trigonal and amorphous Selenium in this thesis.

DEDICATION

To my parents for their love, endless support and encouragement.

ACKNOWLEDGEMENTS

I would like to express my sincere gratitude to my advisor Dr. Oleg Rubel for his continuous support of my research, for his patience, motivation, enthusiasm, and immense knowledge. His guidance and his insightful discussions about the research helped me all the time.

I am also thankful to my supervisory committee members, Drs. Hubert de Guise and Mark Gallagher for all of their support and advice in committee meetings.

At the end I would like to extend my appreciation to Thunder Bay Regional Research Institute for providing the research facilities, and also special thanks to NSERC and CEDC for financial support of the project.

CONTENTS

1. Introduction 13

1.1 Crystalline and non-crystalline solids 13

1.2 Avalanche multiplication 18

1.3 Application of amorphous Selenium based photodetectors in medical imaging . 22

1.4 Thesis motivation and outlines 27

2. Theory of charge transport at high-fields 30

2.1 Impact ionization in solids 30

2.2 Lucky drift model in crystalline solids 33

2.3 Lucky drift model in disordered materials 33

2.4 Electron-phonon interaction 37

3. Methods and frameworks 41

3.1 Electronic properties of crystalline and amorphous Selenium 41

3.2 Electronic structure of crystalline and amorphous Selenium 42

3.3 Density of states of crystalline and amorphous Selenium 46

3.4 Phonon density of states in crystalline and amorphous Selenium 48

3.5 Density functional theory 49

3.6 Computational *ab initio* analysis 54

4. Results and Discussions 58

4.1 Interaction of hot carriers with optical phonons in Selenium 58

4.1.1 Structural model of trigonal Selenium 58

4.1.2 Optical phonon perturbations in Selenium 60
4.1.3 Electron-phonon matrix elements 61
4.1.4 Simulation of the amorphous Selenium structure 66
4.1.5 Volume deformation potential in amorphous Selenium 69
4.2 Single carrier impact ionization favored by a limited band dispersion 72
4.2.1 Confinement of carriers excess energy 72
4.2.2 Principle conservation rules in impact ionization 74
4.2.3 Effective density of states for impact ionization 76
4.3 Modeling the radiation ionization energy of t-Se and a-Se 80
4.3.1 Pair creation energy 80
4.3.2 Fano factor 86

5. Summary 92

LIST OF FIGURES

1.1 t-Se and a-Se structure . . . 14

1.2 Dihedral angle ϕ, bond angle θ, and bond length r are shown in the picture . . . 15

1.3 Pair distribution function in crystal and amorphous solids . . . 16

1.4 Enthalpy of a material as a function of atomic configuration ([1] p.65) . . . 17

1.5 Schematic process of holes avalanche multiplication . . . 19

1.6 Electron excess noise factor versus multiplication factor for different k [2] . . . 20

1.7 DOS of t-Se and a-Se . . . 22

1.8 Direct and indirect conversion a-Se photodetector . . . 23

1.9 Comparison images of HARP and standard camera . . . 24

1.10 PET scanner detector design . . . 25

2.1 Carrier trajectory with relevant elastic and inelastic scattering [3]. . . . 34

2.2 Carrier kinetic energy diagram . . . 35

2.3 Impact ionization coefficient in a-Se . . . 37

3.1 Crystal structure of trigonal Selenium . . . 42

3.2 Bonding configuration of Silicon and Selenium atoms . . . 43

3.3 Direct and indirect gap semiconductor band structure . . . 44

3.4 extended states and localized state wavefunctions . . . 45

3.5 a-Se and t-Se density of states [4] . . . 47

3.6 Phonon DOS of t-Se and a-Se . . . 48

3.7 pseudo-wavefunction and pseudopotential . . . 55

4.1 Schematic illustration of the six optical vibration modes of Selenium [5]. . . . 61

4.2 (a) Hexagonal Brillouin zone and (b) electronic band structure of t-Se 62
4.3 optical phonon matrix element for t-Se 63
4.4 orbitals orientation in t-Se and uniform displacements of band structure 65
4.5 dihedral angle conformation in Selenium 67
4.6 Simulated structure of a-Se including 50 atoms in the cell 68
4.7 Radial distribution function of a-Se 68
4.8 Volume deformation potential in t-Se and a-Se 71
4.9 Frustrated avalanche multiplication of electrons. 74
4.10 Electronic band structure of t-Se 75
4.11 The electronic band structure of t-Se along H-L-H segment. 76
4.12 Top view of the Brillouin zone in t-Se 77
4.13 Effective density of states for impact ionization 78
4.14 Density of states in t-Se and a-Se calculated using DFT. 85
4.15 Fano factor in a-Se 88

LIST OF TABLES

4.1 Lattice parameters of t-Se 60

4.2 Phonon frequencies at Γ-point of t-Se 61

4.3 Intrinsic pair creation energy (eV) in t-Se/a-Se 86

4.4 Intrinsic Fano factor for t-Se/a-Se 87

GLOSSARY OF ABREVIATIONS

t-Se.................... trigonal Selenium

a-Se................... amorphous Selenium

APD .... Avalanche photodiode

e-h .... electron-hole

FPD .... Flat panel detector

PET .... Positron emission tomography

FDG .... Fluorodeoxyglucose

MRI .... Magnetic resonance imaging

PMT .... Photomultiplier tube

IIC .... Impact ionization coefficient

LD .... Lucky drift model

DFT .... Density functional theory

GGA .... Generalized gradient approximation

LDA .... Local density approximation

RDF .... Radial distribution function

DOS .... Density of states

LIST OF PUBLICATIONS

1. A. Darbandi, O. Rubel,” Interaction of hot carriers with optical phonons in Selenium” J. Non-Cryst. Solids. **358**, 2432 (2012)

2. A. Darbandi, O. Rubel,” Single-carrier impact ionization favored by a limited band dispersion”, under review (2012)

3. A. Darbandi, É. Devoie, O. Di Matteo, and O. Rubel,” Modeling the radiation ionization energy and energy resolution of trigonal Selenium and amorphous Selenium” J. Phys: Condens. Matter **24** 455502 (2012)

1. INTRODUCTION

1.1 Crystalline and non-crystalline solids

This communication is a theoretical modeling of high-field charge transport properties in trigonal (t-Se) and amorphous (a-Se) Selenium. Selenium as a semiconductor falls into the category of condensed matter physics which is further divided into two groups, crystalline and non-crystalline ([1] Ch.1). A crystal can be defined as a material with a periodic structure. The latter is also called an ordered structure in which atoms are arranged in a repeating pattern along all directions ([6] Ch.7). As opposed to ordered structure, the materials with no periodic pattern are called disordered. The term *amorphous* has also been commonly used as a synonym for disordered materials. In general, the positions of atoms are not predictable in an amorphous solid while the atomic positions are uniquely defined in a crystalline solid ([7] Ch.1).

However, though the atomic structure of an amorphous material is not periodic, it is not entirely random either. An example of a totally random atomic distribution is an ideal gas. Fig. 1.1 illustrates the difference between a perfect structure and an amorphous structure of Selenium. Fig. 1.1a represents the lattice configuration of trigonal Selenium where atoms are arranged in a helical chains structure [8]. Fig. 1.1b is a structural model of amorphous Selenium simulated using 50 atoms in a cubic cell. It is clear from this figure that no periodic pattern can be observed in the disordered system.

More specifically, non-crystalline arrangement stands in between a completely random structure and a perfect crystalline structure. The degree of orderliness can clarify this structural difference. A long range order is observed in a structure where atoms are arranged in a repeating pattern over an infinite distance. On the other hand, a structure in which the orderliness is present only over distances comparable to the interatomic distances features the short range

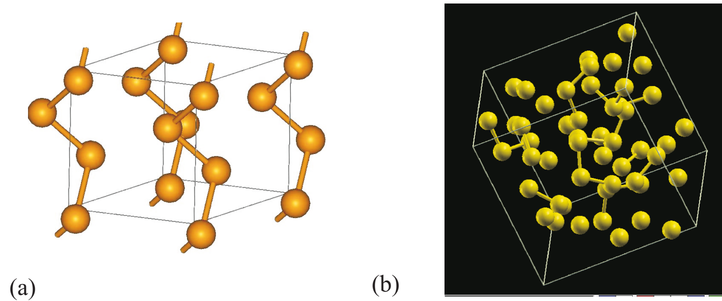

Fig. 1.1: (a) Crystalline structure of trigonal Selenium [8], (b) simulated structure of amorphous Selenium

order properties [9].

None of the long-range order and the short-range order can be seen in an ideal gas since the locations of atoms are independent of each other ([10] p. 186). Fortunately, short-range order is observed in non-crystallines and liquids due to a certain arrangement of nearest atoms ([11] Ch. 2). At the same time in non-crystalline and liquids, the orderliness of neighbouring atoms is transferred to disorderliness at long distances. In other words, the long-range order doesn't exist in these materials ([1] Ch.2).

The discussion of long-range and short-range order in Selenium helps gain a better understanding of the structural difference in t-Se and a-Se. The amorphous structure lacks translational symmetry, but it shows a degree of local correlation between atoms. This implies a short-range order. This short-range order fulfills the requirement for the electronic properties of disordered Selenium ([12] Ch.1). t-Se lattice consists of helical atomic chains (see Fig. 1.1a), where the mutual orientation of those chains preserve the periodicity of the structure. Inside the chains, the short-range order is determined by the bond length r and the bond angle θ and also the coordination number of atoms ([1] p.34). Figure. 1.2 shows the atomic configuration inside Selenium chain.

The degree of orderliness of the system in long distances can be controlled by dihedral angles and intermolecular structure ([13] p.30). The dihedral angle for crystalline Selenium is shown in Fig. 1.2. In fact, it is the variation in the dihedral angle which takes away the periodicity of a crystalline structure. Amorphous Selenium can be modeled by random selection of these dihedral angles in Selenium chains, taking into account that the bond angle and the bond length

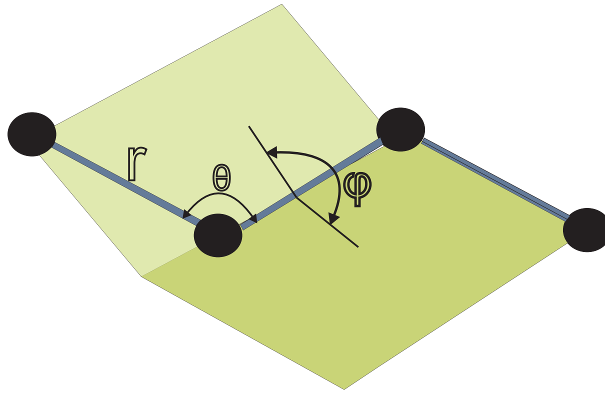

Fig. 1.2: Dihedral angle ϕ, bond angle θ, and bond length r are shown in the picture

are uniquely defined [14, 15]. In Chapter 4 the structural modeling of a-Se and the details of calculations are provided.

The physical observable that the orderliness of a structure can be inferred from is the radial distribution function (RDF) ([1] p.34). The latter is the probability of finding an atom at distance R from another atom. The extreme example of a RDF can be observed in an ideal gas where the nearest neighbors are at the same distance for all atoms due to the random relative atomic positions in an ideal gas ([12] p.19). The schematic illustration of the pair distribution function for crystalline and amorphous states are shown in Fig. 1.3a. Readily discerned from the amorphous RDF, the first few peaks are deterministic of the short range order. However, the correlation between atom pairs are lost in amorphous structure after a few interatomic spacings as a consequence of disorder ([12] p.5). The latter results in an almost uniform distribution of RDF at long distances in amorphous solids.

The distribution function for amorphous Selenium and its comparison with experiment is given in Fig. 1.3b. This a-Se structure was constructed by combination of a lattice random walk theory and *ab initio* molecular dynamics [16]. The first and second nearest neighbor peaks are evident at 2.3 Åand 3.65 Å. The orderliness is lost after $r > 4$Å. Our calculated pair distribution function will be presented in chapter 4, where we introduce our modeled amorphous structure.

Another property that characterizes a material phase is its thermodynamical state. While crystals are in equilibrium, non-crystalls possess a meta-stable phase which changes with time ([1] p.6). For instance, amorphous Selenium film starts crystallization at temperatures above

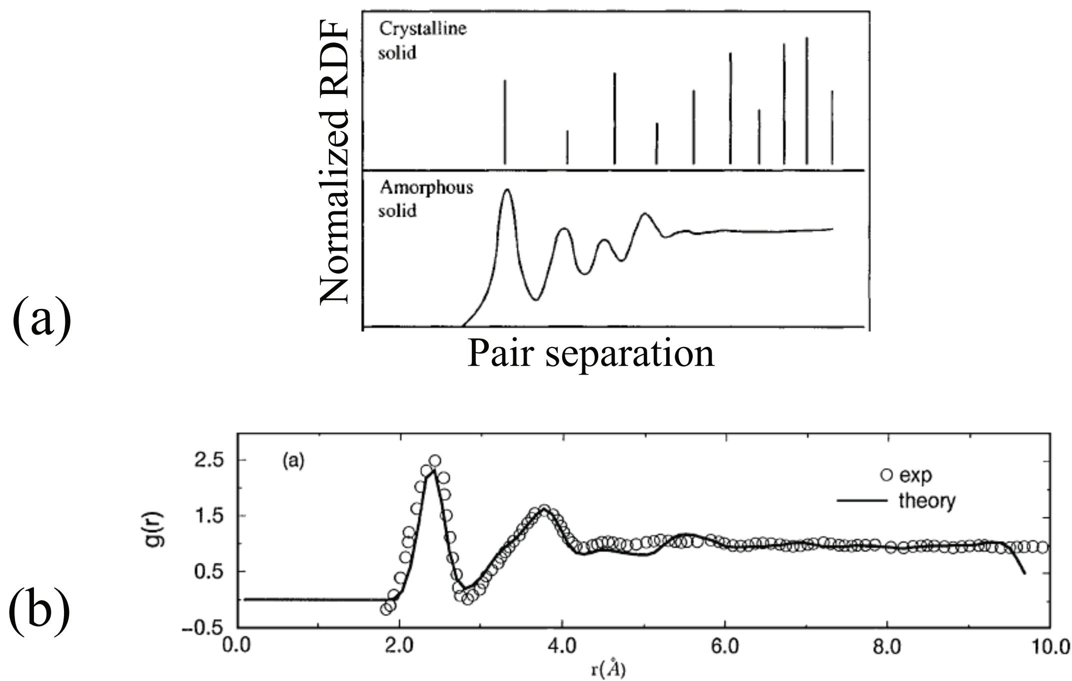

Fig. 1.3: (a) Schematic illustration of radial distribution function in crystalline and disordered solids ([12] p.5), (b) Radial distribution function in a-Se [16]

$40^{\leq}C$ [17]. The latter properties can be interpreted in terms of enthalpy H which describes the total energy of a system. A schematic diagram of H for two phases of glass and crystal is shown in figure 1.4. At room temperature, in general, crystal has the smallest enthalpy. In contrast, a glass has a minimal energy which is higher than the corresponding crystalline phase. This minimal energy is attributed to the quasi-equilibriumness of disordered materials ([1] Ch.3).

Although, the structural difference between disordered and crystalline materials was clarified here, more precisely, the disordered solids include two groups of amorphous and glass materials. According to the definition of Mott (1979) [18], a glass is a disordered solid prepared by melt quenching of a liquid while an amorphous is a disordered solid which is produced through vapour or plasma depositions. Later on, the terms *amorphous* and *glass* are used synonymously in the present study unless it is otherwise specified. Amorphous solids primarily encompasses thin films, nano-structures and gels. This project is devoted to the study of amorphous and trigonal Selenium. In the next, the interest for the latter selection is described.

Selenium is in group VI of the periodic table. These elements are referred to chalcogens.

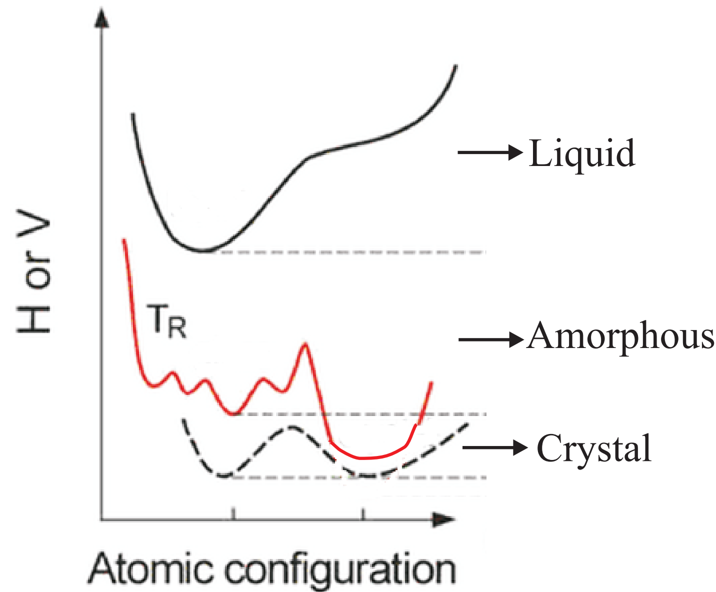

Fig. 1.4: Enthalpy of a material as a function of atomic configuration ([1] p.65)

Compounds containing at least one of Sulfur, Selenium or Tellurium are called chalcogenide materials. Chalcogenide semiconductors have had a place in the electronics industry for nearly half a century. They have found various applications from data storage devices [19, 20, 21, 22] to the medical imaging systems [23, 24, 25, 26, 27].

Historically, Selenium is one of the oldest semiconductor materials that has practical physical properties, such as photoconductivity. Willoughby Smith in 1873 discovered that the electrical resistance of selenium varies significantly with the amount of light falling on it. The photoconductivity of selenium led to a commercial method for converting images into electrical signals [28]. The latter makes Selenium an interesting semiconductor for photocell applications [29]. A significant advance in Selenium research was achieved in 1950s when the *Xerox* corporation commercialized the xerography systems using amorphous Selenium film [30]. Later on, development of scanned electrometer readouts in commercial digital chest x-ray imaging systems enabled the digitalization of the X-ray image. This readout technique provided a basis for the development of amorphous Selenium digital flat panel x-ray image detectors [25, 31, 32]. Recently, Selenium has attracted significant attention due to the observation of charge carrier avalanche multiplication in practical electric fields [33, 34]. Moreover, today's electronics mar-

ket is interested in the development of functional materials which are readily produced in the desired size and structure with low cost and high efficiency. a-Se can be readily prepared using conventional vacuum-deposition techniques with reproducible properties so that the results will be typical for any a-Se photodetector. a-Se offers the advantage of reduced cost and capability of large-area element production ([35] Ch.1). The combination of the above demonstrates the high potential of a-Se for the development of new imaging modalities.

In the following sections, first, charge carrier avalanche multiplication and its application in development of avalanche photodiodes are reviewed. Afterward, the current technological stages of a-Se in application of avalanche based and non-avalanche based detectors are discussed.

1.2 Avalanche multiplication

Two types of mobile carriers in semiconductors are holes and electrons. In a regular p-n junction photodiode, the incident photon is absorbed by the semiconductor when its energy is greater than the semiconductor's energy gap . As a result, an electron-hole pair is generated. The electrons drift toward the positive electrode and the holes drift toward the negative electrode due to the applied external voltage. Once the voltage is high enough to accelerate the charge carriers up to a certain kinetic energy, the carriers can collide with other lattice atoms to ionize them and create new electron-hole pairs ([36] Ch.4). This process is called impact ionization. The case of successive impact ionization occurs in a reverse-biased diode when the electric field increases at the depletion region. The charge carriers acquire sufficient energy to generate electron-hole pairs. These energetic secondary carriers are also able to create new e-h pairs. Thereby an avalanche of holes and electrons will travel through the semiconductor and a sudden increase of the reverse current in the diode will be observed. This process is called avalanche multiplication. ([37] p.523).

The avalanche phenomenon led to the development of avalanche photodiodes (APDs). The latter is a photodetector which converts the incident photons to electric charges, and the charges are then accelerated by a reverse bias below the breakdown voltage. As a result, the charge

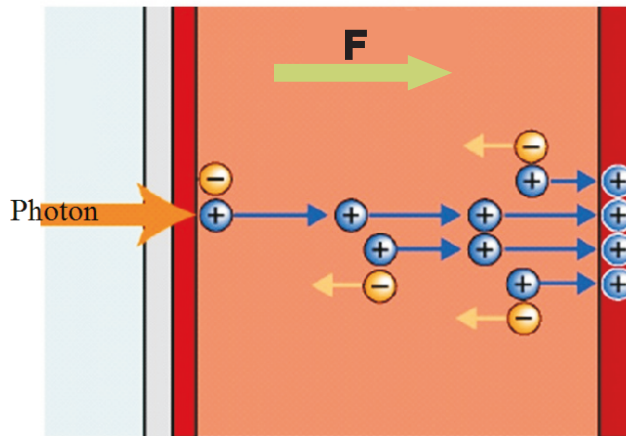

Fig. 1.5: Schematic process of holes avalanche multiplication

carriers undergo avalanche multiplication. An internal current is read out and can be enhanced further by an external amplifier ([38] Ch.13.6). The difference between an APD and a regular photodiode is that the APDs can support higher electric fields. Thus, APDs take advantage of internal gain (avalanche multiplication) and they can also measure the optical signal intensity. The amount of charge carriers generated is characterized by the avalanche gain, which is typically between tens and hundreds ([38] Ch.13.6). Fig. 1.5 illustrates a schematic graph of a linear mode avalanche process where the incident photon is absorbed, and the generated charges are multiplied during their drift across the sample ([38] Ch.13.6). APDs can be considered as an analog of photomultiplier tubes, but with higher photon detection efficiency ([39] Ch.10.3, [40] p.265).

To ensure a high quantum efficiency avalanche photodetector, the semiconductor should feature good photoconductive properties to absorb the incident photons [2]. At the same time, the material should be preferably an insulator in the dark (low dark current) [2]. Due to the stochastic nature of ionization processes, the extra noise that is always associated with the avalanche photodiodes is called excess noise (F). This noise can be calculated with the McIntyre formula [41]

$$F = kM + \left(2 - \frac{1}{M}\right)(1 - K) \quad (1.1)$$

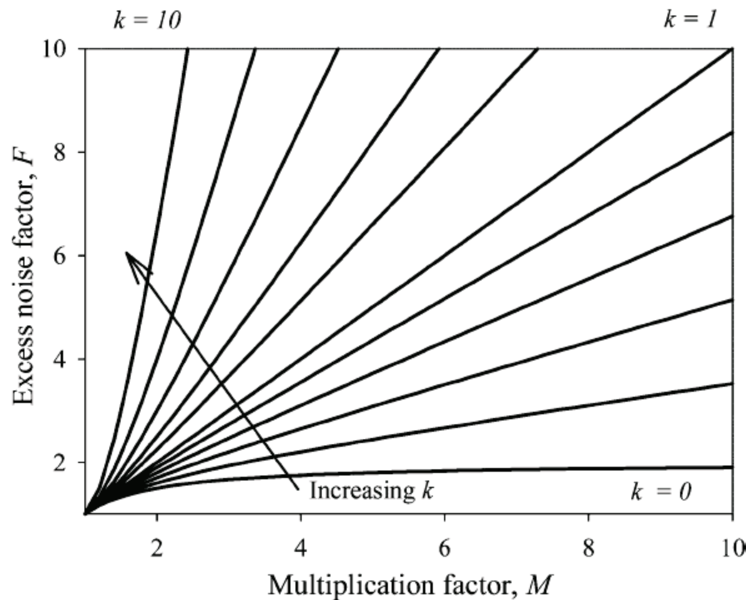

Fig. 1.6: Electron excess noise factor versus multiplication factor for different k [2]

where k is the impact ionization coefficient ratio for electrons α and holes β ($k = \beta/\alpha$), and M is the avalanche gain. Fig. 1.6 demonstrates the electron excess noise versus avalanche gain for different k factors [2]. It can be seen that the lowest electron excess noise can be obtained when $k = 0$. In this case, only electrons participate in avalanche multiplication so that the electron impact ionization coefficient α is much higher than the corresponding value for holes β. This makes the k factor very close to zero. Conversely, multiplication of both carriers, $k \ll 1$, results in higher noise in APDs. Therefore, the appropriate choice of material is critical in the development of high efficiency avalanche photodiodes. To obtain the most efficient detector, there have been numerous studies on various materials that feature avalanche multiplication.

Many studies have been done to achieve low excess noise and high gain in the technologically available semiconductors including Si, InP, $GaAs$, $Al_xIn_{1\ x}As$, $Al_xGa_{1\ x}As$, SiC, $GaInP$ and $HgCdTe$ [42, 43, 44, 45]. However each crystalline semiconductor has its own pros and cons, though the non-crystalline semiconductors present additional advantages which attract the attention of the electronics market. One of the major benefits of disordered semiconductors is the feasibility of these materials to be produced in a large area with economic cost ([35] Ch.1). Amorphous semiconductors can be prepared in thin layers to save on material cost. Another ad-

vantage is that amorphous layers can be deposited at lower temperatures than what is required for crystal growth. For instance, hydrogenated amorphous Silicon can be deposited at a very low temperature, about $80^{\leq}C$, while crystal Silicon growth requires temperature higher than $1000^{\leq}C$. This low temperature allows the use of plastic as the substrate, and as a consequence it leads to the mass production of devices such as solar panels with low cost [46].

The latter characteristics of disordered materials favour the selection of amorphous Selenium for application to photodetectors in desirable sizes with favourable costs. In addition to this, the charge transport mechanism also plays a significant role in feasibility of impact ionization in a-Se. In the next, a quick review of the electronic properties of crystalline and non-crystalline Selenium is provided. Detailed discussions of the electronic structure and band-localization of Selenium are provided in Chapter 3.

Amorphous and crystalline semiconductors share the same basic electronic and optical properties [47]. However, in contrast to crystals, there are fundamental properties associated with the disordered materials that limit the ability of amorphous semiconductors to exhibit the avalanche multiplication phenomenon. The disorder potential in amorphous selenium causes strong electron scattering and eventually electron localization, in which the wavefunction is confined to a small volume rather than being extended ([12] p.13). The wavefunction representation is illustrated in Ch. 3, where we show that the long range disorder in a-Se results in localization of the band edges. This can be inferred from analysis of density of states (DOS).

The corresponding density of states for crystal and amorphous solids is shown in figure 1.7. DOS denotes the number of electron states per unit energy per electron in a material. The shaded area in Fig 1.7b corresponds to the band tails due to the localized states. Unlike the extended states, electrons in the localized states are not free to travel anywhere in the material and therefore their mobility is limited [48].

The mobilities of charge carriers in a periodic structure are higher than ones in a disordered structure. Scattering of charge carriers from the random disorder potentials in amorphous materials limits the charge carriers drift mobilities. The hole mobility in trigonal Selenium is in the range of 6..28 cm^2/Vs while the corresponding value in amorphous phase of Selenium is about

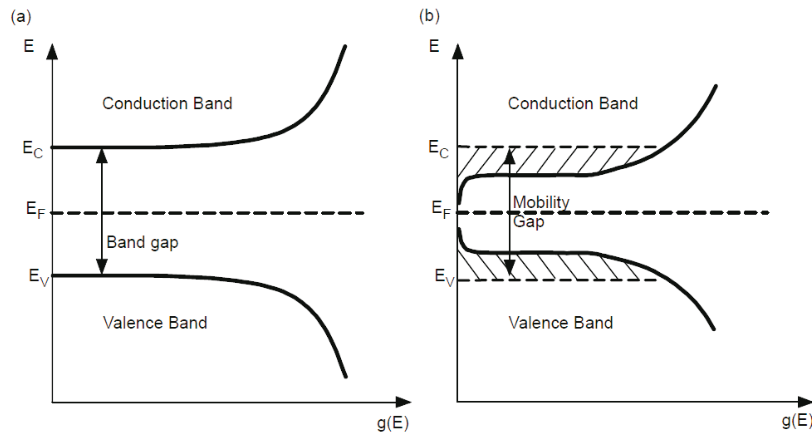

Fig. 1.7: Schematic illustration of (a) DOS of crystalline Se[48], (b) DOS models in a-Se proposed by Mott [49]

0.1 cm^2/Vs [33]. In addition to scattering with disorder potential, the electron trapping which is governed by localized states, limits the mobility of carriers in disordered solids [50]. The latter facts show that not many amorphous semiconductors are able to feature the avalanche of charge carriers. Among various amorphous semiconductors, avalanche multiplication is clearly reported only in amorphous Selenium (a-Se) at *practical electric fields* about 80 V/μm [33, 34]. However amorphous Silicon hydrogenated (a-Si:H) has been also reported to exhibit avalanche multiplication, the required high electric field about 150 V/μm [51] suppresses development of practical applications.

This avalanche phenomenon in a-Se has found a variety of applications in medical imaging systems. The next section reviews the avalanche-based and non-avalanche based amorphous Selenium photodetectors.

1.3 Application of amorphous Selenium based photodetectors in medical imaging

Today, amorphous Selenium as a photodetector is employed into two categories of imaging devices. In the first category, it is used as an x ray photoconductor in the development of direct conversion flat panel detectors (Direct FPDs) where the incident x ray is absorbed by

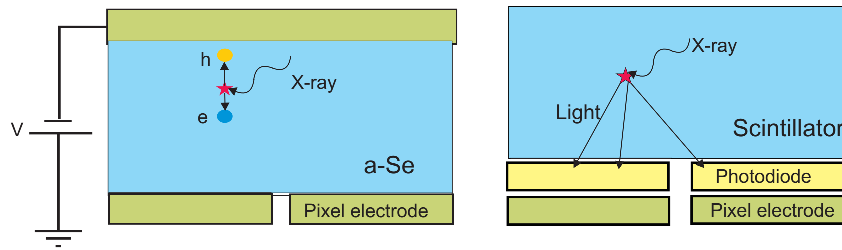

Fig. 1.8: Direct conversion a-Se based photodetector (left image), An indirect conversion photodetector (right image) .

Selenium and, it is then converted directly to electric charges (see Fig. 1.8) [52, 53, 54]. FPDs are used as imaging devices in digital radiography [55, 56] and digital mammography [57]. Other conventional FPDs utilize a scintillator such as Cesium iodide in order to convert the x ray to light. Light is then subsequently detected by the pixel photodiodes and stored in the form of electronic charge in the capacitors associated with each pixel[58] (see Fig. 1.8). The relative performance of direct and indirect digital radiographic systems influences their clinical effectiveness. Therefore a specific comparison of FPD performance is required.

The modulation transfer function (MTF) is a measure of the transfer of contrast from the subject to the image. In other words, it measures how faithfully the imager reproduces details from the object to the image produced. Direct FPD yields a superior MTF over the indirect FPD [59]. In addition, the indirect detector ends up with a degraded image and low spatial resolution due to the possible loss of photons as a result of two steps conversion processes and light scattering [59]. Fig. 1.8 illustrates direct conversion and indirect conversion based photodetectors.

The second category of a-Se detectors are based on avalanche multiplication. Avalanche multiplication in Selenium was first observed by Juska and Arlauskas in 1980 [33]. Their experiment used an a-Se sample sandwiched between two insulating layers, which prevent charge injection from the electrodes to the sample. Avalanche phenomenon in amorphous Selenium was commercialized by Tanioka [60] in 1987 through development of high gain avalanche rushing photoconductor (HARP) for TV camera tubes. Inside a HARP pick up tube, an electric field of about 100 $V/\mu m$ accelerates the holes, and the hot carriers generate additional e-h pairs by impact ionization through the a-Se layer [61]. This can provide a sensitivity of about 100 times

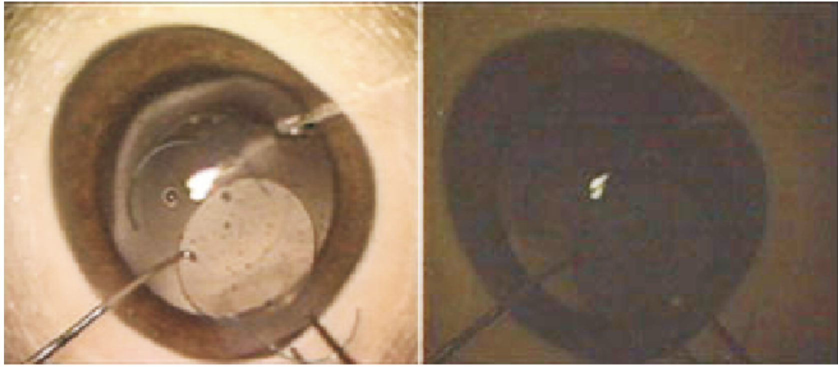

Fig. 1.9: The HARP camera (left image) is 600 times more sensitive than a standard camera (right image)[63].

greater than conventional CCD cameras. The relatively low noise produced by the avalanche process leads to a high sensitivity of the camera. Due to the internal amplification system, each incident photon results in a significant electrical output. Therefore, the HARP camera is capable of capturing bright images even at low intensity light [62].

The HARP camera also entered the medicine world. A new HARP camera which is about 600 times more sensitive than the conventional cameras can be used as the display system in ophthalmic surgeries [63]. In cataract or intraocular lens surgeries where the high intensity can cause damages to the eye's retina, the HARP camera allows the surgeon to operate at a safe low light. Fig. 1.9 shows two comparative images of an eye taken by a HARP and a conventional camera under the same light conditions.

Amorphous Selenium based avalanche photodiodes have great potentials in applications of nuclear medical imaging. Positron emission tomography (PET) is an imaging technique used to take images of functional processes in the body. A radionuclide attached to a tracer is injected into the patient. The most common tracer for PET imaging is Fluorodeoxyglucose (FDG) which carries a radioactive isotope of Fluorine-18 with a half life of 109 min on a basis of glucose [64]. The target structure of FDG is glucose metabolism cells i.e. brain and kidney. Different types of cells consume different level of FDG based on their metabolic activities. For example, cancer cells uptake more FDG than normal cells. The radionuclide in FDG undergoes a beta decay and a pair of γ rays with 511 keV energy moving in approximately opposite directions are emitted

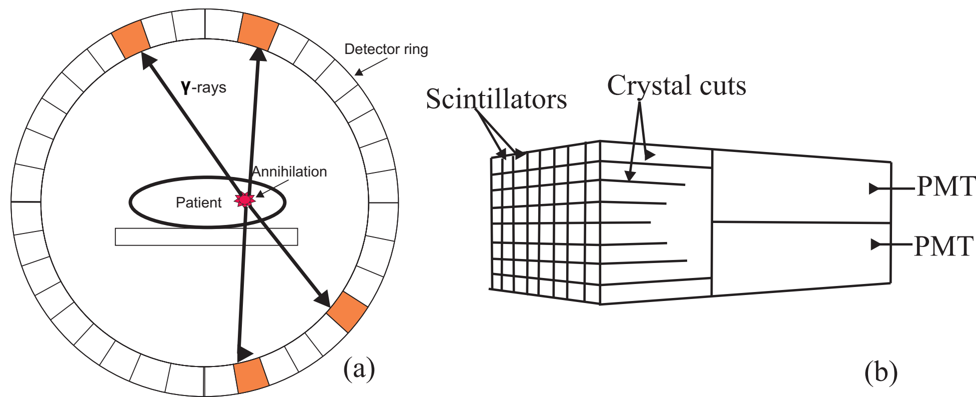

Fig. 1.10: (a) PET scanner detector ring and locating the tumor by coincident detection of pairs of gamma rays (b) block detector design involving scintillator crystall and four shared PMTs.

after the annihilation of a positron and electron ([65] Ch.1-2). PET imaging is based on the coincident detection of those pairs of γ rays [65, 66]. A PET scanner is used to evaluate cancer, blood flow, and take functional images of the organs [67, 68, 69, 70].

Figure. 1.10-a demonstrates a conventional PET detector ring which surrounds the patient. Multiple diagrams are depicted to illustrate the events rate from two coincident detectors. The location of the annihilation process in the tissue is reconstructed by means of the line of response that is assigned to each event detected ([65] Ch.1-2). A conventional photodetector design is shown in Fig. 1.10-b. Inside the detector, the γ ray is first converted to photon lights by the scintillators. These created photons are then converted to electric charges, and subsequently are multiplied through the photomultiplier tubes. The widely used scintillators in PET scanners are sodium iodide (NaI(Tl)), bismuth germanate (BGO) and cerium lutetium oxyorthosilicate (LSO) crystals [65] p.32-34.

The traditional PET detector design is a block detector which consists of a scintillator partially cut depth-wise attached to four photomultiplier tubes (see Fig. 1.10-b). The depths of the cuts yield a spatially linear distribution of light among the four PMTs ([65] p.50-54). The position at which the γ-ray strikes the scintillator is determined by Anger logic ([65] p.51). The major advantage of this design is that it allows an array of many small detector elements sharing only four PMTs instead of utilizing one PMT for each element ([40] Ch. 10).

A PET scan only provides the location of the tracer and it doesn't provide anatomical details of the organs. It is therefore essential to combine the PET imaging with computed tomography (CT) or magnetic resonance imaging (MRI) to have both anatomical and functional information. CT provides the anatomical structure while MRI differentiate between different types of tissues. A Combination of PET-CT has been already constructed and commercialized [71, 72, 73]. Development of PET-MRI is an advanced desired goal due to the absence of ionization radiation in this system and the excellent soft tissue contrast recognition of MRI [74].

Unfortunately, combining PET and MRI is challenging since the conventional PET imagers utilize PMTs which are not compatible with magnetic fields. The presence of the magnetic field in MRI machines will cause the electric charges to deviate from their paths to the PMT's dynodes.

Several approaches to develop PET-MRI have been proposed and studied. One method is to use optical fibers to transfer scintillation light outside of the MRI field of view [75]. PMTs are then placed outside the magnetic field and thus no interference between magnetic field and the metal parts of PMTs occurs [75]. However this approach degrades the overall PET performance. Another alternate approach is relied on a special magnet design where the magnet is shut down during PET data acquisition [76]. A drawback of the latter set up is its limited performance for high resolution MRI images, where a strong magnetic field is required.

The first clinical PET-MRI system has been based on avalanche photodiodes that are not sensitive to magnetic fields. APDs can replace the photomultiplier tube in PET photo-detectors [77]. Silicon APD-based PET detectors built into MRI scanners have been developed and studied for improved performance of small-animal imaging [74, 78].

Feasibility of avalanche multiplication in a-Se suggests the development of Selenium based PET detector for the purpose of combined PET-MRI systems. This design consists of a scintillator (i.e. LYSO), and an a-Se photosensor. Detected γ radiation is absorbed by the scintillator crystals and a burst of optical photons is produced, which imping on the a-Se layer. The photons are absorbed in a-Se and generate electron-hole pairs. An applied electric field above 70 V/μm causes the generated charges carriers undergo avalanche multiplication [79, 80, 81]. Therefore,

understanding the physics of avalanche multiplication in Selenium has practical importance for further achievement of this technology.

1.4 Thesis motivation and outlines

The interest in Selenium experienced a new resurgence after the observation of avalanche multiplication in a-Se. Combination of the latter with the photoconducting properties of Selenium suggested the development of avalanche based a-Se photosensors. Although numerous experimental studies have been done to investigate technological aspects of a-Se APDs, the theory of charge multiplication in disordered materials still remains a challenge.

The question is why amorphous Selenium among all other amorphous materials features avalanche process at practical electric fields.

Several theories, numerical and analytical, have been proposed to explain the impact ionization in crystalline and non-crystalline solids [82, 83, 84, 85, 86]. The latest one, the so called lucky-drift model, attempted to explain the high-field charge transport in amorphous solids [87, 88, 85, 86]. This model introduced two scattering mechanisms and tried to explain the low mobility of disordered materials by the elastic scattering processes. The impact ionization coefficients derived from this model are in good agreement with experimental results. However, this model is still not a self-sustainable theory due to the presence of free parameters (mean free paths as fitting parameters), and it lacks the predictive power.

The key to further improvement of the lucky drift model lays in analysis of the energy dependent mean free path, which is related to the scattering mechanism. This thesis aims to study the inelastic scattering process in t-Se and a-Se in an attempt to elaborate the high-field transport theory for disordered solids.

Moreover, it is attempted to understand what makes holes undergo avalanche multiplication at lower electric fields than electrons. The latter fact provides a basis to propose the single carrier multiplication in Selenium. Single carrier avalanche is a performance requirement of APDs with low excess noise. For that, the impact ionization processes were studied in t-Se using its band structure. This also provides a new perspective in order to apply Selenium electronic char-

acteristics to other semiconductors for development of novel functional materials in application of APDs.

In addition, though the low excess noise is a requirement for development of Selenium-based *avalanche detectors*, at the same time the energy resolution is another important factor for Selenium-based *direct conversion detectors*. Energy resolution can be determined by Fano factor. Therefore, the Fano factor and pair creation energy were also studied for trigonal and amorphous Selenium in this thesis.

The current chapter gives a brief introduction of amorphous and crystalline structures, the impact ionization and avalanche multiplication processes in semiconductors and an overview of applications of APDs in electronics and medical imaging. The rest of the thesis is divided into four chapters.

Chapter 2 discusses the lucky-drift model as a successful theory that describe the impact ionization in ordered and disordered materials. It will be explained how this model treats the scattering process in amorphous solids. Inelastic scattering with optical phonons is characterized as an energy loss mechanism which suppresses impact ionization. The study of electron-phonon interaction for analysis of the latter fact will be introduced.

Chapter 3 includes the methods of calculations and the framework of the project. It is explained that t-Se was undertaken for the study in this project, and the results can be extended to a-Se. In order to justify the latter assumption, a discussion of the density of states and phonon density of states in both a-Se and t-Se is provided. At the end, density functional theory is presented as the computational tool for performing the calculations.

Chapter 4 is organized in 3 sections so that it represents two published papers and one arXived communication. In the first section, the electronic structure of t-Se is calculated, and the electron-phonon interaction is studied. The corresponding matrix elements are related to the phonon scattering rate. This research is a preliminary study for development of the energy dependent lucky drift model.

In the second section, the calculated electronic dispersion of t-Se from previous section is

investigated for the impact ionization events that fulfill energy and momentum conservation principles. The reason for this work is the interesting and peculiar band structure of Selenium, which leads to single carrier impact ionization. It is suggested that this can be achieved by confinement of the excess energy range of charge carriers.

In the third section, the ionization threshold energies found in the second section are used in conjunction with the Selenium density of states in order to analyze the electron-hole pair creation energy and Fano factor in Selenium. The latter plays an important role in determination of the energy resolution in radiation detectors.

2. THEORY OF CHARGE TRANSPORT AT HIGH-FIELDS

2.1 Impact ionization in solids

Hot electrons at very high electric fields (in the range of $20..200V/\mu m$) show a different charge transport properties than that observed at low fields. A charge carrier accelerates in the electric field and gains kinetic energy $W = qFd$, where F is the applied field, q is the electric charge, and d is the distance that the carrier drifts. Once the carrier gains an excess energy greater than the binding energy of a valence electron, it can collide with the lattice atoms and breaks the covalent bond to produce an electron-hole pair [84]. This process is called impact ionization, and it is characterized by the impact ionization coefficient (IIC), α, which is the number of e-h pairs generated by a mobile carrier per unit length in the applied field [82]. The secondary charges have also the potential to initiate impact ionization. As a result of successive impact ionization, the avalanche multiplication of electric charges occurs in the circuit. The acquired reverse current in the circuit is characterized by the multiplication factor or current gain M, which is defined as the ratio of total current to the injected current.

The theory of secondary ionization was motivated by McKay and McAfee's experiments on Silicon and Germanium p-n junctions [89], where they observed charge multiplication below the breakdown voltage. To explain this phenomenon, Wolff [90] translated the gas discharge theory into the breakdown process in the solid state p-n junctions. He used the Boltzmann equation which governs the distribution of electrons at high electric fields. Calculation of this distribution function for a real band semiconductor is not straightforward. Therefore, Wolff neglected the real band structure of Silicon and approximated spherical, non-degenerate energy bands with equal masses for electrons and holes [90]. As a result, he obtained the ionization

coefficient varied with electric field in

$$\alpha \propto \exp(\ \frac{b}{F^2}) \tag{2.1}$$

where b is a fitting parameter. However, when Wolff fitted his calculated IIC curve on an experimental data for Silicon, there were two objections to his theory. First, this model is over simplified and the parabolic band structure is not a valid assumption for bands remote from the band edge. Second, Wolff assumed that the impact ionization is attributed to the electrons at *equilibrium* distribution, although impact ionization is more likely associated with the energetic *non-equilibrium* electrons [82].

To improve Wolff's theory, Shockly provided his model in 1961 [84]. He modified the Wolff theory by introducing the ionization probability distribution in the context of lucky electrons. He proposed that if an electron obtains sufficient threshold energy E_i it is able to generate an electron-hole pair via the impact ionization process. To do so, the carrier should gain the required energy in a ballistic motion. In such a motion the electron avoids any scattering events until it reaches the ionization threshold energy [87]. The distance that such a carrier travels is characterized by the mean free path λ. The Shockley's ionization coefficient is then given by

$$\alpha = \frac{eF}{E_i} \exp(\ \frac{E_i}{e\lambda F}). \tag{2.2}$$

where F is the applied field. Shockley's ionization coefficient shows a field dependence behavior similar to the formula obtained empirically

$$\alpha = \alpha_0 \exp(\ \frac{F_0}{F}) \tag{2.3}$$

where α_0 and F_0 are parameters to be fitted using experimental data.

The lucky electron model gives no explanation to the quantitative value of ionization threshold energy [87]. It is kept as a fitting parameter. In addition, the main objection to his theory is

that Schockley assumed that the electrons gain excess energy during their ballistic motions [82]. In this type of motion, the charge carrier travels a distance of $\lambda_i = \frac{E_i}{eF}$ avoiding any scattering until its energy reaches E_i. The path between two optical phonon collisions is about $4..7nm$ in major semiconductors [91, 92, 93]. Given the ionization threshold energy is equal to the band gap energy in crystalline semiconductors, and using the range of electric field in which avalanche multiplication is observed, one can see that $\frac{\lambda_i}{\lambda_{op}} \approx 10..20$. This great ratio of $\frac{\lambda_i}{\lambda_{op}}$ does not let electrons move ballistically without scattering. Based on the latter interpretation, this theory does not provide enough ballistic electrons to cause avalanche multiplication to explain the experiments. Therefore, a better model was required.

Baraff introduced his numerical model in 1962 [83]. To understand his approach, consider an electric field applied to a group of electrons with energy equal to zero. Electrons start moving and they undergo collisions with phonons and other electrons during their drifts in the semiconductor. The key assumptions of Baraff's theory are [88]: 1. Charge carriers gain kinetic energy by drifting in the applied electric field. 2. Charge carriers undergo *elastic collisions* which are characterized by the energy independent elastic mean free path λ_m. 3. Charge carriers undergo *inelastic collisions* if their kinetic energy becomes greater than optical phonon energy E_{op}. The latter is also characterized by the same mean free path as the elastic one, $\lambda_m = \lambda_{op}$. 4. Scattering events are isotropic. 5. Once the carrier's kinetic energy reaches ionization threshold energy, E_i, impact ionization is initiated.

Baraff converted the Boltzmann transport equation to an integral equation for the space and energy dependent collision density [83]. He solved this integral numerically to obtain the impact ionization coefficient. As a consequence of Baraff's work, it turned out that neither of Shockley's model nor Wolff's theory are valid. The electrons distribution function is too sharp for Wolff's approximation at high electric fields [83], and electrons are drifting in the field rather than following Shockley's ballistic motion [94]. Baraff's theory has been a great point of interest for experimentalists because of its remarkable fit to the experimental results [82]. The next sections describe the further improvement of the lucky drift model for crystalline and

noncrystalline solids.

2.2 Lucky drift model in crystalline solids

The theory of impact ionization in crystalline semiconductors was well established with development of the lucky-drift model by Ridley in 1983 [82]. This theory replaced Baraff's numerical approach with an analytical method. Ridley's lucky drift model was successful to reproduce Braff's curves. The main key to the lucky-drift model is understanding the specific distinction between the rate of momentum relaxation and energy relaxation. After *elastic scattering*, the electron relaxes its momentum without relaxing its energy. On the other hand, after *inelastic scattering*, both momentum and energy of carrier are relaxed.

It is more probable that electrons undergo momentum relaxing collisions than energy relaxing ones ([95] p.84). The latter can be expressed in terms of $\tau_m < \tau_E$, where τ_m and τ_E are momentum relaxation and energy relaxation time constants respectively [82]. In general, if t is the time associated with the carrier's motion, the lucky drift model can be stated as $\tau_m < t < \tau_E$. It is clear that the case $0 < t < \tau_m$ recovers Shockly's ballistic motion that electrons avoid any collisions.

In conclusion, the concept of lucky electrons in this theory refers to those carriers which relax their momentums ($\tau_m < t$), but avoid any energy relaxation collisions ($t < \tau_E$). In other words, this model let electrons reach the ionization threshold energy by drifting instead of moving ballistically. Only lucky electrons take part in impact ionization, and the contribution of unlucky electrons, which are in a steady state, are neglected [82].

2.3 Lucky drift model in disordered materials

The fundamental works of Wolff [90], Shockley [84] and Baraff [83] provided a solid basis for high-field charge carrier transport in crystalline semiconductors. The theory of high-field transport was advanced further by Ridley's drift model [82].

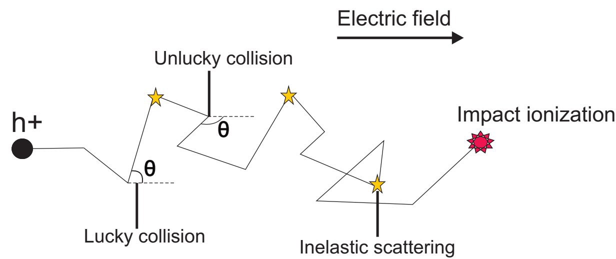

Fig. 2.1: Carrier trajectory with relevant elastic and inelastic scattering [3].

Observation of avalanche multiplication in amorphous solids (i.e. a-Se, a-Si:H) [34, 96, 51] required a theory to explain the impact ionization of carriers in disordered materials. It was widely believed that the latter phenomenon is inherent only to crystalline semiconductors where the carriers mobility is higher than that in amorphous semiconductors. Arkhipov *et al* in 2000 attempted to apply Shockley's theory to interpret the field dependence of the impact ionization coefficient in a-Se [97]. His work resulted in an unrealistic value of E_i = 0.55 eV while the energy gap of a-Se is about 2eV. Therefore, Rubel *et al* [87] and Kasap *et al* [85] were inspired to modify Ridley's lucky drift model in order to develop a theory that is applicable to amorphous solids as well. Next, this modified LD model is described.

In the original lucky drift model only scattering with phonons was considered. As it was explained in the first chapter, the disorder is the characteristic that distinguish an amorphous from a crystal structure. The lucky drift model was extended to amorphous semiconductors by taking into account the role of this disorder in charge transport. The collision of electrons with both phonons and disorder potentials is considered [87]. It is assumed that scattering on disorder potential is the dominant mechanism of the momentum relaxation of hot carriers in amorphous semiconductors [3].

Figure 2.1 illustrates a schematic trajectory of a charge carrier drifting in the electric field. The lucky and unlucky events are defined as follow. Unlucky carriers are those whose velocities have a negative projection on the field direction after scattering ($\theta > \pi/2$), and hence the carriers lose their kinetic energies by traveling against the field [87]. On the other hand, lucky carriers with scattering angle $\theta < \pi/2$ gain energy from the field after collisions and they have oppor-

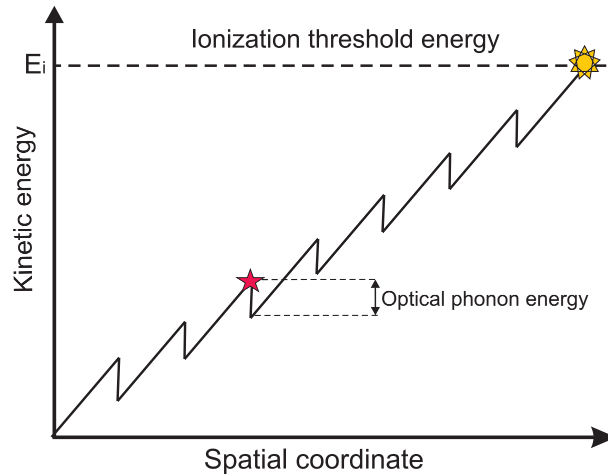

Fig. 2.2: Carrier kinetic energy diagram. Scattering with optical phonon results into an energy loss corresponding to the phonon energy [88] .

tunity to build up their energies up to E_i for initiating impact ionization. Elastic and inelastic scattering are characterized by the energy independent mean free paths λ_d and λ_E respectively.

λ_d is associated with interaction of electrons with the disorder potential and acoustical phonon. Acoustical modes represent a lower frequency than optical modes. The acoustic modes energy in Selenium are about 5   10 meV and the optical modes are about 30 meV [98]. Due to the small energy of acoustic phonons with respect to the lattice thermal energy that is about 25 meV at room temperature, the equipartition approximation can be assumed for acoustic phonon scattering. According to this approximation, the scattering rates are the same for either phonon absorption or phonon emission. Therefore the energy exchange rate remains almost constant in scattering with acoustic phonons (See ref [99]page 470). The latter discussion let us assume that the acoustical phonons do not provide significant contribution in energy loss mechanism.

On the other hand, each collision with optical phonons changes the kinetic energy of a carrier by E_{op}. The particle's energy $E = qFd$ reduces to $E = qFd \quad E_R$ after a phonon emission scattering (see Fig. 2.2). A carriers initiates impact ionization immediately after it builds up its kinetic energy to the ionization threshold energy.

Scattering with optical phonons is the only energy loss mechanism that controls the energy exchange rate in semiconductors. This interaction is responsible for full energy relaxation of charge carriers. The energy relaxation time τ_E in crystalline semiconductor is the sum of optical

phonon relaxation times [88].

$$\tau_E = \frac{E}{\hbar\omega_{op}}\tau_{op} \tag{2.4}$$

where $E/\hbar\omega_{op}$ is the number of released phonons. A parameter $\gamma = \lambda_{op}/\lambda_m$ was introduced in order to account for $\tau_m \gg \tau_{op}$ in amorphous solids. Thereby, the energy relaxation was modified to [88]

$$\tau_E = \frac{E}{\hbar\omega_{op}}\gamma\tau_{op} \tag{2.5}$$

Using Eq. 2.5, the energy relaxation mean free path can be derived from $\lambda_E = v_d(E)\tau_E(E)$, where $v_d(E)$ is the group velocity [88]

$$\lambda_E = \frac{e\gamma\lambda_m^2 F}{2\hbar\omega_{op}} \tag{2.6}$$

Equation 2.6 leads to the calculation of ionization coefficient for disordered materials. Figure 2.3 shows that the fitted calculated α for Selenium using this model is in agreement with the experimental results. In this modified lucky drift theory, the ionization threshold energy E_i, and the mean free paths λ_m and λ_{op} are the adjustable parameters.

Although the modified theory agrees with the experiments remarkably well, there are still challenges being to overcome. It is clear from Figure 2.3 that the theory predicts a stronger dependence of the impact ionization coefficient on the electric field than what is observed experimentally. In addition, the existence of mean free paths as adjustable parameters reduces the self sustainability of the theory. The latter parameters are inspected by fitting the experimental data. However, the best fit is achieved once the energy dependence of mean free paths is considered [85]. Therefore, analysis of carriers energy loss transition is essential in order to develop a parameter-free theory for impact ionization in a-Se. The next section introduces electron-phonon interaction, which is used to study the charge carriers scattering rate.

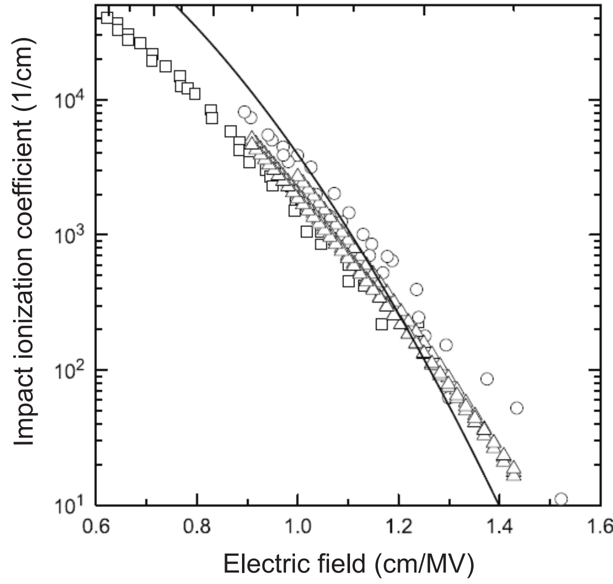

Fig. 2.3: The impact ionization coefficient in a-Se as a function of the inverse electric field. Symbols represent the experimental data from various authors and the solid line is the theoretical fit [88]

2.4 Electron-phonon interaction

Atoms are not fixed at defined places in a real semiconductor and they are constantly vibrating. Each certain type of these atomic motions, that are characterized by the direction and frequency of oscillating atoms, is called phonon ([100] Ch. 4). Dispersion of Phonons can be derived by solving the equations of motion for adjacent atoms in a lattice. The numerical calculation of phonon modes in Selenium is presented in chapter 4.

Phonon vibrations modify the electron behavior in a solid. A certain vibration of atoms causes a modification in the potential that is screened by electrons. This potential is associated with a spatial dependence of the same form as that of the lattice vibration. The latter potential (deformation potential) enter the electron Hamiltonian and gives a coupling between the electrons and phonons ([100] Ch. 4). This interaction is described as ([101] p.132)

$$H_{ep} = \Xi_{n\mathbf{k}} \frac{\mathbf{u_q}}{a} \tag{2.7}$$

where H_{ep} is the electron phonon Hamiltonian, $\mathbf{u_q}$ represents the phonon displacement vector, a is the lattice constant, and $\Xi_{n\mathbf{k}}$ is the deformation potential.

The coupling between electron and phonon is mainly associated with acoustic phonons for a carrier with an excess energy below 25 meV. Charge carriers start to lose energy to optical phonons as they get to higher excess energy ([102] Ch. 4). A further analysis of electrons coupling to *acoustic* phonons is provided in Ch.4 through discussion of a volume deformation potential in amorphous Selenium. Here, the coupling of carriers to *optical* phonons and the corresponding energy loss rate is discussed.

The scattering rate due to absorption and emission of a phonon can be obtained through Fermi's Golden rule. Fermi's golden rule gives the probability of transition of electrons per unit time from one state of energy into another state due to a perturbation in the system. This transition rate is given by ([100] p. 414)

$$R_{i\propto f} = \frac{2\pi}{\hbar}\left|M_{if}\right|^2 \rho_f \tag{2.8}$$

where $R_{i\propto f}$ is the transition rate from the initial eigenstate i into the final state f, ρ_f is the density of final states which takes into account the degeneracy of eigenstates, and $\left|M_{if}\right|$ is the electron-phonon matrix element. Eq. 2.8 can be modified to

$$R_{i\propto f} = \frac{2\pi}{\hbar}\sum_{\mathbf{k},n,l,\mp} \left|\langle f|V_{e-p}|i\rangle\right|^2 \delta(E_f - E_i) \tag{2.9}$$

where $\mp$ includes both phonon absorption and emission, and the summation takes into account the matrix elements of all initial and final Bloch states, $|i_{n\mathbf{k}}\rangle$ and $|f_{n'\mathbf{k}'}\rangle$ in bands n and n', with momentums $\mathbf{k}$ and $\mathbf{k}'$ before and after scattering respectively. l indicates the summation over all phonon modes, and delta function holds the energy conservation principle during scattering. The energy of the initial state is

$$E_i = \epsilon_{n\mathbf{k}} \tag{2.10}$$

and the energy of the final state after emission or absorption of an optical phonon with energy

$\hbar\omega_l$ is

$$E_f = \epsilon_{n'\mathbf{k}'} \mp \hbar\omega_l \tag{2.11}$$

The electron phonon matrix elements in Selenium with six optical modes and three atoms per unit cell is then given by [103]

$$V_{e-p} = \sum_{l=1}^{6}\sum_{\tau=1}^{3}\sqrt{\frac{\hbar}{2m\omega_l}}\left\{a_l\mathbf{u}_{l\tau} + a_l^{\dagger}\mathbf{u}_{l\tau}^{\pm}\right\}.\frac{\partial V_e}{\partial r_\tau} \tag{2.12}$$

where a_l and $a_l^{\dagger}$ are the phonon absorption and emission operators respectively. $\mathbf{u}_{l\tau}$ and $\mathbf{u}_{l\tau}^{\pm}$ are the corresponding phonon displacement vectors, and $\frac{\partial V_e}{\partial r_\tau}$ is the derivative of the electronic potential with respect to the displacement of atom τ. Using Eq.(2.12), the electron phonon interaction matrix element in Eq.(2.9) can be formulated as

$$\langle f|V_{e-p}|i\rangle = \sum_{l=1}^{6}\sum_{\tau=1}^{3}\sqrt{\frac{\hbar}{2m\omega_l}}\left\{a_l\mathbf{u}_{l\tau} + a_l^{\dagger}\mathbf{u}_{l\tau}^{\pm}\right\}\times\mathbf{H}^{\tau}_{\mathbf{k}\mathbf{k}',nn'} \tag{2.13}$$

where $\mathbf{H}^{\tau}_{\mathbf{k}\mathbf{k}',nn'} = \langle f|\frac{\partial V_e}{\partial r_\tau}|i\rangle$ is the atom specific matrix element that can be calculated directly from density functional theory. Density functional theory will be discussed in Ch. 3. $H^{\tau\alpha}_{\mathbf{k}\mathbf{k}',nn'}$ describes the change in the potential caused by displacement of atom τ in direction α. Combining Eq.(2.13) with Eq.(2.9), the carrier scattering rate from state $|n\mathbf{k}\rangle$ into all $|n'\mathbf{k}'\rangle$ by phonon absorption can be evaluated by [103]

$$R_{n\mathbf{k}}(e_{n\mathbf{k}}) = \frac{\pi}{m\omega_l}\sum_{\mathbf{k}'}\sum_{l=1}^{6}\sum_{\tau=1}^{3}\left|\mathbf{u}^{l\tau}_{(\mathbf{k}-\mathbf{k}')}\times\mathbf{H}^{\tau}_{\mathbf{k}\mathbf{k}',nn'}\right|^2 * n(e_{n'\mathbf{k}'} - e_{n\mathbf{k}}) \tag{2.14}$$

where $\mathbf{u}^{l\tau}_{(\mathbf{k}-\mathbf{k}')}$ is phonon displacement vector with momentum $\mathbf{q} = \mathbf{k} - \mathbf{k}'$, and n_ϵ is the phonon density of states which is given by the Bose-Einstein distribution at temperature T [103]

$$n_l = \frac{1}{e^{\hbar\omega_l/k_BT} - 1} \tag{2.15}$$

A similar equation can be derived for phonon emission collisions [103]

$$R^{+}_{n\mathbf{k}}(e_{n\mathbf{k}}) = \frac{\pi}{m\omega_l} \sum_{\mathbf{k}'} \sum_{l=1}^{6} \sum_{\tau=1}^{3} \sqrt{\mathbf{u}^{l\tau}_{(\mathbf{k}\ \ \mathbf{k}')} \times \mathbf{H}^{\tau}_{\mathbf{k}\mathbf{k}',nn'}}^{2} * \ [n(e_{n\mathbf{k}} \quad e_{n'\mathbf{k}'}) + 1] \tag{2.16}$$

The total scattering rate is the sum of phonon emission and absorption rates

$$R_{n\mathbf{k}}(\epsilon_{n\mathbf{k}}) = R_{n\mathbf{k}}(\epsilon_{n\mathbf{k}}) + R^{+}_{n\mathbf{k}}(\epsilon_{n\mathbf{k}}) \tag{2.17}$$

In an attempt to modify the lucky drift model for amorphous Selenium, the best fit to the experimental data was obtained by assuming an energy dependent mean free path, however the quantitative insight into this dependence remained a question [85]. Therefore, the analysis of optical phonon scattering in Eq. 2.17 is an essential part to understand the energy dependence of the mean free paths, and to develop this model for amorphous solids.

The most important component of Eq. 2.14 and Eq. 2.16 is the electron-phonon matrix elements. The corresponding calculation for t-Se is presented in Ch. 4. Though the latter calculations are performed for trigonal Selenium, Ch. 3. justifies the validity of results to be also extended to amorphous Selenium.

3. METHODS AND FRAMEWORKS

3.1 *Electronic properties of crystalline and amorphous Selenium*

Ordered solids which benefit from periodicity in their structures can be analyzed theoretically through the study of their unit cells. The electronic properties calculated based on these unit cells can be applied to the whole corresponding solid since the super-cells are constructed via repeating those unit cells in a certain pattern.

Unfortunately, disordered systems raise a complexity in theoretical calculations. Unit cell is not defined due to the lack of periodicity and symmetry in amorphous structures. Therefore, for analysis of electronic properties of an amorphous material, a large sample of atoms that resemble a disordered structure is needed. Moreover, simulating a theoretical amorphous sample is a time consuming effort for structural optimization and atomic force relaxations. There have been various studies for simulation of amorphous Selenium using Monte Carlo simulation and *ab initio* molecular dynamics [104, 14, 105, 16].

Here, we use another approach for Selenium that reduces those technical difficulties. We suggest to study a periodic lattice and the outcome is also translatable to the non-periodic Selenium. In the following, the density of states, phonon density and the electronic structure of both ordered and disordered Selenium are compared and their similarities are discussed to justify our assumption.

A criticism to our assumption could be the different charge carrier mobilities in a-Se and t-Se [106, 107]. To address this question, we should clarify that the low mobility of carriers in a-Se is attributed to the carriers momentum relaxation due to *elastic* interaction with disorder potentials. However, the part of mobility that is controlled by electron-phonon interaction is the same for the amorphous and crystalline state of a material ([108] and [102] p. 161). The latter

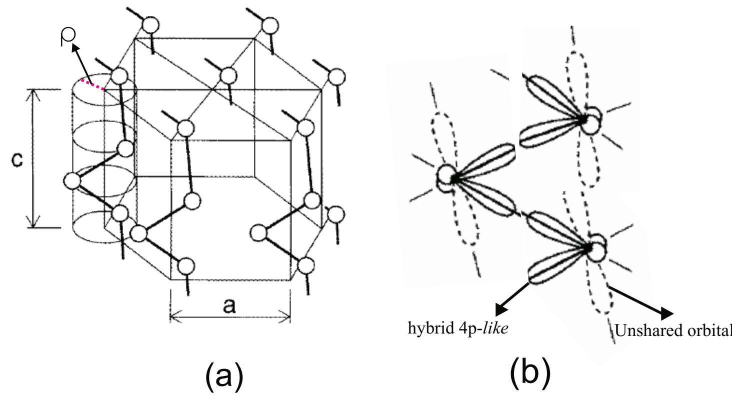

Fig. 3.1: (a) Crystal structure of trigonal Selenium, and (b) the arrangement of hybrid 4p-*like* and unshared LP orbitals[4]

allows us to suggest an analysis of the electron-phonon mechanism in t-Se, and to interpolate the results toward a-Se without concerning about the mobilities.

3.2 Electronic structure of crystalline and amorphous Selenium

The most thermodynamically stable and dense allotropic form of selenium is trigonal Selenium with a melting point about $217^{\leq}C$ [109, 110]. t-Se has a hexagonal crystal lattice which consists of helical chains oriented along the c-axis. The unit cell contains three atoms covalently bonded to two neighbouring atoms [111]. The chains are held together by a Van der Waals type bonding. The crystal structure of Selenium is shown in Figure 3.1(a). The corresponding atomic structure will be discussed in detail in the next chapter.

The orbital configuration of Selenium is $4s^2 4p^4$, which provides 6 valence electrons. Core electrons are not involved in chemical bonding. When atoms combine to form a solid, the electron interaction splits the valence states into bonding and anti-bonding states. Bonding configuration of Silicon and Selenium after hybridization is illustrated in figure 3.2. This provides a better understanding of electronic structure of chalcogenide materials.

Four Silicon valence electrons form sp^3 orbitals which bond to adjacent atoms. It is not always possible to arrange all the valence electrons in bonding orbitals since four is the maximum number of orbitals that can be made from s and p states [13]. In Selenium, which has

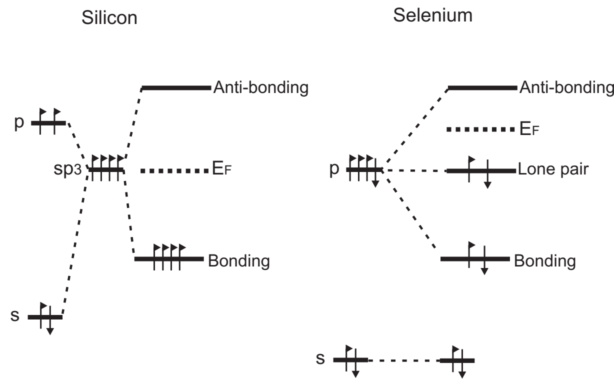

Fig. 3.2: Bonding configuration of Silicon and Selenium atoms constructed from hybridized orbitals [12]

six valence electrons, sp^3 hybridization is not the lowest energy configuration. Instead of hybridization, two electrons of s state lie deep in the energy configuration, and two electrons of p state will form the covalent bond, splitting into bonding and antibonding states (See Fig. 3.2). The remaining two electrons of p state contribute in forming the lone pair state (LP), which lies in energy range between the bonding and anti-bonding states (Fig. 3.2) [112]. These LP states remain unshared and do not participate in chemical bonding [12].

Arrangement of hybrid $4p$ *like* and unshared LP orbitals in Selenium is shown in figure 3.1(b). The existence of this lone pair state is inherent in chalcogenide materials [113]. The presence of these states in Selenium and their weak electronic interactions result in favourable charge transport for avalanche multiplication of holes. More detailed discussion is provided in the next chapter.

The behavior of electrons in a solid can be determined by means of an energy-momentum dispersion called the electronic band structure. The latter describes the available eigenstates of energy in the momentum space, which are created after hybridization ([101] p. 17). A schematic representation of the band structure in semiconductors is given in figure 3.3. A fundamental property of semiconductors is the presence of an energy gap separating the anti-bonding states (conduction bands) from the bonding states (valence bands). This forbidden gap in Selenium can be measured by luminescence method or optical absorption techniques [114, 115].

In amorphous materials, the band edges are replaced by a broadened tail of states which are extended into the forbidden gap. In other words, *localized states* which are the eigenstates of

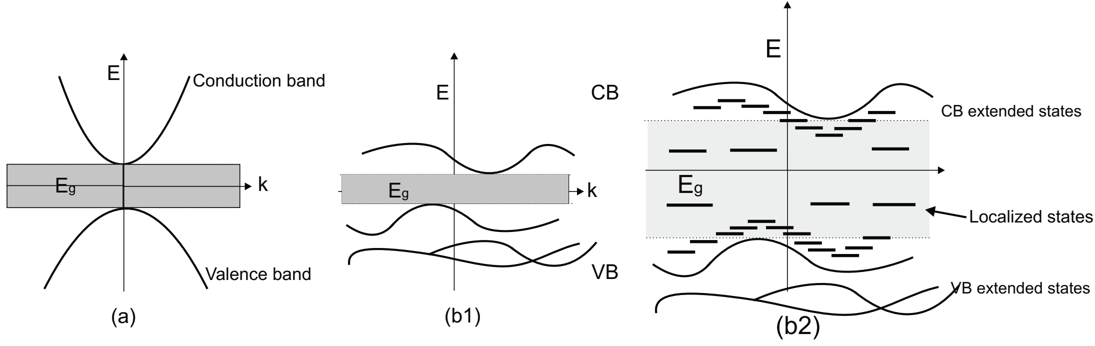

Fig. 3.3: (a) Simple band structure of direct gap semiconductor with a parabolic approximation. (b) Schematic representation of a realistic band structure for an indirect gap semiconductor, (b1) illustrates a crystal and (b2) illustrates an amorphous structure.

the disordered potentials, replace the extended states in non-crystalline semiconductors ([116] Ch.3), and consequently modify the mobility gap and the charge transport properties. Figure 3.3 visualizes our discussion by comparing the band structure of a crystalline semiconductor with an amorphous one.

Band structure is the dispersion of energy states in momentum space $p = \hbar k$ where k is the wave-number. The wave-functions of those electronic states are the solutions to the Schrodinger's equation

$$\frac{\hbar^2}{2m}\dagger^2\psi + V(\mathbf{r})\psi = E\psi \tag{3.1}$$

where E is the electron energy and V_r is the potential energy. The Bloch function is a solution for the periodic potential in ordered crystals. (See Ch.2 [117] for further details)

$$\psi(\mathbf{r}) = U(\mathbf{r})\exp(i\mathbf{k}.\mathbf{r}) \tag{3.2}$$

This wavefunction has a well defined momentum k. It is widely believed that the momentum k is no longer a good quantum number in amorphous structures due to the lack of periodic potentials in these materials (See Ch.6 [118], and Ch.10 [119]). In other words, the Bloch solution for the Schrodinger equation does not apply to amorphous semiconductors because the electronic potential is not periodic anymore. As a consequence, according to this argument the

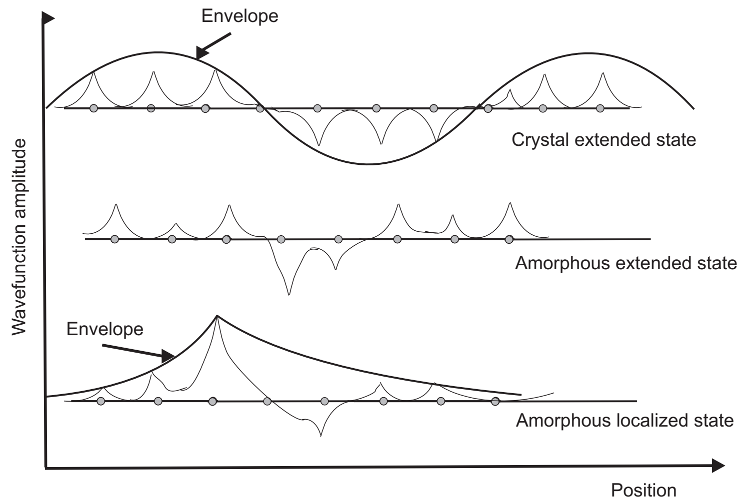

Fig. 3.4: Illustration of extended states and localized state wavefunctions in crystal and amorphous [12]

disordered solids do not feature band dispersion.

Electronic band dispersion is used for analysis of the impact ionization process inside the Brillouin zone. The numerical simulation of this process is studied and is discussed in the next chapter. Although it is necessary to explain how our initial assumption about similar charge transport in t-Se and a-Se is still valid despite the arguments against the existence of band dispersion in a-Se.

A more detailed analysis of the electronic structure of crystalline and non-crystalline materials reveals a different perspective. Wavefunctions of the extended and *localized states* in amorphous and crystal phases are illustrated in figure 3.4. In crystal, the wavefunction is extended throughout the crystal with a constant phase change. However no periodic function for *localized states* can be defined due to the presence of the disorder, the dispersion of the extended states wavefunctions for crystalline and amorphous Selenium are comparable [12]. This leads to the fact that the momentum may not be a valid quantum number for the *localized states*, but it still applies to the extended states in the amorphous structure.

A more quantitative discussion can be provided by studying the bonding properties. The electronic bands are most strongly influenced by the chemical bonding and the short range order [120], and these bonding types and the short range order are similar in both disordered and ordered materials. The absence of periodicity in amorphous structure can be considered as

a small perturbation [12]. The latter was clearly stated by Weaire and Thorpe in 1971 through a tight binding Hamiltonian for Silicon bonding [121, 122]. They showed that the interacting wavefunctions have the form of $\psi_{ij}|\rangle\psi_{i'j'}$ which involves the information of atoms in the same bond. Hence, describing Hamiltonian includes only the short range bonding and it contains no information about the long range order. In better word, both amorphous and crystalline phases can be described by the same Hamiltonian.

In conclusion, the preservation of the short range order in non-crystalline solids leads to a similar electronic dispersion of extended states for both amorphous and crystalline solids (See Fig. 3.3) ([12] p.10). Taking advantage of the latter fact, we propose to perform the calculations of electron-phonon interaction based on the crystalline Selenium structure. This lets us avoid the complexity of modeling a disordered structure.

Although the structural properties of a-Se and t-Se favours our assumption, detailed analysis of density of states and phonon density of states are required. These quantities enter the electron-phonon interaction through Eq. 2.16.

3.3 Density of states of crystalline and amorphous Selenium

According to Eq. 2.8 and Eq. 2.16, calculations of the electron-phonon interaction include information of the density of states (DOS) and the phonon dispersion (PDOS). Different DOS and PDOS in crystal and non-crystal can result in a different electron-phonon mechanism in these materials. In the following, it is justified that the similarity of DOS and PDOS in both crystalline and amorphous Selenium favours our suggestion in extending the electron-phonon interaction results from t-Se to a-Se.

Density of states is defined as the number of available states at each energy level to be occupied by electrons. In analysis of the optical phonon scattering, Fermi's golden rule (Eq. 2.9) takes into account the scattering of electron from band n with momentum k, which is represented by state $nk|$, to the state $n'k'|$. According to this relation, if the density of these initial and final states in t-Se is different from that in a-Se, calculations of crystalline Se will be different from

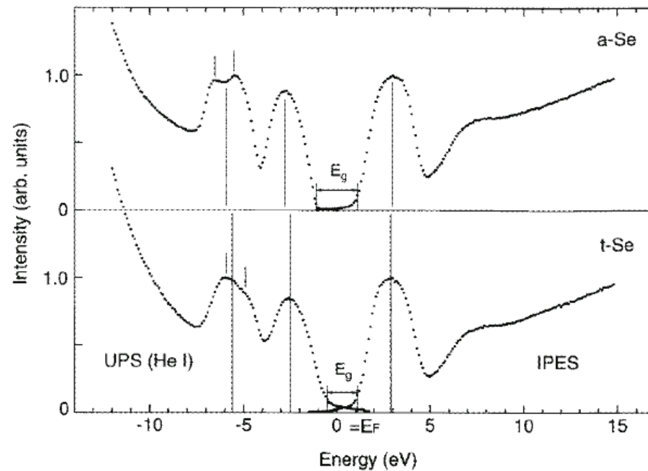

Fig. 3.5: a-Se and t-Se density of states [4]

that of the a-Se, and it cannot be translated into disordered structure.

Several studies have been done to determine the density of states of t-Se and a-Se [123, 124, 125, 126, 127, 4]. Valence band and conduction band spectra have been measured by means of ultraviolet photoemission spectroscopy (UPS) and inverse photoemission spectroscopy (IPES) [4]. Photoemission spectroscopy is based on the photoelectric effect. The material of interest is first exposed to a beam of ultraviolet or x-ray radiation, which ionizes electrons through the photoelectric effect, and then the energies of the emitted photoelectrons are detected. The latter energies are characteristic of the original electronic states of the electrons.

Figure 3.5 illustrates a comparative presentation of the density of states for t-Se and a-Se. The band gap of trigonal Selenium is reported to be about 1.85 eV [114, 115, 128], while the band gap for a-Se is not well defined due to the presence of the tail states, and it lies in the range of 2.1..2.3 eV [129, 130]. The peaks below the energy gap in Fig 3.5 correspond to the lone pair states and $4p$ bonding states respectively. The peak after the gap corresponds to the anti-bonding state. It can be seen from Fig. 3.5 that the electronic structure of amorphous Se is similar to that of trigonal Selenium since they both feature a similar spectra for $4p$ *like* bonding, LP and $4p$ *like* anti bonding states.

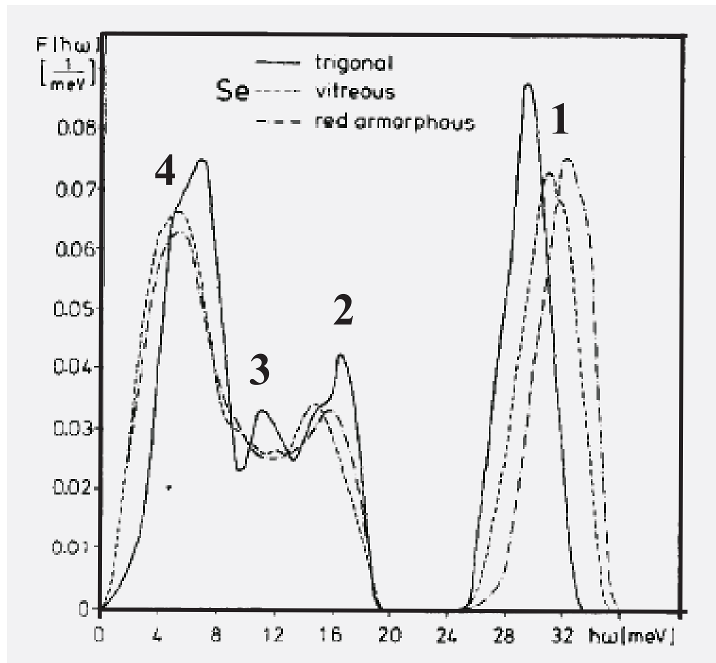

Fig. 3.6: Comparison of the phonon density of states for trigonal Selenium with that of vitreous and amorphous Selenium [131]

3.4 Phonon density of states in crystalline and amorphous Selenium

In phonon collisions, the charge carrier is scattered from one state of energy into another by emitting or absorbing a phonon. According to Eq. 2.16, the rate of this phonon emission depends on the density of phonons. Therefore, to have the calculations of trigonal Se comparable to a-Se, it is required that both amorphous and crystalline phases represent a similar dispersion for phonon density of states.

The PDOS can be directly measured using the coherent inelastic neutron scattering method from Selenium powder [131]. In neutron scattering, the initial and final states of the neutron are described by a wavefunction. The square of the wavefunction's amplitude is the probability that a neutron occupies a particular location. The transferred energy from the inelastic scattering of the neutron will be expended on the stimulation of the vibrational motions. This depends on relative distances between atoms and gives information about the phonons frequencies (See Ch.1 [132]). Figure 3.6 shows the phonon density of states in Selenium [131].

A similar phonon dispersion for both crystalline and disordered Selenium can be seen in

this figure. The first peak in Fig. 3.6, in the range of 24..32 meV, corresponds to the breathing and stretching optical modes. The second peak corresponds to the degenerate optical bending modes, and the third peak is related to the liberation mode. Liberation mode is the lowest energy optical mode. The fourth peak, in the range of 4..10 meV represents the longitudinal and transverse acoustics modes. The detailed analysis of these vibrational modes including their visualizations and calculations of their energies are provided in the next chapter. The optical branch of amorphous Se is shifted by about 3 meV from that of the trigonal Se which is not crucial for the purpose of our study.

These similarities in the density of states and the phonon spectra for both phases of Selenium lead to the fact that Fermi's golden rule (Eq. 2.8,and Eq. 2.9) is applicable to the both ordered and disordered Selenium, and the transport mechanism calculated from one phase is translatable to the other phase. For the sake of conservation of computational efforts, crystalline Selenium was chosen for the case of the presented study. In the next section, density functional theory is introduced as a first principle method for calculation of the corresponding matrix elements in trigonal Selenium.

3.5 Density functional theory

Density functional theory is a theoretical approach to the solution of the Schrodinger's equation in order to describe the quantum behavior of atoms and molecules. Walter Kohn [133] and John Pople won the Nobel prize in chemistry in 1998 for the development of this theory and its practical advantage in computational methods for quantum chemistry. Using DFT theory, the properties of a many-electron system can be determined by employing functional of the electron density. This functional is the exact solution of the Schrodinger equation. Therefore, DFT theory is a first-principle method which allows predictive studies of a wide range of materials. This theory found a broad applications in physics, material science, chemical engineering, geology and other disciplines. According to the *Science Citation Index*, the number of published literatures taking advantage of DFT calculations is about $6,000$ before 1988 and $104,000$ until

2012. This growing rate indicates the popularity of density functional theory as a computational tool among theoretical and experimental scientists.

In order to describe the quantum properties of the material of interest where electrons and nuclei interact with each other, the problem is split into two steps. First, the electron motions are studied for fixed positions of the nuclei in order to find the lowest energy configuration (the ground state energy). In the second step, the vibrations of atoms are then included to take into account the complete electron-phonon interactions [134].

The time independent Schrodinger equation which describes the ground state energy is given by ([134] p. 9)

$$[\ \frac{\hbar^2}{2m}\sum_{i=1}^{N} \dagger_i^2 + \sum_{i=1}^{N} V(\mathbf{r}_i) + \sum_{i=1}^{N}\sum_{j<i} U(\mathbf{r}_i, \mathbf{r}_j)]\psi = E\psi \tag{3.3}$$

where m is the electron mass. The first term in the bracket is the electron's kinetic energy, the second term is the potential energy between each electron and the collection of atomic nuclei, and the last term represents the interaction of electrons with each other. E is the ground state energy of the electrons, and ψ is the Hartree approximation defined as the product of the individual electron wavefunctions $\psi = \psi_1\psi_2, \divideontimes\psi_N$ [135, 136].

In the case of Selenium with 34 electrons, only the analysis of the unit cell which includes 3 atoms in 3 dimensions requires an analysis of a $3 * 3 * 34 = 306$-dimensional full wave function. The latter indicates that highly intensive calculations are needed to solve the Schrodinger equation for a practical material. In addition, the wave function for any particular electron cannot be directly observed ([137] p. 74). Regarding those issues, there is a need for a practical method to reduce the complexity of the calculations.

A quantity of interest which can be experimentally observed is the electrons density ([138] p. 171). This can be given by ([134] p. 10)

$$n(\mathbf{r}) = 2\sum_{i} \psi_i^{\pm}(\mathbf{r})\psi_i(\mathbf{r}) \tag{3.4}$$

where the factor 2 is related to the occupancy of the electronic states, which is a consequence

of the Pauli exclusion principle.

The basis of density functional theory lies in a mathematical theorem by Kohn and Hohenberg. It states that the ground state energy from Schrodinger's equation is a unique functional of the electron density Eq. 3.4. In other words, there is a one-to-one mapping between the ground state wave function and the ground state electron density [139]. Therefore, the ground state energy E can be expressed via a functional of the electron density, $n(\mathbf{r})$ as $E[\psi_i] = E_{KH}[\psi_i] + E_{XC}[\psi_i]$ (See [140] pp.573-592), where the energy functional is split into two contributions. The Kohn-Hohenberg interactions are described as follow ([134] p. 12)

$$E_{KH}[\psi_i] = \frac{\hbar^2}{2m}\sum_{i=1}\int \psi_i^{*}\nabla^2\psi_i d^3\mathbf{r} + \int V(\mathbf{r})n(\mathbf{r})d^3\mathbf{r} + \frac{e^2}{2}\int\int \frac{n(\mathbf{r})n(\mathbf{r}')}{|\mathbf{r}-\mathbf{r}'|}d^3\mathbf{r}d^3\mathbf{r}' + E_{ion} \quad (3.5)$$

where the first term on the right is the electron kinetic energy, the second term is the electron-nuclei Coulomb interactions, the third term is the electron-electron interactions, and the last term is the nuclei-nuclei interaction.

The second part of the ground state energy E_{XC} includes two energy terms, exchange energy and correlation energy. In a non-magnetic material all spins are aligned antiparallel. In order to achieve a parallel orientation of spins, the electrons which undergo a spin flip have to occupy higher lying states according to the Pauli exclusion principle. At the same time, electrons with parallel spin are on average further away from each other, which results in a reduced Coulomb repulsion. This reduced electrostatic Coulomb repulsion between electrons of the same spin with respect to the antiparallel spin alignment is called exchange energy ([141] p.524).

The second energy component in E_{XC} is the correlation energy, which can be explained as a correction to the Hartree-Fock energy. The Hartree-Fock self-consistent-field orbital model theory is the most common approach to study the electronic structure of molecules and crystals ([138] p. 99). However, the instantaneous interaction between electrons (electron correlation) is neglected in this model. The correlation energy is important in accurate calculation of orbitals energies (See Ch.1 [142]). For example, the Hartree-Fock method underestimates atomization energies since it neglects electron correlation, and the correlation energy is larger for molecules than for atoms ([143] p.548). Thus, an improvement to this model is achieved by adding the

correlation energy. The latter can be given by the difference between the exact solution of the non-relativistic Schrodinger equation and the Hartree-Fock energy (Ch. 1 [134]).

The exact form of the exchange-correlation functional does not have a simple analytical form. Instead, several approximations for E_{XC} have been developed to solve the Kohn's equation numerically ([144] p.41).

The XC functional is known for the homogenous electron gas since the electron density is constant for a uniform electron gas. In real materials, the values of the electron density is different at each point in space ([145] Ch. 5.2). In one approximation, the density can be treated locally as an uniform electron gas, and therefore the electron gas XC functional can be extended to real materials [146]. The latter is called the local density approximation (LDA) where the XC potential at each point in the system is the same as that of an uniform electron gas of the same density (Ch. 1 [134] p. 14). This can be formulated as

$$V_{XC}(\mathbf{r}) = V_{XC}^{\text{electrongas}}[n(\mathbf{r})] \tag{3.6}$$

LDA employs the electron gas XC potential for every point in space regardless of the uniformity of the charge density. The XC potential can deviate notably from the uniform result if the material charge density is nonuniform. A correction to the non-uniformity can be provided by expressing this deviation in terms of the gradient of the electron density. The latter is another successful approximation for exchange-correlation energy called the generalized gradient approximation (GGA) [147].

There are various numbers of GGA functionals. Two of the most commonly used functionals are the Perdew-Wang functional [148, 149] and the Perdew-Burke-Ernzerhof functional [150]. There are also more complicated functionals such as the meta-GGA which takes into account the second order gradient of the charge density [151], and the local spin density approximation, which is the extension of LDA to include the electron spins (See Ch.8 [152] for more functionals). Development of the exchange-correlation functionals is an important and active research area.

Different approximations give partially different results for specific configuration of atoms

and molecules. Therefore it is essential to choose the proper functional based on the required properties of interest to get the most accurate results. Each functional has its own pros and cons. For example, LDA overestimates the binding energy, resulting in an underestimated lattice parameters, while GGA is vice versa. A detailed comparison of all available XC functionals with exact results are provided in the Ch. 6 of [153]. Although the band gap energy can not be determined reliably via density fucntional theory, both LDA and GGA interpret the electronic structure well enough [154]. For the sake of the current research on Selenium, both LDA and GGA methods were utilized and the results were compared in chapter 4. Next, the computational algorithm of DFT theory is described.

According to the Hohenberg-Kohn theorem [139], the full solution of the Schrodinger's equation can be achieved using the true electron density. Instead of solving Eq. 3.3 for the coupled wave functions, Kohn and Sham showed that the corresponding electron density can be found through solving a set of equations, where each equation involves a single electron wave function. The Kohn-Sham equations can be derived from [155]

$$\left[-\frac{\hbar^2}{2m}\nabla^2 + V(\mathbf{r}) + e^2\int \frac{n(\mathbf{r}')}{|\mathbf{r}-\mathbf{r}'|}d^3\mathbf{r}' + V_{XC}(\mathbf{r})\right]\psi_i(\mathbf{r}) = e_i\psi_i(\mathbf{r}) \tag{3.7}$$

This equation has a form similar to that of the Eq. 3.3, where the summation is converted to a single electron wave function calculation. The first two terms are the electrons kinetic energy, and the Coulomb interaction between electrons and the nuclei respectively. The third term is the Hartree potential for Coulomb repulsion similar to that of Eq. 3.5, and V_{XC} is the exchange correlation potential.

To solve the Kohn-Sham equation (Eq. 3.7), one needs to define the Hartree potential and to do that the knowledge of the electron density is required. The information of the electron density requires the knowledge of the single electron wave function, and to get this wave function one need to solve the Kohn-Sham equation!

To overcome this circular trend, an initial electron density is defined and an iterative computational method is utilized. First, a trial electron density, $n(\mathbf{r})$, is defined. The Kohn-Sham

equation is then solved using that density to find the single particle wave function, $\psi_i(\mathbf{r})$. The obtained wave function is used to find the electron density, $n_{KS}(\mathbf{r}) = 2\sum_i \psi_i^{\pm}\psi_i$. The last step is to compare the calculated $n_{KS}(\mathbf{r})$ with the initial $n(\mathbf{r})$. The ground state electron density is achieved if these two densities are equal, and the algorithm can proceed toward calculation of the total energy. If the two densities are different, the trial density should be updated and the whole process repeated again until the last step condition is satisfied ([134] Ch. 1).

In this section, density functional theory was introduced as a useful computational tool to evaluate the quantum properties of materials. The Kohn-Hohenberg theorem was introduced where the ground state energy can be expressed via functionals of the electron density. Energy functionals, GGA and LDA, were discussed. Finally the Kohn-Sham single particle wave function theorem and its computational algorithm were explained. The next section explains the methods for DFT calculations including the utilized software techniques.

3.6 Computational ab initio *analysis*

The first principle calculations were performed using the DFT theory implemented in the *ABINIT* package [156, 157], which is a common project of the Universite Catholique de Louvain. *ABINIT* is an open source program that allows the calculation of the electron density, total energy, electronic structure and other specialized properties including the electron phonon matrix elements. The material of interest can be optimized in terms of geometry to find the most accurate lattice parameters. The structure can be then relaxed according to the atomic forces. Pseudo-potentials and planewave methods are utilized together with the optimized structure to enable the analysis of the response function. Response function can determine various physical properties including the phonon vibrations, electron-phonon interaction, dielectric constant and piezoelectricity.

In order to solve the Kohn-Sham equation for a real material, the engaged numerical DFT calculation should be accurate enough and computationally efficient. One successful approach is the plane wave pseudo-potential method where the orbitals are represented via a plane wave

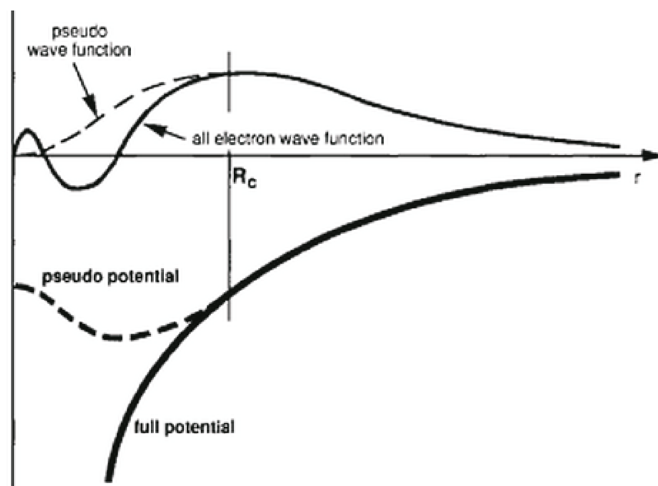

Fig. 3.7: Schematic illustration of the replacement of the all-electron wavefunction and core potential by a pseudo-wavefunction and pseudopotential [159]

basis set, and nuclei and core electrons are treated with the pseudo-potentials ([158] Ch. 3).

The Bloch states experience rapid oscillations close to the crystal nuclei and smoother changes at the outer regions close to the valence electrons. To describe those rapid changes at the core region, plane waves with small wavelengths are required, which enforce a large cut off energy for calculations. This increases the computational time required by the problem. Use of pseudo-potentials can reduce this computational effort. The latter employs a set of pseudo-wavefunctions to solve the Kohn-Sham equation([158] Ch. 3).

The motivation for the pseudo-wavefunctions theory was that the core electrons do not participate in chemical bonding and the valence and conduction properties are mainly due to the electron wavefunctions at the outer orbitals rather than the core electrons. Therefore, the all electron full potential can be replaced by an effective potential so that the core electrons (in case of Selenium $^{18}Ar3d^{10}$) are treated as if they are bound to the nucleus. Hence, the valence electrons (in case of Selenium $4s^24p^4$) are affected by the remaining potential.

In Figure 3.7, a wavefunction in the Coulomb potential of a nucleus, with $V \approx \frac{Z}{r}$, is compared to the one in the corresponding pseudopotential. It is clear that the true potential and the pseudopotential represent the same dispersion after the core cut off radius R_c. Using this method in *ABINIT*, electronic structure of Selenium can be acquired. Details of this calculation

is provided in the next chapter and the results are compared with the experimental data to ascertain their validity. The optimized structure is then used for analysis of the electronic structure and the electron-phonon interaction by means of the response function method.

Density functional theory performs the zero temperature calculation to obtain an atomic structure at the equilibrium. This means that atoms are localized at the minimum energy positions (Ch.5 [134]). It is important to note that in the context of *classical mechanics*, atoms are relaxed at their minimum energy positions at zero temperature, and they start vibrating around these equilibrium positions as the temperature increases. However, in *quantum mechanics*, a system undergo fluctuations even in its ground state at zero temperature. This is the lowest possible energy of the system and it is characterized by the zero-point energy ([160] p.74). The latter atomic vibrations of system can be described in terms of phonon displacements. Phonons energy in Selenium can be measured experimentally via spectroscopy techniques [131]. These phonon vibrations play a major role in electron-phonon scattering. The calculation of the phonon frequencies and electron-phonon matrix elements is done using the response function approach [161, 162]. A quick overview of this method is presented here. The numerical results for Selenium are presented in the next chapter.

The response function is the analysis of the second derivatives of total energy with respect to different perturbations. The response of the total energy to the perturbations including phonons, electric field and strain can determine the physical properties of the materials. For example, phonon dynamical matrix, dielectric tensor, and piezoelectricity are related to the listed perturbations respectively. A simple response function calculation for atomic displacement can be described as follow ([134] Ch. 5). Consider two atoms that are bound together with the bond length b. The total energy of this molecule expanding around the equilibrium bond length, b_0, can be Taylor expanded as ([134] Ch. 5)

$$E = E_0 + (b \quad b_0)\left[\frac{dE}{db}\right]_{b=b_0} + \frac{1}{2}(b \quad b_0)^2\left[\frac{d^2E}{db^2}\right]_{b=b_0} + \times\times\times \tag{3.8}$$

Newton's law gives the force $F = ma$, where $a = d^2b \big/ dt^2$, and force is related to energy via

$F = \quad \partial E/\partial b$. Substituting the given formula in Eq. 3.8, one can obtain

$$\frac{d^2b}{dt^2} = \frac{1}{m}\}\partial E/\partial b + b\frac{\partial^2 E}{\partial b^2} \quad b_0\frac{\partial^2 E}{\partial b^2} + \frac{1}{2}2(b \quad b_0)\frac{\partial^2 E}{\partial b^2} + \frac{1}{2}(b \quad b_0)^2\frac{\partial^3 E}{\partial b^3} + \times\times\times(\tag{3.9}$$

The first term is the first derivative of energy, which is zero at the equilibrium bond length. Ignoring the higher order terms, we can obtain

$$\frac{d^2b}{dt^2} = \frac{2}{m}\frac{\partial^2 E}{\partial b^2}(b \quad b_0) \tag{3.10}$$

The solution of the Eq. 3.10 is $b = b_0 + A\cos\omega t$. A is a constant and ω is the displacement frequency given by

$$\omega = \sqrt{\tfrac{2\alpha}{m}} \tag{3.11}$$

where $\alpha = \frac{d^2E}{db^2}\Big|_{b=b_0}$. It is clear from Eq. 3.11 that the phonon frequency is related to the second derivative of the total energy. Therefore in DFT calculations, the optimized structure first provides the minimum bond length, and then the response function calculates the second derivative of total energy to facilitate the acquiring of the essential pieces of information for further analysis.

In this chapter the density of states and the phonon dispersion were discussed for both crystalline and amorphous Selenium. It was justified that the electron-phonon calculations in t-Se are also applicable to the amorphous structure. Density functional theory was described as a successful computational tool in order to study the electronic properties of materials. Kohn-Hohenberg and Kohn-Sham theories were explained as the basis of the DFT theory. Exchange-correlation energies, GGA and LDA, were discussed. The *ABINIT* package in which the planewave pseudopotential DFT method is implemented was introduced. *ABINIT* takes advantage of the response function approache to analyze the phonon perturbation theory. The next chapter provides the results of the phonon perturbations calculation in t-Se along with the analysis of electronic structure of t-Se and a-Se.

4. RESULTS AND DISCUSSIONS

Chapter one discussed the interest in a-Se and its application in medical imaging. Photoconducting properties of Selenium combined with the feasibility of impact ionization in a-Se make a-Se a promising material for development of high energy radiation photosensors. To understand the high-field charge transport in Selenium, the lucky drift model, was introduced in the second chapter. Further improvement of this model to a self-sustainable theory requires advanced analysis of energy dependent mean free paths. In addition, it has been still remained an open question that what makes a-Se to feature impact ionization among other amorphous materials. The key is to study the electron-phonon interaction and the electronic structure of Selenium. To undertake these problems, density functional theory was introduced in the third chapter as our computational method. Chapter four provides the results of analysis along with their interpretations. This chapter is organized in three sections. Each section is representative of a published paper.

4.1 Interaction of hot carriers with optical phonons in Selenium

4.1.1 Structural model of trigonal Selenium

The structure of t-Se consists of parallel helical chains arranged with a hexagonal symmetry as it can be seen in figure 3.1. The structure can be characterized by two lattice constants a, c and the radius of the chain ρ. Calculations of the electronic structure and electron phonon matrix elements were performed in the framework of density functional theory (DFT) implemented in the *ABINIT* package. Planewave method and Troullier-Martins pseudopotentials were employed. Two approximations for the exchange correlation functional were used: local (LDA) and generalized gradient (GGA) density approximations.

The full structural optimization was performed to get the most accurate structural model of Selenium before proceeding with the electron-phonon interactions. To get the most optimum structure, convergence tests were performed with respect to the planewave cutoff energy E_{cut} and the k-mesh density.

For a periodic structure, the Bloch's theorem gives the electron wavefunction as follow [163]

$$\psi_k(\mathbf{r}) = \sum_{\mathbf{G}} C_{k,G} e^{i(\mathbf{G}+\mathbf{k})\cdot\mathbf{r}} \tag{4.1}$$

where $\mathbf{k}$ is the wavevector and $\mathbf{G}$ is the reciprocal lattice vector. The cutoff energy E_{cut}, which controls the number of planewaves at a given k point can be found from [163]

$$\frac{(\mathbf{G}+\mathbf{k})^2}{2} \sim E_{cut} \tag{4.2}$$

The $\mathbf{k}$-mesh was generated inside the Brillouin zone by means of the Monkhorst-pack method [164]. The Monkhorst-pack grid let us to define a set of $\mathbf{k}$-points in a rectangular grid with dimensions of $M_x * M_y * M_z$ where these points are distributed evenly throughout the space. The higher the number of the grid points is, the finer and more accurate the sampled Brillouin zone will be. On the other hand, the increase in the dimensions of the grid will cost an increase in the computational time. Therefore, the convergence tests are required to find a trade off between the structural accuracy and the computational efforts.

The convergence was reached at $E_{cut} = 25$ Ha and $4 * 4 * 4$ k-point mesh. The calculated values of the lattice parameters are listed in Table 4.1. Results are compared with the experimental values. As it was described in Ch.3, LDA functional overestimates the binding energy, resulting in an underestimated lattice parameter. While LDA calculates the lattice constant a about 10% less than the experimental value, the GGA results show a superior agreement with the experimental data. Only less than 3% deviation from measured values can be seen in GGA calculations. Therefore, GGA approximation was chosen for further calculations of the electronic structure and the matrix elements.

Tab. 4.1: Lattice parameters of t-Se obtained theoretically using DFT with two different approximations (LDA and GGA) for the exchange correlation functional.

	Lattice Parameters (Å)		
	$a = b$	c	ρ
Experimental	4.366[a]	4.953	1.86
	4.277[b]	4.974	
GGA	4.544	5.055	1.88
LDA	3.879	5.080	1.89

[a] Room-temperature data [165]
[b] Results of the measurements are extrapolated to $T = 0$ K [166]

4.1.2 Optical phonon perturbations in Selenium

The phonon-specific matrix element part of the Eq. 2.14 and Eq. 2.16 is given by

$$M_{l,n\propto n\{}(\mathbf{k} \propto \ \mathbf{k} + \mathbf{q}) = \sum_{\tau} \mathbf{u}_l^{\tau}(\mathbf{q}) \times \mathbf{H}_{n\propto n\{}^{\tau}(\mathbf{k} \propto \ \mathbf{k} + \mathbf{q}) \tag{4.3}$$

Where $\mathbf{u}_l^{\tau}(\mathbf{q})$ is the phonon displacement vector of mode l with momentum $\mathbf{q} = \mathbf{k}^{\{} \ \ \mathbf{k}$. The latter determines the amplitude of atomic vibrations for the phonon mode l. The general set of matrix elements $\mathbf{H}$ is dependent on atom τ. These matrix elements were calculated explicitly for nine perturbations caused by the displacement of the three atoms in three directions. Next, the corresponding optical phonon perturbations are discussed.

The unit cell of t-Se consists of three atoms, leading to a total of nine phonon branches: three acoustical and six optical [167, 168]. The corresponding phonon eigenvectors for Selenium were derived by Nakayama [5]. The optical vibrations are illustrated in Fig. 4.1. $A1$ and $A2$ are called breathing and rocking modes respectively. The breathing mode corresponds to the atomic displacements in $x \quad y$ plane. The rocking mode is associated with twisting the chain along the z axis (see Fig 4.1). $E1$ and $E2$ are degenerate modes. The corresponding phonon frequencies are listed in table 4.2. Only four optical modes are listed because of the degeneracy. Modes $A1$ and $E1$ are the highest energy modes corresponding to the first peak of Fig 3.6. Comparison of our calculated phonon energies with the experimental observations are provided in table 4.2.

The calculated frequencies are in agreement with the experimental values, which gives a confidence in our structural model. In the following we focus the attention on modes $E1$ and

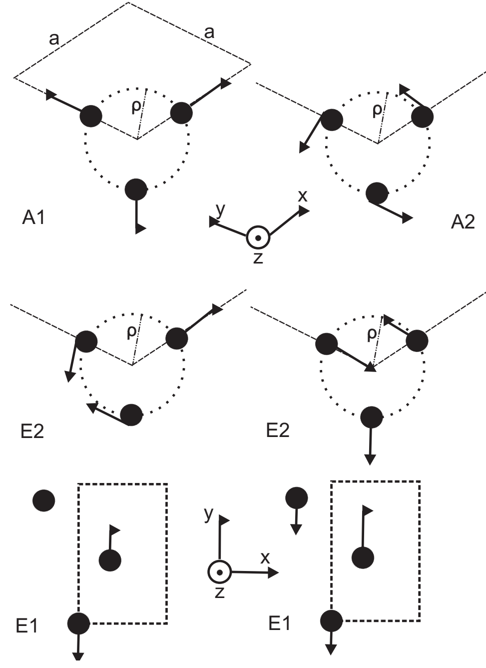

Fig. 4.1: Schematic illustration of the six optical vibration modes of Selenium [5].

$A1$. These two modes are expected to play a major role in the energy relaxation of hot carriers in Selenium, since they both have the highest energy and the highest density of phonon states [131] (See Fig 3.6). Next, we perform the calculations of the electronic structure and matrix elements.

Tab. 4.2: Phonon frequencies at Γ-point of t-Se obtained theoretically, and experimental data.

	Optical Phonon Frequency (cm^{-1})			
	$A1$	$A2$	$E1$	$E2$
Experimental[a]	237	103	233	144
GGA	230	84	218	126

[a] Nakayama [5]

4.1.3 Electronic structure of trigonal Selenium and the electrons and holes matrix elements

To calculate the electronic band structure, the Kohn-Sham equation must be solved for different **k** points along different lines of the Brillouin zone. The Selenium Brillouin zone with a hexagonal symmetry along with the high symmetry points are shown in Fig 4.2a. The corresponding eigenvalues calculated from the Kohn-Sham equation represent the band structure (Fig 4.2b). It is clear from this figure that the conduction bands are separated from the valence bands by

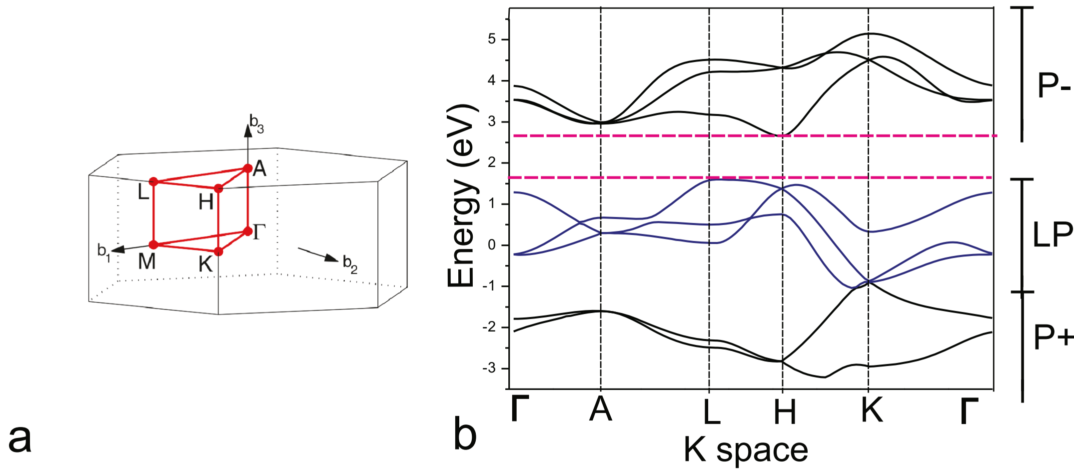

Fig. 4.2: (a) Hexagonal Brillouin zone and (b) electronic band structure of t-Se

a gap of energy. The energy gap determined by the DFT theory is not estimated well and it requires correction. The blue curves represent the lone-pair states which do not contribute in the chemical bonding. The rest of the valence bands correspond to the p-type bonding states. The conduction bands are associated with the antibonding states.

As it is seen in the Fig 4.2b, Selenium is an indirect semiconductor which the valence band maximum is located at L-point while the conduction band minimum is located at H-point. Our band dispersion is consistent with the other structures calculated from a tight binding theory [169, 170]. Also electrons transition measurement in t-Se at symmetry points H, K and Γ validates our electronic structure [171]. Having the information of the bands and the k-vectors, we can now calculate the phonon specific matrix elements of Eq. 4.3.

In our analysis, we limited our study to the relaxation that involves small $\mathbf{q}$ vectors, i.e. the case of $\mathbf{q} = 0$ corresponds to energy relaxation of charge carriers, but not their momentum ($\mathbf{k} = \mathbf{k}^{\{}$). This assumption allows us to eliminate a complex integration in q space. The energy conservation is enforced by considering only diagonal elements, i.e. $M_{l,m\propto m}$.

The matrix elements for $A1$ and $E1$ phonon modes are shown together with the band structure of t-Se in Fig 4.3. The band structure data are shown in 2 eV range of excess energy for electrons and holes, since the minimum excess energy required to ionize the electron-hole pair is about the energy gap [172].

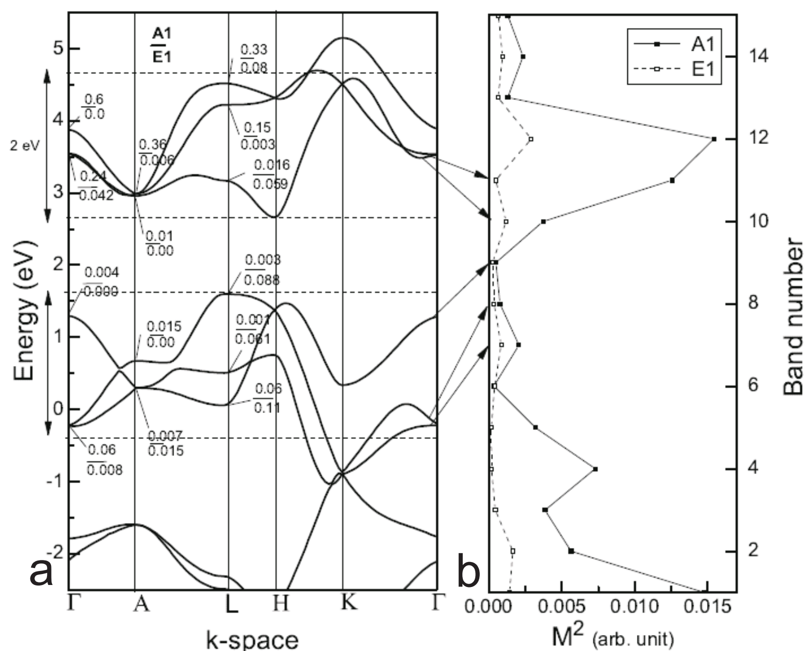

Fig. 4.3: Band structure (a) and the square of the optical phonon matrix element (b) for t-Se. Values in the numerator and denominator on panel (a) correspond to the matrix element squared for A1 and E1 modes, respectively.

Fractional data in Fig. 4.3a shows a general trend for a limited selection of high symmetry **k** points. Values in the numerator and dominator correspond to the matrix element squared for $A1$ and $E1$ modes respectively. It can be seen from Fig. 4.3a that the absolute values of the square of matrix elements in the valence band are by an order of magnitude lower than that in the conduction band. This indicates that electrons show a stronger coupling to the phonon perturbation than holes.

More representative data can be obtained by performing the calculation on a denser mesh of 64 **k** points. Further averaging for each band taking into account the weight of individual **k** points was applied. The corresponding band-average squared matrix elements are shown in Fig. 4.3b. The bands 7 9 in Fig. 4.3b correspond to the top of the valence bands, lone pair states, and the bands 10 12 are the bottom of the conduction band.

An overall stronger electron-phonon coupling can be seen for mode $A1$ than $E1$ in Fig. 4.3b. This is attributed to a break of the lattice symmetry in mode $E1$ which affects the deformation potential screened by electrons ([173] Ch.3.3, [174]). The square matrix elements in the

conduction band is by an order of magnitude greater than that for the top of the valence band. Since the scattering rate is proportional to the corresponding matrix elements via Eq. 2.14 and Eq. 2.16, the energy relaxation time due to the emission/absorption of optical phonons for holes will be longer than that for electrons. In other words, the inelastic scattering rate for electrons will be greater than that for holes. As a result, this intense electron energy loss will suppress the impact ionization of electron. This result correlates with the experimental observation that holes undergo avalanche at lower electric fields than electrons [34].

Excess energy of a charge carrier can be increased by traveling to the energy states further from the band edges in the valence or conduction bands. One can see from Fig. 4.3b that the absolute value of square of the matrix element increases with an increase of the excess energy of holes and electrons. Similar observations were made for an acoustical phonon deformation potential [3]. It was shown that a higher deformation potential can be seen for electrons than for holes, and the deformation potential increases by increasing the excess energy of the charge carriers. These characteristics associated with the both acoustical and optical phonons can be interpreted by means of a tight-binding model.

Atomic states become combined and their corresponding energy states will be shifted when atoms are brought together to form molecules or solids. Hybridization in Selenium splits the atomic p states into bonding and antibonding states, and it leaves an unshared lone-pair states on top of the bonding states (Fig. 3.2). In discussion of solving the time independent Schrodinger equation $H\psi(\mathbf{r}) = E\psi(\mathbf{r})$, the ground state energy which is the minimum energy of the system can be represented by the an eigenstate corresponding to the lowest available energy level. The latter can be found by calculating the average energy, $\frac{\langle\psi|H|\psi\rangle}{\langle\psi|\psi\rangle}$ ([175] Ch.1). Expanding this for the adjacent atoms and minimizing the entire expression to get the lowest energy eigenvalues, one obtains a set of equations which their solution gives the bonding and antibonding states energies as follow [175] p.6

$$E_{\mp} = \frac{H_{11} + H_{22}}{2} \mp \sqrt{\left(\frac{H_{11} - H_{22}}{2}\right)^2 + H_{12}H_{21}} \tag{4.4}$$

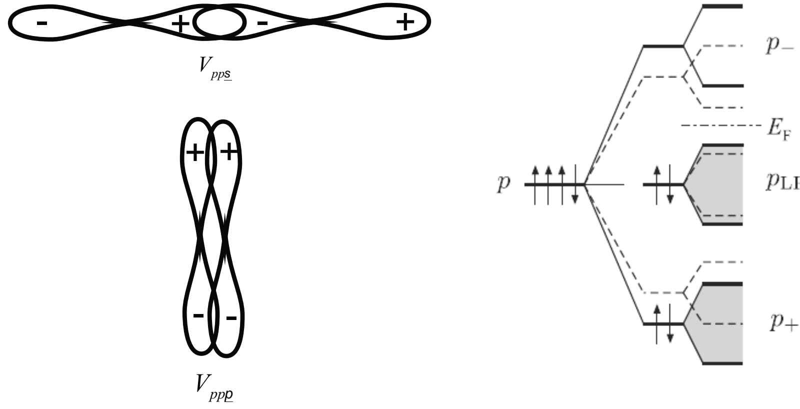

Fig. 4.4: (a) Illustration of $V_{pp\sigma}$ and $V_{pp\pi}$ overlapping orbitals [176] (b) Uniform displacements of atoms will affect the position of the energy bands while the lone-pair states are least affected. Solid and dashed lines correspond to the unstrained and strained lattice respectively [3].

where E_+, and E correspond to the bonding and antibonding states respectively. Here we took advantage of the notation $H_{ij} = \langle \psi_i | H | \psi_j \rangle$, which gives the matrix element of the overlapping orbitals [175] Ch.1. The valence and conduction bands are formed essentially by p states in Selenium. Therefore, splitting of the energy levels depends on orientation of *p* orbitals in Selenium [3]. The corresponding interatomic matrix elements for adjacent atoms in Selenium are $V_{pp\sigma}$ and $V_{pp\pi}$ (Fig. 4.4a). A detailed study of the valence bands formation by Harrison 1975 proved that all the interatomic matrix elements vary approximately as d ^{2} where d is the interatomic spacing [175] p.48. Hence, a phonon perturbation can cause a change in the spacing length and as a result the level of energy splits will change. A schematic explanation of this theory was represented by Rubel *et al* [3]. In this simple illustration (Fig. 4.4b), a uniform atomic expansion/contraction will cause a reduce/increse of both $V_{pp\sigma}$ and $V_{pp\pi}$ that result in a shift of bonding and antibonding bands towards/away one another. It is clear that the lone-pair states are the least affected bands to these phonon perturbations since they are not involved in any chemical bonding. This weak response of upper valence states to lattice perturbations consequence in a lower deformation potential and matrix elements for holes than for electrons in both acoustical and optical perturbations. Our calculated results are in agreement with this model in Fig. 4.4b, which lead to a favorable high-field charge transport in a-Se, where holes undergo avalanche multiplication in a lower electric fields than electrons.

In this section, the electron-phonon matrix elements in trigonal Selenium were calculated for optical phonon modes. These calculations were also compared to previous studies of acoustical modes. The results suggest that energetic holes, as opposed to energetic electrons, should experience a weaker interaction with phonons perturbations. The latter results for holes are attributed to the weak interaction of lone-pair states with atomic displacements. This conclusion for lone-pair states is based on the analysis of t-Se structure. However it was justified that the calculation of phonon interaction in t-Se is translatable to amorphous phase (See chapter 2), there is a question to the efficiency of this assumption.

In the next subsection, an a-Se structure was constructed, and the corresponding pair distribution function was analyzed in order to validate the accuracy of the simulations. This constructed structure was used to study the absolute volume deformation potential in a-Se. The deformation potential was also computed for crystalline Selenium. The aim of the latter was to verify that the response of the electronic structure to phonon perturbations is similar in both trigonal and amorphous Selenium. This is another evidence that justifies the trustworthy of our assumption, in which the electron-optical phonon calculations for t-Se can be also applied to the study of a-Se.

4.1.4 Simulation of the amorphous Selenium structure

Liquid and amorphous Selenium keep definite values of bond angle θ and bond length r similar to those in crystalline state in order to preserve the short range order [177]. The bond angle θ and the bond length r in helical chain crystalline Selenium have fixed values of $\theta = 102 \quad 106^{\leq}$ [15, 178] and $r = 2.3 \quad 2.4$Å [15, 179] respectively. To make a Selenium molecule, consider the following steps: The first atom is located at the origin. The second and third atoms are bonded to the first atom with definite value of θ and r as shown in Fig. 4.5a. These three atoms are found in a plane which makes the dihedral angle ϕ with the plane constituted of atoms 2, 3 and 4. The dihedral angle has a value of $\phi = 100 \quad 103^{\leq}$ in crystalline Selenium [15, 179].

When the fourth atom is linked to the third atom, there are two choices for the dihedral angle,

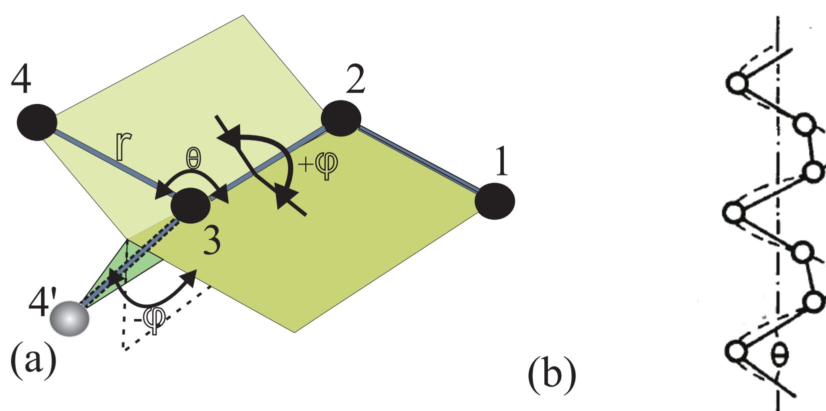

Fig. 4.5: (a) Illustration of dihedral angle cis-conformation $+\phi$ and trans-conformation ϕ in Selenium structure (b) Construction of t-Se crystalline structure with successive trans-conformation dihedral bonding [15].

whether the fourth atom is located at the same side to the first atom ($+\phi$ cis-conformation) or at the opposite side to the first atom (ϕ, trans-conformation). t-Se is formed by successive trans-conformation dihedral bonding (See Fig. 4.5b). On the other hand, a disordered chain model can be constructed when the dihedral angle between atoms in the same chain is random [15]. This random change in the phases of the dihedral angle is on order to avoid any long range order in a-Se structure.

The simulation cell in this work consists of 50 atoms placed in a cubic supercell with periodical boundary conditions (See Fig. 4.6). The creation of a-Se structure involves two steps. First, a preliminary structure of a-Se was created using the self-avoiding random-walk model (the disordered chain model) [15, 180, 178]. In this model, the chains of atoms are built by arranging atoms such that the nearest-neighbor distances and the bond angles correspond to the equilibrium experimental values, while the dihedral angle between atoms in the same chain is random. Second, the structural relaxation was performed using a full-potential linearized augmented plane-wave method implemented in the *WIEN2k* package [181]. *WIEN2k* is a program package that allows to perform electronic structure calculations of solids using density functional theory (DFT). GGA [182] was used for the exchange-correlation functional. The energy to separate core and valence electrons was set to 6 Ry. The product of the atomic sphere radius and plane-wave cutoff in k-space was equal to 7. The Brillouin zone was sampled using a

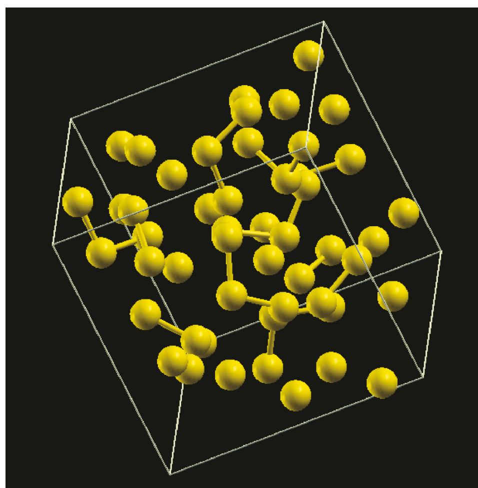

Fig. 4.6: Simulated structure of a-Se including 50 atoms in the cell.

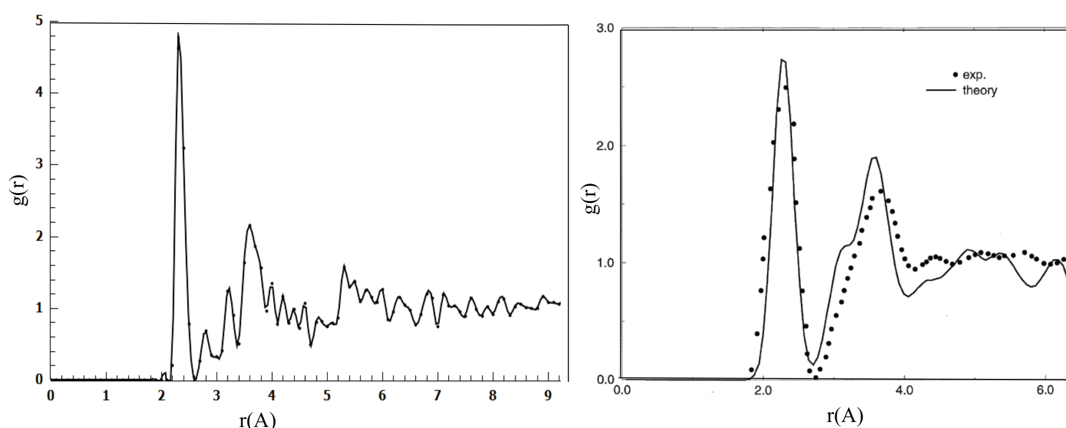

Fig. 4.7: Calculated pair distribution function for amorphous Selenium (left panel), and its comparison with one obtained from molecular dynamics simulation and experiments (right panel [183]).

$2 * 2 * 2$ Monkhorst-Pack mesh [164]. The internal degrees of freedom were relaxed by minimizing the total energy and forces acting on atoms. In the final structure, the residual forces did not exceed 2 mRy/Bohr. Next, the validity of our simulated structure was confirmed by analysis of the pair distribution function.

The radial distribution function $g(r)$ was calculated in order to verify the simulated structure. $g(r)$ is given by Eq. 4.5, where $n(r)$ is the mean number of atoms in a shell of width dr at distance r, and ρ is the mean atom density. This function is calculated for every atom in the structure, and then averaged out over all atoms in the system.

$$g(r) = n(r) \big/ \rho 4\pi r^2 dr \tag{4.5}$$

Fig. 4.7 shows the calculated pair correlation function for a-Se. Two prominent peaks can be seen at 2.3 Å and 3.65 Å which corresponds to the first and second nearest neighbor in a-Se. The latter is sign of the short range order in the structure. Our results are in good agreement with theoretical and experiential investigations (See Fig. 4.7 right panel) [183, 16, 104]. The atomic correlation is lost at further distances ($r > 4$ Å) due to the lack of long range order.

4.1.5 Volume deformation potential in amorphous Selenium

In the discussion of the electron-phonon interaction, the response of t-Se electronic structure to optical vibrations were studied in previous subsection. However the results from t-Se are applicable to a-Se, one further step is to analyze the electron-phonon interaction in actual a-Se structure. The present subsection aims not to repeat the calculations of optical phonons, but instead to study an acoustical mode in amorphous Selenium. It is shown that the results of a-Se is in agreement with that of t-Se. This confirms the validity of our assumption discussed in the second chapter.

Scattering of electrons with low excess energy occurs predominantly with small wavenumber phonons (acoustics phonons) ([100] p.391). Scattering with optical phonons occurs less often due to the higher required excess energy of carrier for this interaction. The electrons interaction with acoustic phonons can ordinarily be described in terms of a volume deformation potential. A small uniform expansion of the lattice by δV will shift the energy of electronic bands E_{nk} by an amount of ([101] p.125)

$$\delta E_{nk} = \Xi_{nk}(\frac{\delta V}{V}) \tag{4.6}$$

where Ξ_{nk} is the volume deformation potential. Scattering of electrons with phonons is derived from the Fermi's golden rule (Eq. 2.8), where $\left|M_{if}\right|^2$ is the squared of the electron-phonon interaction matrix elements. The corresponding matrix elements for transition of electrons from state $\sqrt{i|}$ with momentum k to a final state $\sqrt{f|}$ with momentum $k^{\prime} = k + q$ can be described in

terms of deformation potential ([100] p. 415)

$$\left|M_{kq}\right|^2 = \frac{n_q \hbar q^2}{2\rho V} \frac{\Xi_k{}^2}{N\omega} \tag{4.7}$$

where n_q is the phonon Bose-Einstein distribution in Eq. 2.15, $\hbar\omega$ is the phonon energy, N is the number of atoms in the lattice, ρ is the density and V represents the volume. It is clear form Eq. 4.7 that the scattering rate between two states for the electron will be proportional the square of the deformation potential. Hence, the volume deformation potential for a-Se and t-Se was calculated in this subsection.

The absolute deformation potential can be evaluated from Eq. 4.6 by calculating the relative change in the eigenvalues E_{nk} of the strained and unstrained electronic structure of Selenium. The energy levels of $1s$ core states were averaged out for 50 atoms and it was taken as a reference energy assuming that these core states are not sensitive to the volume deformation [184].

The results of calculation for a-Se and t-Se are shown Fig. 4.8 as a function of the excess energy of a charge carrier. The excess energy is in the range of upper valence band and bottom of the conduction band widths (see Fig.4.3a). An overall higher deformation potential can be seen for electrons than for holes in both trigonal and amorphous Selenium. This implies that the lone-pair states are least affected by the atomic vibrations. This low response of lone-pair states to phonon modes can be interpreted via a tight bonding model discussed in the subsection 4.1.3. The latter is in agreement with calculated electron-optical phonon matrix elements (see Fig.4.3b). This confirms the validity of our assumption discussed in Ch. 2.

Results for t-Se are also in correlation with previous studies of longitudinal acoustical deformation potential [3]. A parabolic dependence of deformation potential on the excess energy can be seen for both electrons and holes in t-Se [3].

Comparing two electronic structures in Fig. 4.8, a relatively higher deformation potential for electrons can be seen in a-Se than in t-Se. The latter resulting in a higher elastic scattering of electrons in a-Se is due to the disorder in amorphous structure.

In order to connect this discussion to the lucky drift model, the energy dependence of the volume deformation potential and the electron-optical phonon matrix elements on the mean

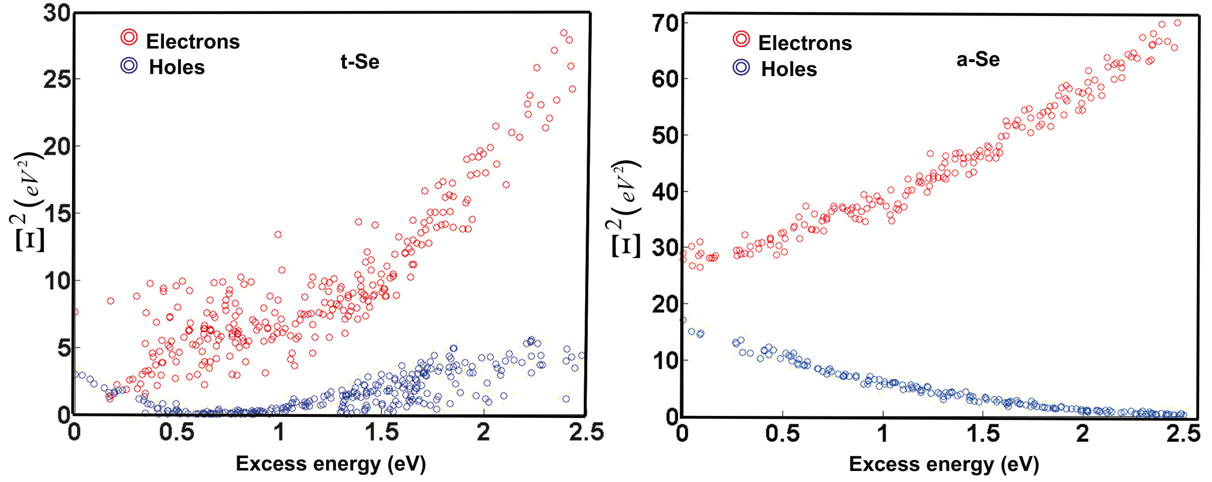

Fig. 4.8: Dependence of the squared of volume deformation potential on the excess energy for electrons and holes in t-Se (left panel) and a-Se (right panel).

free paths are considered. The mean free paths are inversely proportional to the scattering rates, and the inelastic and elastic scattering rates are proportional to the M^2 via Eq. 2.8 and Eq. 4.7 respectively. Therefore, it can be concluded from Fig. 4.8 that the momentum relaxing mean free path for holes increases with an increase in their excess energy. An opposite dependence is seen for electrons. This increase in the holes mean free path favours the avalanche multiplication of holes in a lower electric field than electrons.

Further analysis can be obtained from Kasap *et al* study to extend the lucky drift impact ionization model to a-Se [85]. It was attempted to describe the impact ionization coefficient α as a function of reciprocal field $1/F$ for holes and electrons in a-Se. The application of lucky drift model with energy *independent* mean free path led to a quite small ionization threshold energy in a-Se ($E_i \ll E_g/3$) [97]. The best fit to the experimental data was obtained by assuming an energy *dependent* mean free path in a form of [85]

$$\lambda_E = \lambda_{E_0} + AE^s \tag{4.8}$$

where λ_{E_0} is the constant low energy value of λ_E, s is some characteristics scattering index, and B is a constant that is a measure of the dependence of λ_E on energy E. An excellent fit to the experimental data can be obtained with selection of $s = 1$, $\lambda_{E_0} = 0.377$ nm and $A = 2.92$ nm

$(eV)^{1}$. In nearly all combination cases of these parameters, one obtains $\lambda_E \ll 4 \quad 6$ nm. This is successful in interpreting observed data taking into account that the mean free path increases with the carrier excess energy (See Eq. 4.8). The latter is consistent with our calculation of deformation potential in a-Se, where our interpretation suggests that mean free path for holes increases by an increase in their excess energies .

In this subsection, an a-Se structure was constructed and the volume deformation potential was studied for the simulated amorphous phase. We showed that the lone-pair states response is in conjunction with that of t-Se results presented in the latter subsection.

The interesting dispersion of Selenium electronic states, which was calculated in this section, combined with the feasibility of avalanche multiplication in a-Se provides a basis to propose a new perspective in semiconductor research. In the next section, development of functional materials that feature single carrier multiplication is suggested via analysis of the Selenium band dispersion. In single carrier multiplication only one type of electric charges, either electron or hole, participate in impact ionization. The latter has practical advantage in application of low noise avalanche photodiodes.

4.2 Single carrier impact ionization favored by a limited band dispersion

4.2.1 Confinement of the carriers excess energy by a limited width of the energy bands

Impact ionization in semiconductors and subsequent avalanche multiplication of charge carriers is widely exploited in avalanche photodiodes (APDs) (See Ch.1). Chapter one explored a quick look at the wide range of applications of this phenomenon in high-sensitivity photoreceptors. APDs generally operate in a linear mode at a bias voltage lower than the breakdown voltage, where the output current is linearly proportional to the incident photon flux[185]. The requirements to semiconducting materials for linear APDs include high gain and low excess noise. Variations in avalanche gains result in an excess noise in the detector. The corresponding

excess noise factor in an electron-avalanche based detector can be given by

$$F = kM + \left(2 \quad \frac{1}{M}\right)(1 \quad k) \tag{4.9}$$

where k is the ratio of the hole impact ionization rate to that of electrons (so-called k-factor), and M is the avalanche gain. One can see from Eq. 4.9 that in case of avalanche multiplication of both carriers, $k = 1$, a huge excess noise appears at the terminal ($F = M$). This factor can be decreased to its minimum ($F < 2$) if only electrons take part in impact ionization process ($k \ll 0$). Hence, in order to fulfill the requirements of high gain and low noise, semiconductors that feature a single-carrier multiplication are needed.

Unfortunately, k-factor is far from its ideal value for the majority of technologically-relevant semiconductors, such as Si [186], GaAs (Ref. [187], p. 320) , InP [188]. In the following, we show that the single-carrier avalanche multiplication can be achieved as a result of a limited dispersion for one of the carriers and/or fundamental restrictions, such as energy and momentum conservation. This opens an avenue for the design of materials with the electronic structure that favors single-carrier avalanche multiplication.

The hypothetical electronic band structure of a material with high k-factor is shown on Fig. 4.9. Its characteristic feature is a limited width of the conduction band, which prevents free electrons from gaining the excess energy enough to initiate the impact ionization. The presence of a gap of energy in conduction band confines the energy range of hot electrons. In contrast to free electrons, the valence band dispersion permits the impact ionization initiated by holes. A schematic illustration of hole impact ionization is displayed in Fig. 4.9. Successful ionization event is caused by the primary hole 1 and results in creation of the electron-hole pair 2 and 2'. A material that feature such an electronic dispersion will exhibit full suppression of the counterpart carrier multiplication. In order to illustrate feasibility of the proposed concept, the electronic structure of trigonal Selenium (t-Se) in the framework of a DFT theory was analyzed. It is shown that the presence of an energy gap in the conduction band limits the electron participation in the impact ionization, while the extended dispersion of lone-pair states in the valence band favors the hole impact ionization.

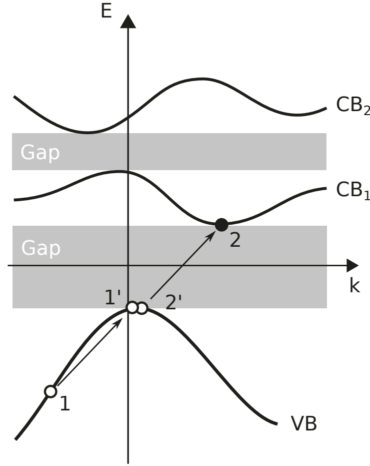

Fig. 4.9: Hypothetical band structure of a material with frustrated avalanche multiplication of electrons.

4.2.2 Principle conservation rules in impact ionization

A necessary condition for the impact ionization to occur is that all initiating and resultant particles should satisfy the energy and momentum conservation requirements.

$$E(\mathbf{k}_1, n_1) + E(\mathbf{k}_2, n_2) = E(\mathbf{k}_{1'}, n_{1'}) + E(\mathbf{k}_{2'}, n_{2'}) \,, \tag{4.10}$$

$$\mathbf{k}_1 + \mathbf{k}_2 = \mathbf{k}_{1'} + \mathbf{k}_{2'} \,, \tag{4.11}$$

where k_i is the electron wave vector, n_i is the band index and $E(\mathbf{k}_i, n_i)$ is the corresponding energy eigenvalue. The indices 1, 2 and 1', 2' represent the initiating and resultant carriers, respectively. The ionization energy corresponds to the excess energy of the primary carrier 1.

Further analysis of the ionization threshold for electrons and holes in t-Se requires detailed knowledge of the band structure, which was obtained self-consistently using DFT in the former section. Selenium electronic dispersion along high-symmetry points in the Brillouin zone is shown in figure 4.10. Bonding σ, antibonding $\sigma^{\pm}$ and lone-pair (LP) states are indicated. The calculated band gap was corrected to the experimental value of $E_g = 1.85$ eV by means of a so called scissor operator. The shaded areas in fig 4.10correspond to the optical gap and the gap between two conduction bands (from bottom to top, respectively). One can see that the valence band benefits from a continues dispersion while the conduction band, the blue curves,

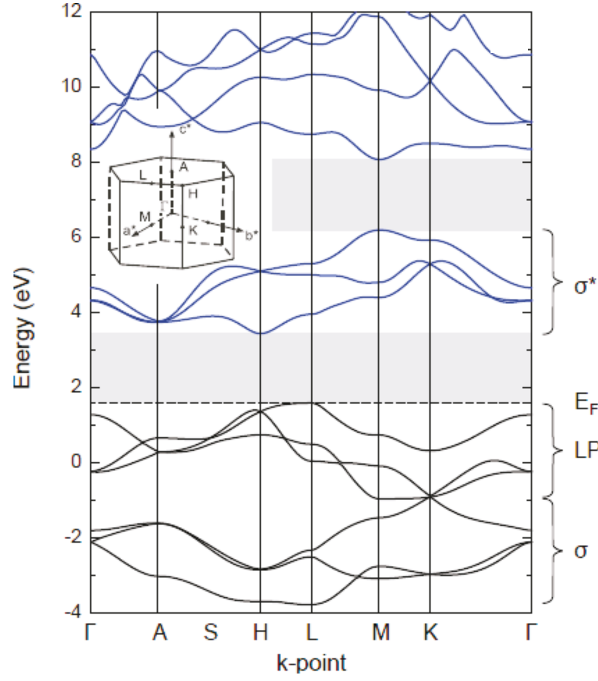

Fig. 4.10: Electronic band structure of t-Se, Shaded areas correspond to the optical gap and the gap between two conduction bands (from bottom to top, respectively

is split by a gap of energy. This gap in the conduction band is about 2 eV. The necessary precursor for impact ionization is a low threshold energy of a primary charge carrier. The entire Brillouin zone of Selenium was sampled using 6,400 k-points ($20 * 20 * 16$ mesh) in order to find the ionization threshold. The threshold energy is identified as the lowest possible ionization energy that satisfies the conservation rules. Next we analyzed all possible ionization events by generating combinations of four k-points that obey Eq. 4.11. For each set of k-points and the combination of four bands (n_1, n_2, n'_1, n'_2) involved in the impact ionization event, the energy conservation criterion Eq. 4.10 was evaluated using a Gaussian approximation for the delta function with the smearing of 50 meV. This approach provides the resolution of approximately 20 meV for the ionization energy, which is sufficient for the purpose of our discussion.

The analysis of the electronic structure of t-Se yields the ionization threshold of 1.85 eV for electrons as primary charge carriers. The charge carriers with the lowest ionization energy are located along H L H segment of the Brillouin zone. Fig. 4.11 shows the band structure along H L H segment with four particles involved into the electron ionization event near to the threshold. The resultant carriers 1’, 2 and 2’ occupy states in the valence band maxi-

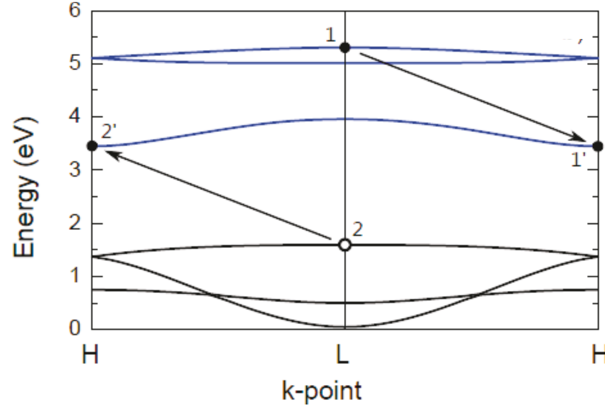

Fig. 4.11: The electronic band structure of t-Se along H-L-H segment.

mum (L-point) and the conduction band minimum (H-point), which ensures the lowest possible ionization energy $E_{th,e} = E_g$, providing a sharp contrast with the parabolic band approximation [189], which predicts $E_{th} = 1.5E_g$.

Results of our calculations suggest that the ionization energy for primary holes amounts to 1.95 eV ($E_{th,h} = 1.05E_g$), which is slightly greater than that for electrons. The interpretation of this result requires further analysis of the valence band dispersion. For the energy threshold to be equal to the band gap, the resultant carriers 1', 2 and 2' should not have any excess energy, i.e., occupy the valence band maximum and the conduction band minimum (L and H points, respectively). In this case, the momentum conservation dictates that the wave vector of the primary carrier k_1 should be either at H or S point (see Fig. 4.12). Apparently, the excess energy of holes in H and S points of the lone pair band does not exceed the band gap (see Fig. 4.10), which precludes their participation in the impact ionization. Therefore, the wave vectors of particles participating in the impact ionization of holes near to the threshold deviate from these high symmetry points as shown in Fig. 4.12, resulting in the value of ionization energy slightly higher than E_g, but still lower than $1.5E_g$.

4.2.3 Effective density of states for impact ionization

The low ratio $E_{th}/E_g \ll 1$ is a consequence of an indirect band structure inherent to t-Se, which is a positive factor for the avalanche gain. However, the insufficient disparity between the values

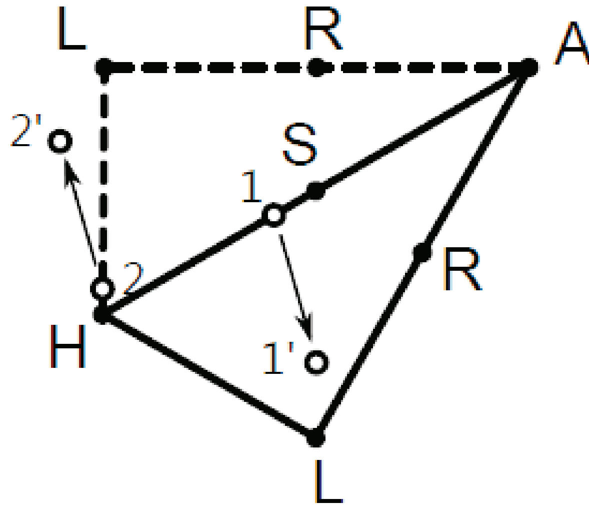

Fig. 4.12: Top view of the Brillouin zone with k-points involved into the hole ionization event near to the threshold.

of $E_{th,e}$ and $E_{th,h}$ can affect the feasibility of operation in the single-carrier multiplication mode. It has been indeed observed experimentally [190] that the avalanche multiplication in polycrystalline t-Se is dominated by holes with the ratio $\beta/\alpha \rightarrow 10$. This result implies that factors other than the ionization threshold are responsible for the nearly single-carrier multiplication in t-Se.

The impact ionization rate for a carrier with the energy equal to or above the ionization threshold is proportional to the value of a corresponding Auger matrix element and an effective density of states. In the following, we focus our discussion on the energy dependence of the effective density of states (DOS), assuming that the matrix element does not vary significantly near to the threshold energy [191]. The effective DOS for four-particles inverse Auger process represents the relative number of possible ionization events as a function of excess energy of the primary carrier.

The relative number of possible ionization events that satisfy the conservation rules is plotted on Fig. 4.13 as a function of the excess energy of the primary carrier. Apparently, the effective DOS for primary holes increases faster than that for electrons as the excess energy exceeds the threshold. Furthermore, the DOS for primary electrons exists only in the narrow range of excess energies 1.85 2.65 eV, which is related to a limited width of $\sigma^{\pm}$ antibonding states in t-Se. The effective DOS for holes shows no discontinuity at higher excess energies due to the absence of

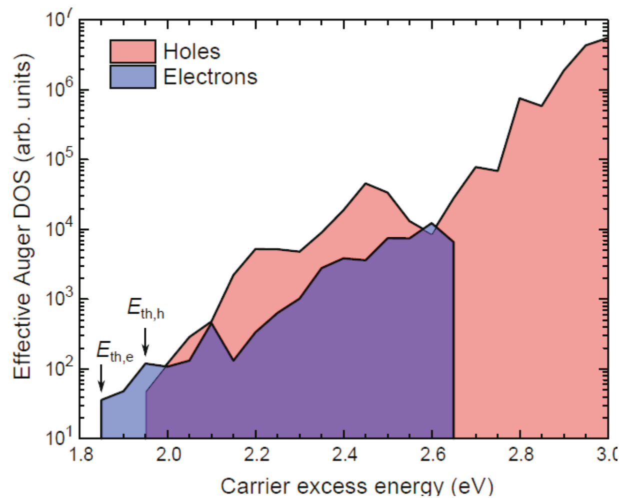

Fig. 4.13: Effective density of states for impact ionization as a function of the excess energy of primary electrons and holes

the energy gap between lone-pair and bonding σ states as can be seen at Fig. 4.10.

The results of our calculations suggest that the suppression of electrons' avalanche multiplication in t-Se can be caused by peculiarities of its electronic structure. In conjunction with the week electron-phonon coupling inherent to holes in t-Se [192, 3], these properties favor the single-carrier impact ionization.

According to calculations of the electronic structure of a-Se [193], it also features a gap in the conduction band analogous to that in t-Se, which can be a possible explanation for the observed high disparity between impact ionization coefficients for electrons and holes in a-Se. The K-factor for amorphous selenium ranges between 10 and 100 depending on the electric field strength [86]. However, the field corresponding to the onset of avalanche multiplication in a-Se is about 70 V/μm [33], which is significantly higher than that in the polycrystalline form (15 . . . 20 V/μm [190]). This difference is attributed to intense elastic scattering due to disorder inherent to the amorphous structure [87, 85].

Another prominent class of materials that demonstrated a well-separated narrow conduction band similar to Fig. 4.9 are quaternary chalcogenide I_2-II-IV-VI_4 semiconductors [194, 195, 196]. Specific examples include Cu_2ZnGeS_4 and $Cu_2ZnSnSe_4$ compounds, which are currently studied as an active material for thin-film solar cells [197]. In these structures, the lowest conduction band has the width of 1 2 eV, and it is separated by the energy gap of approximately

the same magnitude from the rest of the conduction band [194, 195, 196]. The topmost valence band, on the other hand, is much wider than the optical energy gap. Bearing in mind that the optical energy gap in these materials is of the order of 1.5 eV, this material class show a great promise for single-carrier (holes) avalanche multiplication, because the electron multiplication should be fully suppressed.

In previous section, calculation of the electron-phonon matrix elements and the weak response of the lone-pair states to phonon perturbation suggested a favorable high-field charge transport for holes. In this section, we moved one step further by analyzing the density of states for impact ionization in Selenium. Also, the ionization threshold energies for electrons and holes in t-Se were computed based on its electronic structure. It was shown that the single-carrier multiplication regime, which is a requirement for the development of linear APDs with high gain and low noise, can be achieved by confinement of the kinetic energy for the counterpart charge carrier. In other word, the good combination of valence band continues dispersion with presence of the lone-pair states favors the impact ionization of holes in Selenium. However, the limited band width of the conduction band along with the intense inelastic scattering rate with optical phonons suppress the electrons impact ionization. Similar peculiarities of the electronic band structure are found in compound chalcogenide I_2-II-IV-VI_4 semiconductors that makes them a promising candidate for the active material in high-sensitivity photoreceptors.

Moreover, Our results suggest that the excess energy of the primary carrier required to generate the secondary electron-hole pair in t-Se is approximately equal to the energy gap ($E_{\mathrm{th,e/h}} \ll E_{\mathrm{g}}$) that is significantly different from the result predicted by the parabolic band approximation ($E_{\mathrm{th,e/h}} = 1.5E_{\mathrm{g}}$).

Results from analysis of the ionization threshold energy lead to an advanced study of pair creation energy for a-Se in the next section. In the following, calculation of pair creation energy in Selenium based on its electronic structure is presented. The latter factor plays a major role in development of Selenium-based direct conversion photodetectors for high-energy radiation applications.

4.3 Modeling the radiation ionization energy and energy resolution of trigonal Selenium and amorphous Selenium from first principles

4.3.1 Pair creation energy

Semiconductors are widely used as functional materials in high-energy radiation detectors. The direct conversion based detectors including Se and (CdZn)Te detectors attracted a vast attentions in medical and industrial imaging, dosimetry and security [198, 199, 200]. Amorphous Selenium-based flat-panel x-ray detectors and their principles were reviewed in the first chapter. The sensitivity of these detectors is determined by their ability to convert high-energy photons into electron-hole pairs. The corresponding characteristic of the material is the pair-creation energy, $W^0_\mp$, which is the ratio between the radiation-ionization energy and the average number of electron-hole pairs created (quantum yield). $W^0_\mp$ is empirically about 3 times the band gap energy E_g of the semiconductor.

The theory of electron-hole pair production by impact ionization in semiconductors was initially introduced by Shockly [84] and further refined by Klein [201] in the context of electron-hole pair generation by ionizing radiation. According to Klein [201], $W^0_\mp$ is related to the semiconductor energy gap E_g, the average residual kinetic energy of resultant carriers $\rangle E_k|$, and the average energy loss to optical phonons $\rangle E_{ph}|$ between two ionization events in the following way

$$W^0_\mp = E_g + 2\rangle E_k| + \rangle E_{ph}| \ . \tag{4.12}$$

It is assumed that the energy of the ionizing radiation is spent on creation of excited electrons and holes. When one of these particles reaches a final states where it can no longer excite another e-h pair due to its low energy below the ionization energy E_{th}, it thermalizes by phonon emission. Each available state is assumed equally likely to be a final state, and the density of states $\rho(E)$ is then $\rho(E) \propto \sqrt{E}$. Considering energy and momentum conservation requirements during the pair production event [202], and assuming a parabolic band dispersion along with the random-**k** approximation [203], the following expression is obtained for the average of the

residual kinetic energy [201]

$$\rangle E_k| = \frac{\int_0^{E_{th}} E\rho(E)dE}{\int_0^{E_{th}} \rho(E)dE} = \frac{\int_0^{E_{th}} E^{3/2}dE}{\int_0^{E_{th}} E^{1/2}dE} = \frac{3}{5}E_{th} , \tag{4.13}$$

One can obtain $W^0_\mp$ by submitting Eq. 4.13 in Eq. 4.12 using the parabolic band assumption for the ionization threshold energy $E_{th} = 3/2E_g$

$$W^0_\mp = E_g + 2\frac{3}{5}E_{th} + \rangle E_{ph}| = E_g + \frac{9}{5}E_g + \rangle E_{ph}| \ , \tag{4.14}$$

$$W^0_\mp \ll 2.8E_g + \rangle E_{ph}| \ \ , \tag{4.15}$$

The average phonon energy loss is usually assumed to be in the range of $\rangle E_{ph}| = 0.5 \ldots 1$ eV for the majority of semiconductors [84].

In spite of the number of approximations involved, Eq. (4.15) provides a good representation of the experimentally observed linear dependence of $W^0_\mp$ on the energy gap in most semiconductors [201]. The notable exception is amorphous Selenium, for which Eq. (4.15) overestimates the pair-creation energy by approximately 2 eV [204]. In particular, the mobility gap of a-Se is about 2.3 eV [205], which, through Eq. (4.15), leads to the theoretical $W^0_\mp \ll 7.0 \ldots 7.5$ eV. However, the experimental intrinsic value of $W^0_\mp$ in a-Se is approximately $4 \ldots 6$ eV [206].

Que and Rowlands [204] proposed to resolve this inconsistency in a-Se by assuming that the ionization threshold energy, E_{th}, is equal to the energy gap. This assumption implies loosening the requirement of momentum conservation, which is motivated by the disordered structure of a-Se. Accordingly, Eq. (4.15) is transformed into [204, 84]

$$W^0_\mp \ll E_g + 2\frac{3}{5}E_g + \rangle E_{ph}| , \tag{4.16}$$

$$W^0_\mp \ll 2.2E_g + \rangle E_{ph}| , \tag{4.17}$$

The latter expression is consistent with the experimental data for the pair production energy in

a-Se.

Our analysis of the electronic structure of trigonal Selenium in previous section indicates that $E_{th} \ll E_g$ for both types of charge carriers as a result of the indirect band structure [207]. Therefore, the assumption regarding violation of momentum conservation is not necessarily required for interpretation of the low $W^0_{\mp}$ in a-Se.

In this section, a detailed calculations of the electron-hole pair creation energy in t-Se and a-Se from first principles is reported. Unlike previous calculations [204], which were based on the parabolic band structure approximation, our calculations include realistic density of states and ionization threshold energies that result in more accurate and reliable prediction of the pair creation energy. Furthermore, we report theoretical values of the Fano factor, a measure of the dispersion of the probability distribution of $W^0_{\mp}$. The calculated intrinsic Fano factor turns out to be lower than that in (CdZn)Te indicating a high potential for a good energy resolution in a-Se. In the discussion we specially emphasize the statistical role of recombination as a limiting factor of the energy resolution.

The generation of charge carriers by ionizing radiation is generally viewed as a two-step process. The first step involves the absorption of a high-energy photon and the subsequent creation of primary energetic electrons and holes. In the second step, the primary charge carriers lose their kinetic energy mainly by impact ionization leading to the production of secondary electron-hole pairs. The process continues until the excess kinetic energy of the secondary carriers falls below the ionization threshold. The main challenge in theoretical calculation of the pair production energy using Eq. (4.12) is finding an accurate approximation for the average kinetic energy of residual charge carriers while taking into account the electronic structure of the material in question.

Here we use a random-**k** approximation [203, 208], which is proven to be successful especially for transitions far from the ionization threshold. This approximation implies a uniform distribution of final carriers in **k**-space, which translates into the probability for a resultant carrier of falling in the energy interval $(E, E + dE)$ to be proportional to the density of states $\rho(E)$.

The average kinetic energy of residual electrons can then be expressed as [202]

$$\rangle E_{k,e} | = \frac{\int_{E_{\mathrm{CBM}}}^{E_{\mathrm{th,e}}} (E \quad E_{\mathrm{CBM}})\, \rho(E)\, \mathrm{d}E}{\int_{E_{\mathrm{CBM}}}^{E_{\mathrm{th,e}}} \rho(E)\, \mathrm{d}E}, \tag{4.18}$$

where $E_{\mathrm{th,e}}$ is the ionization threshold energy for electrons and E_{CBM} is the energy position of the conduction band minimum. It is straightforward to extend Eq. (4.18) for holes to get a similar equation.

We begin the calculation of the average pair creation energy $W^0_{\mp}$ by identifying the values of its main constituents: the semiconductor energy gap E_g, the average residual kinetic energy of resultant carriers $\rangle E_k |$ and the average energy loss to optical phonons $\rangle E_{ph} |$.

The energy gap of t-Se is 1.85 eV [114, 115, 128]. In amorphous structures, E_{g} is not well defined due to the extended band tails. Therefore, we use a range of 1.95 . . . 2.3 eV for a-Se. The lower bound corresponds to optical absorption measurements [209, 210], whereas the upper limit is set by transport measurements of the mobility gap [205, 129, 130].

Calculation of the average kinetic energy for residual carriers requires knowledge of the DOS near the top of the valence band and the bottom of the conduction band, as well as the ionization threshold. Calculation of DOS for trigonal Selenium was undertaken in the framework of the density functional theory implemented in the `ABINIT` package [211, 157]. The DFT theory and the `ABINIT` package were discussed in previous chapter. The generalized gradient approximation (GGA) [182] and Troullier-Martins pseudopotentials [212, 213] were employed. The valence electron wave functions were expanded using a plane wave basis set with the cut-off energy of 25 Ha. The Brillouin zone was sampled using a Monkhorst-Pack [164] $20 * 20 * 18$ **k**-point mesh. Further details regarding the geometry of the model structure and convergence criteria have been discussed in previous chapter.

Calculation of DOS for a-Se was undertaken using `WIEN2K` package. Simulation of a-Se structure in the framework of a density functional theory and a random-walk model was provided in previous section.

The DFT energy gap of t-Se is about 1 eV, which is significantly underestimated with respect to the experimental value of 1.85 eV [114, 115, 128]. This inconsistency is attributed to a well-known shortcoming of explicit density-dependent functionals, which tend to underestimate the energy gap [154]. In the following analysis, the so-called "scissor operator" (energy offset) was applied in order to match the theoretical energy gap with its experimental value. The same energy offset was also applied when calculating DOS for a-Se.

The calculated DOS of t-Se and a-Se are presented in Fig. 4.14. Both densities of states clearly exhibit the presence of bonding, antibonding and lone-pair states.The width of the corresponding bands is about 2.5 . . . 3 eV, which is consistent with previous calculations [124, 125] and experimental measurements [123, 4]. The lone-pair DOS of t-Se has a characteristic double-peak structure [124, 125], which is well reproduced in our calculations. In the case of a-Se, peaks and the band edges are smeared due to the disorder [4]. Nevertheless, it is still possible to resolve a gap between bonding and antibonding DOS, the presence of which is a signature of a distorted, but not random dihedral angle [125, 14]. Some sharp features are still present in a-Se DOS (Fig. 4.14) and can be related to the finite size of the simulation volume. However, the latter does not affect the calculation of $W_{\mp}$ due to the averaging procedure in Eq. (**??**).

The top of the valence band and bottom of the conduction band of t-Se DOS are marked as E_{VBM} and E_{CBM}, respectively in Fig. 4.14. The shaded area indicates the states, which can be occupied by residual charge carriers with excess energy not exceeding the ionization threshold energy for electrons and holes ($E_{\mathrm{th,e}}$ and $E_{\mathrm{th,h}}$, respectively. The center of mass of the shaded area corresponds to the average kinetic energy $\rangle E_{\mathrm{k}}|$ of residual carriers. The difference between these energies is the pair creation energy minus the phonon contribution, $W^{0}_{\mp}$ $\rangle E_{\mathrm{ph}}|$. The calculated DOS for a-Se is shown in Fig. 4.14 for comparison (red dashed line). The Gaussian broadening of 25 meV was applied in both cases.

The threshold energies for electrons and holes are derived from analysis of t-Se band structure taking into account energy and momentum conservation requirements (See previous section). The results of the calculation suggest that the ionization threshold in t-Se is approximately equal to the energy gap ($E_{\mathrm{th,e}} = E_{\mathrm{g}}$ and $E_{\mathrm{th,h}} = 1.05E_{\mathrm{g}}$ [207]). This result differs significantly

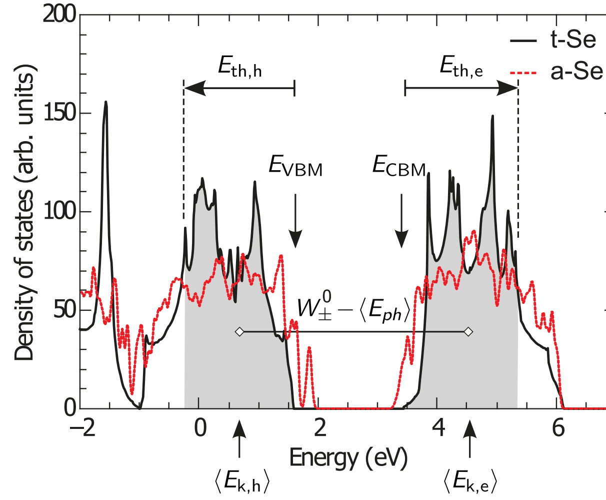

Fig. 4.14: Density of states in t-Se and a-Se calculated using DFT.

from that predicted by the parabolic band approximation ($E_{\mathrm{th}} = 1.5E_{\mathrm{g}}$) and can be attributed to the indirect band structure of t-Se.

Using the ionization threshold energies and the calculated DOS function $\rho(E)$ for t-Se and a-Se, we calculate the average kinetic energy for residual carriers as a weighted average of the shaded regions in Fig. 4.14. Using Eq. (4.18) we obtain the ratio $\rangle E_{\mathrm{k}}| / E_{\mathrm{g}} = 0.54 \mp 0.04$. Here the margins appear due to the uncertainty of the band gap energies. The difference between the average kinetic energy for electrons and holes is marginal and it does not exceed the error-bar. It should be noted that the obtained average kinetic energy is much less than that predicted by the parabolic band approximation $\rangle E_{\mathrm{k}}| / E_{\mathrm{g}} = 0.9$. The difference is largely attributed to the fact that $E_{\mathrm{th}} \ll E_{\mathrm{g}}$.

The average energy loss due to phonon-emission $\rangle E_{\mathrm{ph}}|$ between two successive ionization events can be estimated based on the average number of phonons emitted $\rangle r|$ and the optical phonon energy $\hbar\omega_{\mathrm{op}}$. According to Shockly [84], $\rangle r|$ is not sensitive to the material composition and ranges between 10 and 30. The phonon spectra of t-Se and a-Se phases are very similar [131] with the high-energy peak at 29 and 31 meV for t-Se and a-Se, respectively [214]. In our calculation we take the value of $\hbar\omega_{\mathrm{op}} = 30$ meV, which results in the average energy loss to phonons $\rangle E_{\mathrm{ph}}| = 0.3 \ldots 0.9$ eV. The pair creation energies in t-Se and a-Se calculated according to Eq. (4.12) are presented in Table 4.3. The expectation value of $W_{\mp}^{0}$ ranges between 4.4 and 5.6 eV depending on the choice of material parameters, E_{g} and $\rangle r|$. The difference

Tab. 4.3: Intrinsic pair creation energy (eV) in t-Se/a-Se assuming various various values of the energy gap and the average number $\rangle r|$ of optical phonons emitted.

$\rangle r|$	Energy gap (eV)		
	1.85	2.1	2.3
10	4.4/	4.7/4.4	5.0/4.5
20	4.7/	5.0/4.7	5.3/4.8
30	5.0/	5.3/5.0	5.6/5.1

between the values of $W^0_\mp$ for a-Se and t-Se is marginal (about 10%), and it can be attributed to a more uniform DOS of a-Se (Fig. 4.14). This data corresponds to the *intrinsic* pair creation energy implying that the electron-hole pair generation and collection is not mediated by recombination. The theoretical values of $W^0_\mp$ agree with those measured experimentally for a-Se: $W^0_\mp = 4\ldots6$ eV [206], 6 eV [215, 216], 5.4 eV [217]. The results of our detailed calculations are remarkably close to those obtained using the approximate Eq. (4.17) that explains the success of Que analysis of x-ray photogeneration in a-Se with the assumption that $E_\mathrm{g} = E_\mathrm{th}$. However, the violation of momentum conservation is not required in our case.

4.3.2 Fano factor

Fluctuations in the number of charge carriers generated as a result of absorption of a high-energy radiation can be expressed through the Fano factor. It is closely related to the intrinsic limit of the energy resolution of the detector (Ref. [200], p.377). The Fano factor was calculated from the variance σ_N^2 in the number N of electron-hole pairs generated per incident high-energy photon absorbed as follows [218]

$$F = \frac{\sigma_N^2}{\rangle N|} \ . \tag{4.19}$$

The statistics of electron-hole pair generation was modeled using a Monte Carlo simulation algorithm based on random values of $W^0_\mp$ and a fixed energy $\hbar\omega_0$ of the absorbed photon. The calculations were performed for the photon energy of 10 and 100 keV, but no noticeable difference in the value of Fano factor was found.

Random values of the electron-hole pair creation energy were determined according to

$$W^0_{\mp} = E_g + E_{k,e} + E_{k,h} + r\hbar\omega_{\mathrm{op}}\ . \tag{4.20}$$

Here $E_{k,e}$ and $E_{k,h}$ are the electron and hole kinetic energies taken randomly in the range $0 \ldots E_{th}$ with a probability distribution proportional to the density of states $\rho(E)$ in the conduction and valence band, respectively. The stochastic nature of energy loss due to the optical phonon emission is taken into account via a random number of phonons emitted r with the exponential distribution

$$p(r) = \rangle r|\ ^{1} e^{\ r/\rangle r|}\ , \tag{4.21}$$

where $\rangle r|$ represents the average number of phonons emitted per electron-hole pair produced.

Using a set of random values $W^0_{\mp}(i)$, the number of electron-hole pairs N generated per incident photon was determined from the following condition

$$0\ \sim\ \left[\sum_{i=1}^{N} W^0_{\mp}(i)\right]\quad \hbar\omega_0\ <\ W^0_{\mp}(N)\ . \tag{4.22}$$

After multiple realizations, we build a statistically viable set of data that allows for evaluation of the Fano factor using Eq. (4.19).

We proceed with calculation of the Fano factor according to its definition in Eq. (4.19) using the same parameters as for the pair creation energy. The results are presented in Table 4.4.

Tab. 4.4: Intrinsic Fano factor for t-Se/a-Se assuming various values of the energy gap.

$\rangle r|$	Energy gap (eV)		
	1.85	2.1	2.3
10	0.036/	0.031/0.044	0.030/0.043
20	0.044/	0.038/0.051	0.036/0.049
30	0.057/	0.050/0.063	0.046/0.059

Our calculations suggest that the intrinsic value of the Fano factor in t-Se and a-Se is in the range of $0.03 \ldots 0.06$. The Fano factor increases with decreasing energy gap E_{g} and increasing number of phonons $\rangle r|$ emitted between two consequent pair production events. The disparity

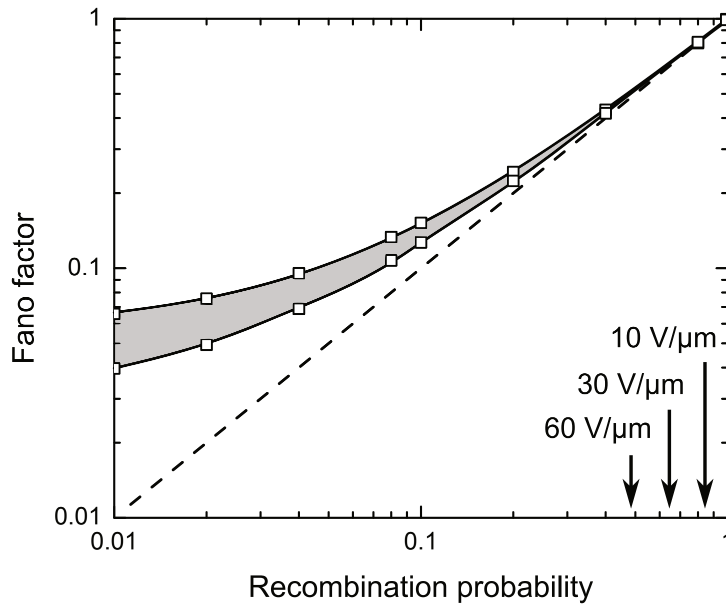

Fig. 4.15: Dependence of the Fano factor on the recombination probability in a-Se calculated using Monte Carlo simulation (symbols) and analytically using Eq. (4.23).

between a-Se and t-Se values of the Fano factor is practically negligible and can be assigned to a broader distribution of energy of resultant carriers in the case of a-Se. It is apparent that the Fano factor in t-Se and a-Se is superior to the corresponding value in such technologically prevalent semiconductors as Ge, Si and (CdZn)Te, where the Fano factor amounts to 0.059, 0.067 and 0.089, respectively[219, 220].

One should bear in mind that the intrinsic values of the Fano factor can only be observed under the circumstances of complete collection of photogenerated charge carriers. Recombination and charge trapping are two major mechanisms that limit the collection efficiency in a-Se [204, 215, 221]. Even at a relatively strong electric field of 10 V/μm, only about 10% of photogenerated carriers survive recombination, which is evident from the high value of the pair creation energy $W_{\mp} \ll 40$ eV [222] compared to the intrinsic value of $W_{\mp}^{0} \ll 5$ eV.

Provided recombination is the only stochastic factor that governs variation in the number N of electron-hole pairs created, statistics of the charge conversion are then described by a binomial distribution with the variance of $Np(1 \quad p)$ and mean $N(1 \quad p)$, where p is the recombination probability. Hence, according to Eq. (4.19), the Fano factor is given by $F = p$. This simple result sets the lower statistical limit for the Fano factor due to recombination.

In order to account for recombination as an additional source of variance in the number of

electron-hole pairs generated, we include the recombination probability p as a parameter into the Monte Carlo algorithm for the calculation of the Fano factor. The simulated dependence of the Fano factor on the recombination probability is presented in Fig. 4.15. The shaded region represents the uncertainty in the intrinsic value of the Fano factor according to the range of data in Table 4.4. The dashed line corresponds to the recombination-limited value of the Fano factor $F = p$. The arrows indicate an approximate value of the recombination probability taken from Refs. [204] and [222] for the specified electric fields. In the limit of small recombination probabilities, the Fano factor approaches its intrinsic value. The Fano factor then deteriorates progressively, approaching the limit of $F = p$, as the fraction of carriers that recombine increases.

Using a heuristic approach, we derived a general expression for the Fano factor

$$F = F_0(1 - p) + p\ . \tag{4.23}$$

that captures both effects: statistical fluctuations of the pair creation energy included in the intrinsic Fano factor F_0 and the carrier loss due to recombination. Equation (4.23) successfully reproduces results of the Monte Carlo simulation as shown in Fig. 4.15.

Our analysis suggests that the nearly intrinsic value of the Fano factor can only be achieved if one manages to keep the recombination probability below 0.1 for a-Se, or more generally $p \lesssim F_0$. In practice, the recombination can be controlled by the strength of an external electric field applied to the sample. The pulse height spectroscopy experiments performed on a-Se at a field of 20 V/μm indicate a broad distribution of Ns [222], which is consistent with the recombination-limited statistics. Apparently, electric fields much greater than 60 V/μm are required in order to lower the Fano factor down to its intrinsic limit (see Fig. 4.15).

In the case of single photon detectors when the energy of the incident radiation is concerned, the most important factor is the energy resolution, which is given by (Ref.[223], p. 118)

$$R = 2.35\sqrt{F/\langle N\rangle}\ . \tag{4.24}$$

Apparently, the lower Fano factor of the photoconductor directly translates into a better energy resolution of the detector. However, when the detector operates in the integration mode, one of the main performance factors is the detective quantum efficiency (Ref. [224], p. 26). The latter is proportional to the Swank factor A_S, which also depends on the Fano factor and the average number $\rangle N|$ of electron-hole pairs collected

$$A_\mathrm{S} = \frac{\rangle N|}{F + \rangle N|} \, . \tag{4.25}$$

Given the number of created charge carriers is much greater than the Fano factor, A_S in a-Se comes very close to unity [56], its ideal value. In this case, the Fano factor does not play a significant role in determining the detector characteristics.

The objective of our theoretical study in this section was the calculation of the charge pair production energy and the Fano factor in t-Se and a-Se. The calculation was based on the electronic structure of t-Se and a-Se, which was obtained self-consistently from first principles in the framework of a density functional theory. The statistics of the electron-hole pair generation were modeled using a Monte Carlo simulation technique and a random-**k** approximation to determine the final state of resultant charge carriers.

Results of our calculations suggest that the intrinsic theoretical value of the pair creation energy $W^0_\mp$ in a-Se and t-Se ranges between 5 and 6 eV. The value is practically insensitive to structural order of Selenium. The uncertainty is related to the flexibility in the choice of material parameters, such as the energy/mobility gap and the average number of phonons emitted between two consequent pair production events. Obtained values agree well with experimental data available in the literature for a-Se. The puzzling overestimation of $W^0_\mp$ by Klein's [201] traditional formula is attributed to a relatively low average kinetic energy of resultant charge carriers. This observation is closely related to low ionization threshold energies for both charge carriers in t-Se as a consequence of its indirect band structure. Our interpretation provides an alternative to violation of the momentum conservation, which was put forward previously in the literature to explain the deviation of $W^0_\mp$ from Klein's [201] formula.

According to theoretical predictions, the intrinsic value of the Fano factor F_0 in Selenium is confined within the range of $0.03\ldots0.06$, which is superior to the corresponding characteristic in Si, Ge and (GdZn)Te. However, achieving these values practically can be challenging due to the recombination of photogenerated charge carriers, which is present to a large extent in Selenium even at strong electric fields ($10\ldots60$ V/μm). We propose a correction to the Fano factor that takes into account effect of the carrier loss due to recombination. The analysis suggests that the nearly intrinsic value of the Fano factor can only be achieved, when the recombination probability is reduced below F_0. Otherwise, the Fano factor and, correspondingly, the energy resolution of a detector is limited by a recombination statistics rather than by fluctuations in the pair creation energy.

5. SUMMARY

The objective of this thesis was to investigate the high-field charge carrier transport properties in amorphous Selenium. The energy loss mechanism that prevents the carriers from gaining sufficient kinetic energy to initiate impact ionization is inelastic scattering of electrons with optical phonons. Calculation of electron-phonon matrix elements in trigonal Selenium was performed for optical phonon modes.

Here, we assume that the calculated results based on crystalline Selenium structure can be also translated into the amorphous structure. This was supported through studies of density of states and phonon density of states in both amorphous and crystalline phases of Selenium. In addition, an amorphous Selenium structure was simulated and the volume deformation potential was studied for both trigonal and the simulated amorphous lattice. As a consequence, we showed that a similar energy dependence of deformation potential for electrons and holes can be seen in both trigonal and amorphous Selenium. This further confirmed the validity of our assumption.

Results from calculation of electron-phonon matrix elements suggest that the energetic holes should experience an interaction by an order of magnitude weaker than that of electrons. The results for holes are attributed to the weak interaction of lone-pair states with the corresponding phonon modes and linked to the favorable high-field transport of holes in amorphous Selenium

Furthermore, we showed that the single-carrier multiplication regime can be achieved by confinement of the kinetic energy for the counterpart charge carrier. This hypothesis was demonstrated through a detailed analysis of the electronic structure of trigonal Selenium. This investigation involved studies of all possible inverse Auger transitions for both electrons and holes in the Selenium Brillouin zone. The precursor of the latter calculations is finding the ion-

ization threshold energy. The ionization threshold energies for electrons and holes in t-Se were computed based on its electronic structure. Our results suggest that the ionization threshold energy for both holes and electrons in t-Se is approximately equal to the energy gap, which is significantly different from the result predicted by the parabolic band approximation.

Following the latter analysis, we showed that the effective density of states for the impact ionization with holes as a primary carrier can exceed by 3 orders of magnitude the corresponding value for electrons. This result is due to the presence of an energy gap in the conduction band that limits electrons from acquiring high kinetic energy. This is consistent with the experimental observation of dominant holes avalanche multiplication in poly-crystalline Selenium.

In addition, the calculated threshold energies were used in conjunction with the Selenium density of states in order to analyze the electron-hole pair creation energy and Fano factor in t-Se and a-Se. Results of our calculations suggest that the intrinsic theoretical value of the pair creation energy $W^0_{\mp}$ in a-Se and t-Se ranges between 4.4 and 5.6 eV. Obtained values agree well with experimental data available in the literature for a-Se. We also proposed a correction to the Fano factor that takes into account effect of the carrier loss due to recombination. The analysis suggests that the nearly intrinsic value of the Fano factor in the range of 0.003 0.006 can only be achieved, when the recombination probability is reduced below F_0. Otherwise, the Fano factor and, correspondingly, the energy resolution of a detector is limited by a recombination statistics rather than by fluctuations in the pair creation energy.

BIBLIOGRAPHY

[1] K. Tanaka and K. Shimakawa. *Amorphous Chalcogenide Semiconductors and Related Materials*. Springer, 2011.

[2] J. P. R. David and C. H. Tan. *IEEE Journal of selected topics in quantum electronics*, 14:998, 2008.

[3] O. Rubel and D. Laughton. *J. Phys: Condens. Matter*, 22:355803, 2010.

[4] I. Ono, P. C. Grekos, T. Kouchi, M. Nakatake, M. Tamura, and S. Hosokawa. *J. Phys: Condens. Matter*, 8:7249, 1996.

[5] T. Nakayama. *J. Phys. Soc. Jpn*, 33:12, 1972.

[6] D. C. Ghosh, N. C. Ghosh, and P. K. Haldar. *Engineering Physics*. Firewall Media, 2008.

[7] J. Sestak, J. J. Mares, and P. Hubik. *Glassy, Amorphous and Nano-Crystalline Materials: Thermal Physics, Analysis, Structure and Properties*. Springer, 2010.

[8] M. F. Kotkata. *K. Mater. Sci.*, 27:1785, 1992.

[9] D. R. Askeland, P. P. Fulay, and W. J. Wright. *The Science and Engineering of Materials*. Cengage Learning, 2010.

[10] G. K. Vemulapalli. *Invitation to Physical Chemistry*. World Scientific, 2010.

[11] R. Fairman and B. Ushkov. *Semiconducting Chalcogenide Glass I: Glass Formation, Structure, and Stimulated Transformations in Chalcogenide Glasses*. Academic Press, 2004.

[12] R. A. Street. *Hydrogenated Amorphous Silicon*. Cambridge University Press, 2005.

[13] A. Popov. *Disordered Semiconductors: Physics and Applications*. Pan Stanford Publishing, 2011.

[14] D. Hohl and R. O. Jones. *Phys. Rev. B*, 43:3856, 1991.

[15] M. Misawa and K. Suzuki. *J. Phys. Soc. Jpn.*, 44:1612, 1978.

[16] X. Zhang and D. A. Drabold. *Phys. Rev. Lett*, 83:5042, 1999.

[17] H. Kalebozan M. Ozenbas. *J. Crystal Growth*, 78:523, 1986.

[18] N. F. Mott and E. A. Davis. *Electronic Processes in Non-Crystalline Materials*. Oxford University Press, 1979.

[19] AV. Kolobov, P. Fons, AI. Frenkel, AL. Ankudinov, J. Tominaga, and T. Uruga. *Nature Materials*, 3:703, 2004.

[20] A. Pirovano, A.L. Lacaita, A. Benvenuti, F. Pellizzer, and R. Bez. *IEEE Trans. Electron Devices*, 51:452, 2004.

[21] H. Horii, J.H. Yi, Y.H. Park, J.H.and Ha, I.G. Baek, S.O. Park, Y.N. Hwang, S.H. Lee, Y.T. Kim, K.H. Lee, UIn. Chung, and J.T. Moon. *VLSI Technology, Digest of Technical Papers.*, page 177, 2003.

[22] Ovshinskey, 1992.

[23] W. E. Carel and Van. Ejik. *Phys. Med. Biol*, 47:R85, 2002.

[24] W. Que and J. A. Rowlands. *Medical Physics*, 22:365, 1995.

[25] W. Zhao and J. A. Rowlands. *J Med Phys.*, 22:1595, 1995.

[26] W. Zhao, I. Blevis, S. Germann, JA. Rowlands, D. Waechter, and Z. Huang. *J Med Phys.*, 24:1834, 1997.

[27] U. Neitzel, I. Maack, and S. Gnther-Kohfahl. *J Med Phys.*, 21:509, 1994.

[28] W. Smith. *Selenium : its electrical qualities, and the effect of light thereon*. London, 1877.

[29] M. Mayer, D. Speaks, K. Yu, S. S. Mao, E. E. Haller, and W. Walukiewicz. *Appl. Phys. Lett.*, 97:022104, 2010.

[30] S. Zannos. *Chester Carlson and the Development of Xerography*. Mitchell Lane Publishers, 2002.

[31] M. Yaffe and J. Rowlands. *J. A. Med. Biol.*, 42:1, 1997.

[32] A. Reznik, S. D. Baranovskii, O. Rubel, K. Jandieri, S. Kasap, Y. Ohkawa, ans K. Tanioka M. Kubota, and J. Rowlands. *J. Non-Cryst. Solids.*, 354:2691, 2008.

[33] G. Juska and K. Arlauskas. *Phys. Status Solidi (a)*, 59:389, 1980.

[34] G. Juska and K. Arlauskas. *Phys. Status Solidi (a)*, 77:387, 1983.

[35] V. I. Mikla. *Amorphous Chalcogenides: The Past, Present and Future*. Elsevier, 2011.

[36] M. Fukuda. *Optical Semiconductor Devices*. John Wiley & Sons, 1998.

[37] R. C. Dorf. *The Electrical Engineering Handbook*. CRC Press, 1997.

[38] K. Lizuka. *Engineering Optics, Volume 10*. Springer, 2008.

[39] M. M. Khalil. *Basic Sciences of Nuclear Medicine*. Springer, 2010.

[40] Mi. N. Wernick and J. N. Aarsvold. *Emission Tomography: The Fundamentals of PET and SPECT*. Academic Press, 2004.

[41] R. J. McIntyre. *IEEE Trans. Electron Devices*, 13:164, 1966.

[42] V. Saveliev and V. Golovin. *Nucl. Instr. Meth. Phys. Res. A*, 442:223, 2000.

[43] P. Yuan, C. Hansing, and K. Anselm. *IEEE J. Quantum Electron.*, 36:198, 2000.

[44] A. Konstantinov, Q. Wahab, and N. Nordell. *J. Appl. Phys. Lett.*, 71:90, 1997.

[45] J. Beck, C. Wan, M. Kinch, J. Robinson, P. Mitra, R. Scritchfield, F. Ma, and J. Campbell. *J. Electron. Mater.*, 35:6, 2006.

[46] A. J. Flewit and W. I. Milne. *Proceedings of the IEEE.*, 93, 2005.

[47] A. Madan and M.P. Shaw. *The Physics and Applications of Amorphous Semiconductors*. Academic Press, 1988.

[48] W. C. Tan. *Optical properties of Amorphous Selenium films*. Saskatchewan University, 2006.

[49] N. F. Mott. *Adv. Phys.*, 16:49–57, 1967.

[50] R. M. Blakney and H. P. Grunwald. *Phys. Rev.*, 159:664, 1967.

[51] M. Akiyama, M. Hananda, H. Takao, K. Sawada, and M. Ishida. *Jpn. J. Appl. Phys.*, 41:2552, 2002.

[52] M. Spahn. *European Radiology*, 15:1934, 2005.

[53] S. Kasap and J. A. Rowlands. *J. Mater. Sci. Mater.*, 11:179, 2000.

[54] D. L. Lee, L. K. Cheung, B. Rodricks, and G. F. Powell. *Proceedings of the Society of Photo-Optical Instrumentation Engineers (SPIE)*, 3336:14, 1998.

[55] E. Kotter and M. Langer. *European Radiology*, 12:2562, 2002.

[56] S. Kasap and J. A. Rowlands. *Proceedings of the IEEE*, 90:591, 2002.

[57] M. Bissonnette, M. Hansroul, E. Masson, S. Savard, S. Cadieux, P. Warmoes, D. Gravel, J. Agopyan, B. Polischuk, W. Haerer, T. Mertelmeier, JY Lo, Y. Chen, JT. Dobbins, and and S. Singh JL. Jesneck. *Proceedings of the Society of Photo-Optical Instrumentation Engineers (SPIE)*, 5745:529, 2005.

[58] W. Zhao, G. Ristic, and JA. Rowlands. *J Med Phys.*, 31:2594, 2004.

[59] E. Samei and MJ. Flynn. *J Med Phys.*, 30(4):608–622, APR 2003.

[60] K. Tanioka, J. Yamazaki, K. Shidara, K. Taketoshi, T. Kawamura, S. Ishioka, and Y. Takasaki. *IEEE Electr. Device. L.*, 8:392, 1987.

[61] K. Tanioka, T. Matsubara, Y. Ohkawa, K. Miyakawa, S. Suzuki, T. Takahata, N. Egami, K. Ogusu, A. Kobayashi, Tand. Hombo M. Hirai, Tand. Kawai, and T. Yoshida. *IEICE Trans. Electron.*, E86C:1790, 2003.

[62] M. Kubota, T. Kato, S. Suzuki, H. Maruyama, K. Shidara, K. Tanioka, K. Sameshima, T. Makishima, K. Tsuji, T. Hirai, and T. Yoshida. *IEEE Trans. Broadcast.*, 42:251, 1996.

[63] K. Miyake and I. Ota. *Arch Ophthalmol.*, 117:1623, 1999.

[64] G. Stcklin and V.W. Pike. *Radiopharmaceuticals for Positron Emission Tomography - Methodological Aspects*. Springer, 1993. Ch. 1.

[65] D. L. Bailey, D. W. Townsend, P. E. Valk, and M. N. Maisey. *Positron Emission Tomography: Basic Sciences*. Springer, 2005. Ch. 2.

[66] M. E. Phelps. *PET: Molecular Imaging and Its Biological Applications*. Springer, 2004. Ch. 1.

[67] H. T. Chugani, M. E. Phelps, and J. C. Mazziotta. *Annals of Neurology*, 22:487, 2004.

[68] S. Yasuda, M. Ide, H. Fujii, T. Nakahara, Y. Mochizuki, W. Takahashi, and A. Shohtsu. *Br. J. Cancer.*, 83:1607, 2000.

[69] P. Camicia, E. Ferranninia, and L. H. Opie. *Progress in Cardiovascular Diseases*, 32:217, 1989.

[70] G. Chiro and Di. MD. *Investigative Radiology*, 22:360, 1987.

[71] T. Beyer, DW. Twonsend, and T. Brun. *J. Nucl. Med*, 41:1369, 2000.

[72] DW. Townsend. *J. Nucl. Med*, 42:533, 2001.

[73] Pj. Ell and GK. von Schulthess. *Eur J Nucl Med Mol Imaging*, 29:719, 2002.

[74] B. J. Pichler, M. S. Judenhofer, C. Catana, and J. H. Walton. *J. Nucl. Med*, 47:639, 2006.

[75] Y. Shao. *IEEE Trans. Nucl. Sci.*, 44:1167, 1997.

[76] K. M. Gilbert, W. B. Handler, T. J. Scholl, J. W. Odegaard, and B. A. Chronik. *Phys. Med. Biol*, 51:2825, 2006.

[77] H. P. Schlemmer. *J. Nucl. Med*, 48:45P, 2007.

[78] M . S. Judenhofer et al. *Nature Medicine*, 14:459, 2008.

[79] H. M. Rougeot and G. E. Possin. *United States Patent*, page 5198673, 1993.

[80] W Zhao, D Li, A Reznik, B Lui, DC Hunt, K Tanioka, and JA Rowlands. *Proc. SPIE*, 5745:352, 2005.

[81] A. Reznik, BJ. Lui, and J. A. Rowlands. *Technol Cancer Res Treat*, 4:61, 2005.

[82] B. K. Ridley. *J. Phys. C: Solid State Phys*, 16:3373, 1983.

[83] G. A. Baraff. *Phys. Rev.*, 128:2507, 1962.

[84] W. Shockley. *Solid-State Electron*, 2:35, 1961.

[85] S. Kasap, J. A. Rowlands, S. D. Baranovskii, and K. Tanioka. *J. Appl. Phys.*, 96:2037, 2004.

[86] K. Tsuji, Y. Takasaki, T. Hirai, and K. Taketoshi. *J. Non-Cryst. Solids*, 114:94, 1989.

[87] O. Rubel, S. Baranovskii, I. P. Zvyagin, P. Thomas, and S. Kasap. *Phys. stat. sol. (c)*, 1:1186, 2004.

[88] O. Rubel, A. Potvin, and D. Laughton. *J. Phys: Condens. Matter*, 23:055802, 2011.

[89] K. G. McKay and K. B. McAfee. *Phys. Rev.*, 91:1079, 1953.

[90] P. A. Wolff. *Phys. Rev.*, 95:1415, 1954.

[91] C. A. Lee, A. Logan, R. L. Batdorf, J. J. Kleimack, and W. Wiegmann. *Phys. Rev.*, 134:A761, 1964.

[92] R. Chin, N. Holonyak, G. E. Stillman, J. Y. Tang, and K. Hess. *Electronics Letters*, 16:467, 1980.

[93] C. R. Crowell and S. M. Sze. *Appl. Phys. Lett.*, 9:242, 1966.

[94] E. Bringuier. *Phys. Rev. B*, 49:7974, 1994.

[95] M. Lundstrom. *Fundamentals of Carrier Transport*. Cambridge University Press, 2009.

[96] G. Juska, K. Arlauskas, and E. Montrimas. *J. Non-Cryst. Solids*, 97:559–561, 1987.

[97] V. Arkhipov and S. Kasap. *J. Non-Crys. Solids*, 266:959, 2000.

[98] W. C. Hamilton. *Solid State Commun.*, 14(10):1089, 1974.

[99] K. Brennan. *The Physics of Semiconductors: With Applications to Optoelectronic Devices*. Cambridge University Press, 1999.

[100] W. A. Harrison. *Solid State Theory*. McGraw Hill, 1970.

[101] P. Y. Yu and M. Cardona. *Fundamentals of Semiconductors: Physics and Materials Properties*. Springer, 2010.

[102] A. Rose. *Electron phonon interactions: A novel semiclassical approach*. World Scientific, 1989.

[103] F. Murhpy-Armando and S. Fahy. *Phys. Rev. B*, 78:035202, 2008.

[104] B. W. Corb, W. D. Wei, and B. L. Averbach. *J. Non-Cryst. Solids*, 53:29, 1982.

[105] M. Long, P. Galison, and R. Alben. *Phys. Rev. B.*, 13:1821, 1976.

[106] W. E. Spear. *Proc. Phys. Soc.*, 76:826, 1960.

[107] W. E. Spear. *Proc. Phys. Soc. B.*, 70:669, 1957.

[108] A. Rose. *Proc. of the Int. Workshop on Amorphous Semiconductors*, page 29, 1987.

[109] A. P. Saunders. *J. Phys. Chem*, 4:423, 1900.

[110] V. S. Minaev, S. P. Timoshenkov, and V. V. Kalugin. *J Optoelectron Adv M.*, 7:1717, 2005.

[111] P. Cherin and P. Unger. *Inorg. Chem.*, 6:1589, 1967.

[112] M. Kastner. *Phys. Rev. Lett*, 28:355, 1972.

[113] M. Kastner. *Phys. Rev. Lett*, 28:255, 1972.

[114] R. Fischer. *Phys. Rev. B.*, 5:3087, 1972.

[115] B. Moreth. *Phys. Rev. Lett*, 42:264, 1979.

[116] Jai. Singh. *Optical Properties of Condensed Matter and Applications*. John Wiley & Sons, 2006.

[117] J. Piprek. *Semiconductor Optoelectronic Devices: Introduction to Physics and Simulation*. Academic Press, 2003.

[118] G. J. Wilfried, H. M. van Sark, L. Korte, and F. Roca. *Physics and Technology of Amorphous-Crystalline Heterostructure Silicon Solar Cells*. Springer, 2011.

[119] O. Madelung. *Introduction to Solid-State Theory*. Springer, 1995.

[120] A. E. Ioffe and A. R. Regel. *Progress in semiconductors*. Heywood Co, Ltd London, 1960.

[121] M. F. Thorpe and D. Weaire. *Phys. Rev. B.*, 4:3518, 1971.

[122] M. F. Thorpe and D. Weaire. *Phys. Rev. B.*, 4:2508, 1971.

[123] P. Nielsen. *Phys. Rev. B.*, 6:3739, 1972.

[124] J. D. Joannopoulos, M. Schluter, and M. L. Cohen. *Phys. Rev. B.*, 11, 1976.

[125] D. W. Bullett. *J. Phys. C: Solid State Phys*, 8:377, 1975.

[126] K. Nakamura and A. Ikawa. *Comput. Phys.*, 142:295, 2001.

[127] N. J. Shevchik, M. Cardona, and J. Tejeda. *Phys. Rev. B.*, 8:2833, 1973.

[128] M. Takumi, Y. Tsujioka, N. Hirai, K. Yamamoto, and K. Nagata. *J. Phys.: Conf. Ser.*, 215:012049, 2010.

[129] B. Vanhuyse, W. Grevendonk, G. J. Adriaenssens, and J. Dauwen. *Phys. Rev. B.*, 35:9298, 1987.

[130] M. Abkowitz. *Philos. Mag. Lett.*, 58:53, 1988.

[131] F. Gompf. *J. Phys. Chem. Solids.*, 42:539, 1981.

[132] A. B. Zahlan. *Excitons, Magnons and Phonons in Molecular Crystals*. Cambridge University Press, 1968.

[133] W. Kohn. *Rev. Mod. Phys.*, 71:1253, 1999.

[134] D. S. Sholl and J. A. Steckel. *Density Functional Theory*. Wiley, 2009.

[135] D. R. Hartree. *Proc. Camb. Phil. Soc*, 24:89, 1928.

[136] D. R. Hartree. *Proc. Camb. Phil. Soc*, 24:111, 1928.

[137] A. F. J. Levi. *Applied Quantum Mechanics*. Cambridge University Press, 2006.

[138] K. I. Ramachandran, G. Deepa, and K. Namboori. *Computational Chemistry and Molecular Modeling*. Springer, 2008.

[139] P. Hohenberg and W. Kohn. *Phys. Rev. B.*, 136:864, 1964.

[140] I. N. Levine. *Quantum Chemistry*. Prentice Hall, Upper Saddle River, NJ, 2000.

[141] E. Hasselbrink and B. I. Lundqvist. *Handbook of surface science: Electronic Structure*. Elsevier, 2008.

[142] A. H. Winter. *Theoretical and Experimental Investigations of High Spin Ionic Intermediates*. ProQuest, 2007.

[143] F. Jensen. *Introduction to quantum chemistry*. John Wiley & Sons, 2007.

[144] V. May and O. Kohn. *Charge and Energy Transfer Dynamics in Molecular Systems*. John Wiley & Sons, 2008.

[145] J. Thijssen. *Computational physics*. Cambridge University Press, 2007.

[146] J. P. Dahl and J. Avery. *Local density approximations in quantum chemistry and solid state physics*. Plenum Press, 1984.

[147] C. Filippi, C. J. Umrigar, and X. Gonze. *Generalized gradient approximations to density functional theory: comparison with exact results*. Cornell Theory Center, Cornell University, 1996.

[148] J. P. Perdew and Y. Wang. *Phys. Rev. B.*, 45:13244, 1992.

[149] J. P. Perdew and Y. Wang. *Phys. Rev. B.*, 33:8800, 1986.

[150] J. P. Perdew, K. Burke, and M. Ernzerhof. *Phys. Rev. Lett*, 80:890, 1998.

[151] J. P. Perdew and S. Kurth. *Phys. Rev. Lett*, 82:2544, 1999.

[152] R. M. Martin. *Electronic Structure: Basic Theory and Practical Methods*. Cambridge University Press, 2004.

[153] J. M. Seminario. *Recent Developments And Applications Of Modern Density Functional Theory*. Elsevier, 1996.

[154] J. P. Perdew. *Int. J. Quantum Chem.*, 28:497, 1985.

[155] W. Kohn and L. J. Sham. *Phys. Rev.*, 140:A1133, 1965.

[156] X. Gonze, B. Amadon, P.M. Anglade, J.-M. Beuken, F. Bottin, P. Boulanger, F. Bruneval, D. Caliste, R. Caracas, M. Cote, T. Deutsch, L. Genovese, Ph. Ghosez, M. Giantomassi,

S. Goedecker, D.R. Hamann, P. Hermet, F. Jollet, G. Jomard, S. Leroux, and S. Mazevet M. Mancini, M.J.T. Oliveira, G. Onida, Y. Pouillon, T. Rangel, G.M. Rignanese, R. Shaltaf D. Sangalli, M. Torrent, M.J. Verstraete, G. Zerah, and J.W. Zwanziger. *Computer Phys. Commun..*, 180:2582, 2009.

[157] X. Gonze, G.-M. Rignanese, M. Verstraete, J.-M. Beuken, Y. Pouillon, R. Caracas, F. Jollet, M. Torrent, G. Zerah, M. Mikami, Ph. Ghosez, M. Veithen, J.-Y. Raty, V. Olevano, F. Bruneval, L. Reining, R. Godby, G. Onida, D.R. Hamann, and D.C. Allan. Zeit. *Zeit. Kristallogr*, 220:558, 2005.

[158] D. J. Singh and L. Nordstrom. *Planewaves, Pseudopotentials, and the LAPW Method*. Brikhauser, 2005.

[159] E. Hasselbrink and B. I. Lundqvist. *Handbook of surface science: Electronic structure*. Elsevier, 2008.

[160] E. V. Anslyn and D. A. Dougherty. *Modern Physical Organic Chemistry*. University Science books, 2006.

[161] X. Gonze. *Phys. Rev. B*, 77:10337, 1997.

[162] X. Gonze and C. Lee. *Phys. Rev. B.*, 55:10355, 1997.

[163] D. A. Jelski and F. G. Thomas. *Computational Studies of New Materials*. World Scientific, 1999.

[164] H. Monkhorst and J. Pack. *Phys. Rev. B*, 13:5188, 1976.

[165] H. Swanson, W. Gilfrich, and G. Ugrinic. 1955.

[166] R. Grosse, H. Swoboda, and A. Tausend. *J. Phys. C: Solid State Phys.*, 8:L445, 1975.

[167] R. Geick W. Teuchert. *Phys. Status Solidi (b)*, 61:123, 1974.

[168] W. Teuchert, R. Geick, G. Landwehr, H. Wendel, and W. Weber. *J. Phys. C: Solid State Phys.*, 8:3725, 1975.

[169] J. R. Reitz. *Phys. Rev.*, 105:1233, 1957.

[170] D. J. Olechna and R. S. Knox. *Phys. Rev.*, 140:A986, 1965.

[171] Simpei Tutihasi and Inan Chen. *Phys. Rev.*, 158:623, 1967.

[172] N. Hindley. *J. Non-Cryst. Solids*, 8-10:557, 1972.

[173] Y. Masumoto and T. Takagahara. *Semiconductor Quantum Dots: Physics, Spectroscopy and Applications*. Springer, 2002.

[174] B. Wong and A. Mittal. *Nano-CMOS Circuit and Physical Design*. John Wiley & Sons, 2004.

[175] W. A. Harrison. *Electronic structure and the properties of solids*. Dover Publications, Inc., New York, 1988.

[176] R. Sutton, B. Rockett, and P. G. Swindells. *Chemistry for the Life Sciences*. CRC Press, 2000.

[177] M. Misawa and K. Suzuki. *Trans. Japan. Inst. Metals*, 18:427, 1977.

[178] S. Balasubramanian, K.V. Damodaran, and K.J. Rao. *Chem. Phys.*, 166:131, 1992.

[179] D. Vanderbilt and J. D. Joannopoulos. *Phys. Rev. B.*, 27:6296, 1983.

[180] R. Bellissent and G. Tourand. *J. Non-Cryst. Solids*, 35-36:1221, 1980.

[181] P. Blaha, K. Schwarz, G. K. H. Madsen, D. Kvasnicka, and J. Luitz. *Wien2k: An Augmented Plane Wave + Local Orbitals Program for Calculating Crystal Properties*. Karlheinz Schwarz, Techn. Universität Wien, Austria, 2001.

[182] J. P. Perdew, K. Burke, and M. Ernzerhof. *Phys. Rev. Lett.*, 77:3865, 1996.

[183] X. Zhang and D. A. Drabold. *J. Non-Cryst. Solids*, 241:195, 1998.

[184] S. Wei and A. Zunger. *Phys. Rev. B*, 60:5404, 1999.

[185] T. Yoshizawa. *Handbook of optical metrology: principles and applications*. CRC Press, 2009.

[186] S. Kasap, C. Koughia, H. Ruda, and R. Johanson. *Springer Handbook of Electronic and Photonic Materials*. Springer, 2006.

[187] S. Adach. *GaAs and related materials*. World Scientific Publishing Co., Singapore, 1994.

[188] L. W. Cook, G. E. Bulman, and G. E. Stillman. *Appl. Phys. Lett.*, 40:589–591, 1982.

[189] C. L. Anderson and C. R. Crowell. *Phys. Rev. B*, 5:2267, 1972.

[190] H. P. D. Lanyon and R. E. Richardson. *Phys. Status Solidi (a)*, 7:421–425, 1971.

[191] N. Sano and A. Yoshii. *J. Appl. Phys.*, 77:2020–2025, 1995.

[192] A. Darbandi and O. Rubel. *J. Non-Cryst. Solids*, 358:2434–2436, 2012.

[193] E. Devoie, A. Darbandi, and O. Rubel. Electronic structure of amorphous selenium. (unpublished).

[194] J. Paier, R. Asahi, A. Nagoya, and G. Kresse. *Phys. Rev. B*, 79:115126, 2009.

[195] S. Chen, X. G. Gong, A. Walsh, and S. Wei. *Phys. Rev. B*, 79:165211, 2009.

[196] C. Persson. *J. Appl. Phys.*, 107:053710, 2010.

[197] H. Katagiri, K. Jimbo, S. Yamada, T. Kamimura, W. Shwe Maw, T. Fukano, T. Ito, and T. Motohiro. *Appl. Phys. Express*, 1:041201, 2008.

[198] Y. Eisen, A. Shor, and I. Mardor. *Nucl. Instrum. Meth. A*, 428:158–170, 1999.

[199] C. Scheiber and G. C. Giakos. *Nucl. Instrum. Meth. A*, 458(1):12–25, 2001.

[200] G.F. Knoll. *Radiation detection and measurement*. New York, John Wiley and Sons, Inc., 1979.

[201] C. A. Klein. *J. Appl. Phys.*, 39(4):2029–2038, 1968.

[202] R. C. Alig and S. Bloom. *Phys. Rev. Lett.*, 35:1522–1525, 1975.

[203] E. O. Kane. *Phys. Rev.*, 159:624, 1967.

[204] W. Que and J. A. Rowlands. *Phys. Rev. B*, 51:10500–10507, Apr 1995.

[205] G. Juska. *J. Non-Cryst. Solids*, 137–138:401, 1991.

[206] S. O. Kasap, V. Aiyah, B. Polischuk, and A. Baillie. *J. Appl. Phys.*, 83(6):2879–2887, 1998.

[207] A. Darbandi and O. Rubel. 2012. arXiv:1210.4119 [cond-mat.mtrl-sci].

[208] J. Geist and W. K. Gladden. *Phys. Rev. B*, 27:4833–4840, 1983.

[209] L. Tichỳ, H. Tichá, P. Nagels, E. Sleeckx, and R. Callaerts. *Mater. Lett.*, 26(6):279–283, 1996.

[210] A. Solieman and A. A. Sehly. *Physica B: Condensed Matter*, 405(4):1101–1107, 2010.

[211] X. Gonze, J.-M. Beuken, R. Caracas, F. Detraux, M. Fuchs, G.-M. Rignanese, L. Sindic, M. Verstraete, G. Zerah, F. Jollet, M. Torrent, A. Roy, M. Mikami, Ph. Ghosez, J.-Y. Raty, and D.C. Allan. *Comp. Mater. Sci.*, 25:478, 2002.

[212] N. Troullier and J. L. Martins. *Phys. Rev. B*, 43:1993, 1991.

[213] M. Fuchs and M. Scheffler. *Comp. Phys. Comm.*, 119:67, 1999.

[214] V. V. Poborchii, A. V. Kolobov, and K. Tanaka. *Appl. Phys. Lett.*, 72(10):1167–1169, 1998.

[215] S. Kasap. *J Phys D: Appl Phys.*, 33:2853, 2000.

[216] C. Haugen, S. O. Kasap, and J. Rowlands. *J Phys D: Appl Phys.*, 32:200, 1999.

[217] M. Lachaine and B.G. Fallone. *J Phys D: Appl Phys.*, 33:1417, 2000.

[218] U. Fano. *Phys. Rev.*, 72:26–29, 1947.

[219] T. Papp, M. C. Lepy, J. Plagnard, G. Kalinka, and E. Papp-Szabo. *X-Ray Spectrom.*, 34(2):106–111, 2005.

[220] R. H. Redus, J. A. Pantazis, A. C. Huber, V. T. Jordanov, J. F. Butler, and B. Apotovsky. In *MRS Proceedings*, volume 487, page 101, 1997.

[221] Y. Fang, A. Badal, N. Allec, K.S. Karim, and A. Badano. *Med. Phys.*, 39(1):308, 2012.

[222] I. M. Blevis, D. C. Hunt, and J. A. Rowlands. *J. Appl. Phys.*, 85(11):7958–7963, 1999.

[223] W. R. Leo. *Techniques for Nuclear and Particle Physics Experiments*. Springer, 1994.

[224] P. Gevenois and A. Bankier. *Imaging*. European Respiratory Society, 2004.